Università degli Studi di Ferrara

Physics and Earth Science Department

Degree of Doctor of Philosophy in subject of Physics

DEVELOPMENT OF A HIGH PRECISION LYSO POLARIMETER FOR EDM SEARCH AT COSY STORAGE RING

Supervisors

Prof. *Paolo Lenisa*

Dr. *Luca Barion*

Candidate

Simone Basile

PhD Coordinator

Prof. *Vincenzo Guidi*

Cycle XXI

SUMMARY

INTRODUCTION **5**

CHAPTER 1 - Theoretical Background **7**

1.1 Matter over anti-matter imbalance and discrete fundamental symmetries 7

1.1.3 Combination of charge and parity transformation 10

1.2 Electric Dipole Moments 11

1.2.1 Definition of Electric Dipole Moment 11

1.2.2 EDMs experimental measurements 13

CHAPTER 2 - EDM measurements in storage rings **19**

2.1 EDM searches in storage rings 19

2.1.1 Main principle 19

2.1.2 Pure electric storage ring 21

2.1.3 Combined electric and magnetic ring 22

2.1.4 Pure magnetic storage ring 22

2.1.5 RF Wien Filter 23

CHAPTER 3 - The Cooler Synchrotron (COSY) storage ring **28**

3.1 The COSY storage ring facility 28

3.1.1 Main storage ring 28

3.1.2 Polarized source 30

3.2 Polarimetry measurements at COSY 31

3.2.1 EDDA 31

3.2.2 Differential cross sections 32
3.2.3 Relevant polarimetry observables 35
3.2.4 Errors in polarization measurements 35
3.3 measurement of horizontal polarization 37
3.3.1 Experimental cycle with the *time-stamp system* 37
3.4 Achievements at COSY storage ring 41
3.4.1 Spin coherence time (SCT) measurement 41
3.4.2 Spin tune measurement 44
3.3 COSY, an ideal starting point for... 45
CHAPTER 4 - LYSO Polarimeter Development.....48
4.1 General description and characteristics 48
4.2 Description of a single LYSO module 51
4.3 First step: Comparing PMTs and SiPMs in LYSO readout 52
4.3.1 Setup description 52
4.3.2 Read-out electronics design and development 57
4.3.3 Experimental results 60
4.4 Step 2: detection of a scattering asymmetry 65
4.4.1 Setup description 65
4.4.2 Read-out electronics design and development 70
4.4.3 Experimental Results and data analysis 71
4.5 Step 3: LYSO crystals homogeneity scans 100
4.5.1 Setup description 100
4.5.2 Results of LYSO crystals front and side scans 102
4.5.3 Comparison between different types of SiPMs 104
CONCLUSIONS.....106
BIBLIOGRAPHY.....108

INTRODUCTION

The baryogenesis is one of the greatest unanswered questions in contemporary physics. According to Sakarov's conditions for baryogenesis, a process must have occurred early in universe's life, that violated the fundamental CP-symmetry and led to the dominance of matter over antimatter in our universe. However all descriptions provided by the Standard Model in terms of CP-violating processes are insufficient by several order of magnitude to explain the observed abundance of matter. There must be some larger CP violation source, the observation of which could lead to the explanation of the matter-antimatter asymmetry and to new physics beyond the SM.

A strong source of CP violation could manifest in the existence of an Electric Dipole Moment (EDM) of elementary particles. For neutral particles EDMs investigations started about 60 years ago, the approach was based on the use of magnetic traps, so far all results of EDM measurements are compatible with a vanishing EDM value.

EDM searches on charged particles like protons and deuterons cannot be based on the same approach as for neutral particles, since the application of electric fields would result in an acceleration of the particle; therefore the use of storage rings in experiments aiming to directly measure a non-vanishing EDM on charged particles has been suggested by scientific collaborations all around the world.

The ideal scenario would be an EDM-search dedicated electric storage ring to be developed on purpose to perform an EDM measurement on proton. As a first step towards a dedicated storage ring, feasibility studies on deuteron beams are performed by the JEDI (Jülich Electric Dipole Investigations) collaboration at the magnetic storage ring COSY (Cooler Synchrotron) at Forschungszentrum Jülich in Germany.

The idea is based on the manipulation of the spin of the particles in the ring by use of a particular kind of radio frequency Wien Filter which acts on particles EDM leaving their orbit unperturbed, in such

a way to obtain a beam vertical polarization build-up which is proportional to the EDM value. The polarization-induced asymmetry in beam particles elastically scattered off a target, proportional to beam polarization, is then measured via a polarimeter and it is possible to obtain a value for the EDM.

The cycles of tests that led to the development of the prototype of such a high precision polarimetry detector, made of a number of LYSO scintillator crystal modules and with a readout system based only on Silicon Photomultipliers (SiPMs), is the topic of the present thesis. In chapter I the theoretical background is presented. Chapter II is dedicated to a detailed description of the main principles in the use of storage rings for EDM searches in charged particles. Chapter III is a description of the COSY facility at FZ-Jülich and in chapter IV all the results from the tests performed in the development of the LYSO polarimeter are presented in detail.

CHAPTER 1 - Theoretical Background

The interest to search for permanent electric dipole moments (EDMs) of elementary particles is presented in this chapter. The theoretical background of elementary particles EDMs is also described.

1.1 Matter over anti-matter imbalance and discrete fundamental symmetries

1.1.1 Matter-antimatter imbalance

One of the most important unanswered scientific question of the 20th century is the existing asymmetry between matter and anti-matter in our universe. The established Standard Model of particle physics (SM) fails to explain the reason for the measured abundance of matter over anti-matter.

This matter-antimatter discrepancy derives from the baryon-antibaryon asymmetry η_{BA}, defined as the difference of baryon density n_B and the anti-baryon density $n_{\bar{B}}$ normalized to the photon density n_γ [1] [2].

$$\eta_{BA} = \frac{n_B - n_{\bar{B}}}{n_\gamma} \tag{1.1}$$

The baryon-antibaryon asymmetry η_{BA} is one of the relevant parameters of the standard cosmological model, and measurements have been performed by astrophysics experiments (CMS and BBN above all) to determine it.

The results of both these measurements are consistent with each other and can be found in [3] [4].

$$\eta_{BA} = \frac{n_B - n_{\bar{B}}}{n_\gamma} = (6.09 \pm 0.06) \cdot 10^{-10}\ (CMB), \tag{1.2}$$

$$5.8 \cdot 10^{-10} \leq \eta_{BA} \leq 6.6 \cdot 10^{-10}\ (BBN, 95\%\ C.L.) \tag{1.3}$$

In absence of CP violation, the expectation is of an equal amount of matter and antimatter produced in the Big Bang. Cosmological model and SM calculations lead to an asymmetry parameter of [5]

$$\eta_{BA} = 10^{-18} \tag{1.4}$$

The results of the performed measurements and the theoretical prediction differ by eight orders of magnitude.
Two solutions have been proposed to solve this discrepancy:

- Separated matter and antimatter regions exists in the universe and we live in the 'matter-dominated' one.

- An asymmetry in the matter-antimatter annihilation process must have occurred in the early universe resulting in matter-dominated universe.

In order to prove the first assumption the experiment AMS-02 (*Alpha Magnetic Spectrometer*) is ongoing aboard the International Space Station searching for heavy anti-nuclei. The measurement of such a heavy anti-nucleus could be a proof of the existence of 'antimatter-dominated' regions in our universe [6] [7].

In 1967 Sakarov proposed three conditions for the so called *baryogenesis* (i.e. the generation of baryons in the early universe) to explain the asymmetric annihilation of matter and anti-matter:

Baryon number violation: some mechanism must exist which violates the baryon number conservation, otherwise there would be no asymmetry between baryons and anti-baryons.

Violation of C and CP symmetries: the process must violate the charge conjugation symmetry (C) and the combination of charge and parity transformation symmetry (CP). These symmetry breaking processes are necessary to produce an imbalance of baryons and anti-baryons.

Thermal non-equilibrium: The process must take place in a condition of thermal non-equilibrium, otherwise each sub-process would occur as often as its reverse process and this would not lead to a net change in the baryon number.

The Standard Model includes the description of CP violating processes, but their effect is way too small to produce the measured asymmetry of baryons and anti-baryons, it is then necessary to search for CP violating processes beyond the SM, one of these could manifest in a permanent EDM of charged elementary particles.

1.1.2 Physical symmetries and their transformations

Symmetries play a fundamental role in physics, as they are directly linked to conservation laws. In particle physics three main discrete symmetry transformations are considered: the parity transformation (P), the charge conjugation transformation (C) and the time reversal transformation (T), a brief definition of each is given below.

Parity transformation: the parity transformation P reverses the coordinates of a spatial vector in a physical process $(\vec{x} \rightarrow -\vec{x})$, the time coordinate stays the same.
A P-symmetric process behaves exactly as its mirror image process.

Charge conjugation transformation: the application of the charge conjugation transformation changes a particle into its anti-particle, changing the sign of its charge.

Time reversal transformation: the time reversal transformation changes the sign of the time coordinate leaving the spatial coordinates unchanged $(t \rightarrow -t,\ \vec{x} \rightarrow \vec{x})$.
A time reversed T-symmetric physical process would lead to the same rates as the unreversed one.

1.1.3 Combination of charge and parity transformation

A first indirect CP-violating process was observed in 1964 via the measurement of the kaon decay K_L^0 particles [8].
This observed CP violating process was included in the SM of particle physics by introducing the unitary CKM-matrix (*Cabibbo-Kobayashi-Maskawa*). However this matrix is not sufficient to describe the asymmetry between matter and antimatter in the universe, therefore additional sources of CP violating processes, beyond the SM, are of interest to explain this asymmetry.
The existence of permanent EDMs in elementary particles could be the consequence of one of these sources. Next section will give a description of the theory behind the EDM of elementary particles as well as an explanation for the importance of its measurement and for the behavior of EDMs under symmetry transformations.

1.2 Electric Dipole Moments

1.2.1 Definition of Electric Dipole Moment

In classical physics an EDM is described as the charge separation along the spatial vector $\vec{r}$:

$$\vec{d} = \int_V \rho(\vec{r}) \cdot \vec{r} d\vec{r} \tag{1.5}$$

Where $\rho(\vec{r})$ describes the spatial charge density. In particle physics the EDM is a property of the particle itself, the alignment of the EDM is either parallel or antiparallel to the particle spin $\vec{S}$ [9] because the spin quantization axis is the only observable direction.
The definition of EDM $\vec{d}$ and its magnetic analogue $\vec{\mu}$ (Magnetic Dipole Moment, MDM) is given in equation (1.6)

$$\vec{d} = \eta_{EDM} \frac{q}{2mc} \vec{S}$$
$$\vec{\mu} = g \frac{q}{2m} \vec{S} \tag{1.6}$$

The values q and m define the charge and the mass of the particle, the constant c is the speed of light. The particle has a g-factor defining its MDM, η_{EDM} is defined in analogy to the g-factor.
The Hamiltonian H of a particle at rest, immersed in an electric and a magnetic field is:

$$H = -\vec{\mu} \cdot \vec{B} - \vec{d} \cdot \vec{E} \tag{1.7}$$

The application of parity and time reversal transformations to the Hamiltonian results in:

$$P\text{: } H = -\vec{\mu} \cdot \vec{B} + \vec{d} \cdot \vec{E}$$
$$T\text{: } H = -\vec{\mu} \cdot \vec{B} + \vec{d} \cdot \vec{E} \tag{1.8}$$

As it's possible to see, the parity transformation leaves the magnetic term unchanged (both spin vector and magnetic field have eigenvalue $= +1$), the electric field flips (it has eigenvalue $= -1$) thus the product of EDM $\vec{d}$ and the electric field $\vec{E}$ results in a sign change in the Hamiltonian, which is a parity violating process.
The application of time reversal transformation shows the EDM is also a symmetry violating process, the magnetic field and the spin both reverse their sign under time reversal operator. Therefore a non-vanishing EDM $\vec{d}$ violates time reversal symmetry.
Assuming the CPT theorem to hold, a time reversal symmetry violating process leads directly to a CP violation process.
In figure (1.1) the parity and time reversal transformations for an elementary particle are illustrated.

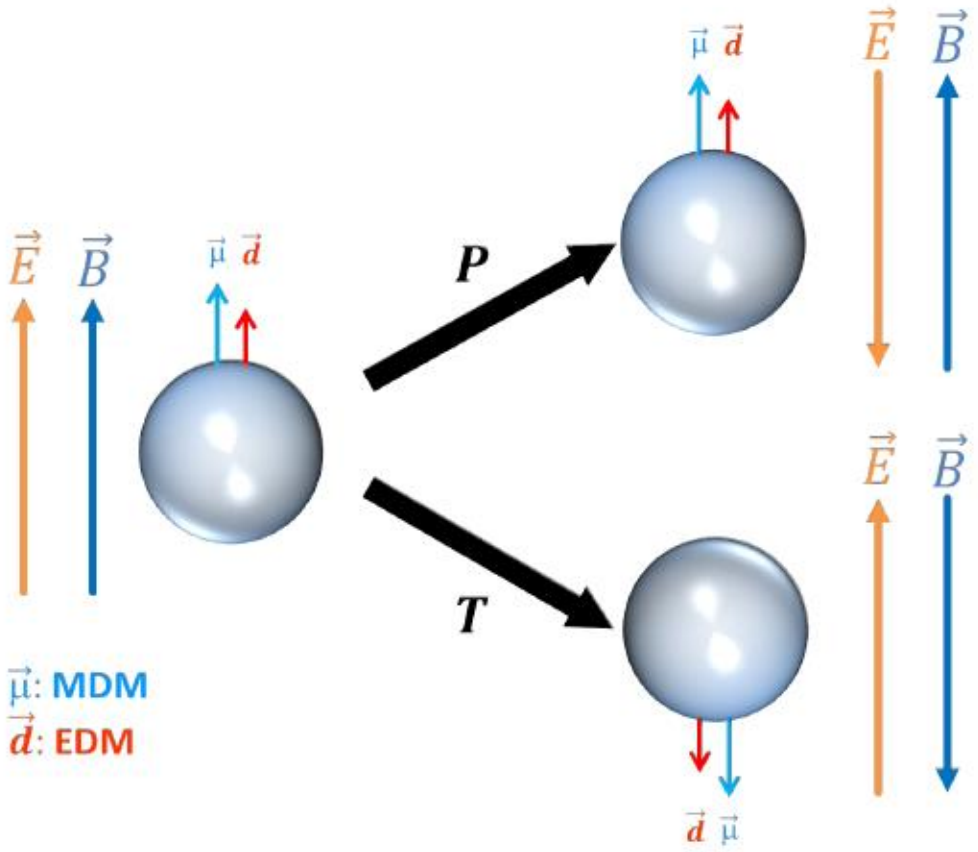

Figure 1.1 - Sketch of an elementary particle with an electric and a magnetic dipole moment immersed in an electric and a magnetic field. The EDM and the MDM are aligned to the electric and magnetic field. The application of parity transformation causes a flip in the electric field, the time reversal transformation flips the sign of the magnetic and electric dipole moment and the magnetic field. Both transformation are symmetry violating.

1.2.2 EDMs experimental measurements

In order to observe new CP violating processes many experiments have been performed in the past decades, based on the application of combined $\vec{E}$ and $\vec{B}$ fields applied to particles stored inside a trap. Since the application of electric and magnetic fields on charged particles would accelerate them out of the trap, it's clear that this approach is limited to neutral entities, like neutrons, atoms or molecules.

This 'traditional' approach aims to measure the spin precession frequency of a trapped neutral particle with a magnetic and an electric field applied.

A $\vec{B}$ field is applied to the particle and its spin starts preceding about the field axis because of the interaction between the field and the magnetic dipole moment MDM. Then an $\vec{E}$ field is applied that gives a contribution to spin precession frequency due to the interaction with the electric dipole moment EDM.

In order to disentangle the frequency contribution given by EDM from the one given by the MDM the $\vec{E}$ field is continuously flipped, switching from parallel to anti-parallel to $\vec{B}$. The difference between spin precession frequencies measured with the electric field in parallel and anti-parallel direction gives an information on the entity of the EDM $|\vec{d}|$:

$$|\vec{d}| = \hbar \frac{\omega_{E+} - \omega_{E-}}{4|\vec{E}|} \tag{1.9}$$

In figure (1.2) a description of this procedure is illustrated.

Figure 1.2 - 'Traditional' approach for EDM measurement, limited to neutral particles, atoms or molecules. μ = Magnetic Dipole Moment, d = Electric Dipole Moment, B = Magnetic field, E = electric field, hf = spin precession frequency.

The first measurement of an EDM was performed for the neutron in 1949 and the result was published in 1957 [10].
The first limit for the neutron EDM was calculated to:

$$d_n = (-0.1 \pm 2.4) \cdot 10^{-20}\, e \cdot cm \tag{1.10}$$

The measurement techniques and the control of the systematics have been considerably improved in the last 60 years and the upper limit of the neutron EDM decreased.
In the following, a few upper limits for EDM of different experiments are presented, figures (1.3) and (1.4) show a time evolution of these limits for neutron and other elementary particles:

- Ultra-cold neutrons: $d_n \leq 3 \cdot 10^{-26}\, e \cdot cm \quad (95\%\ C.L.)$ [11]
- Derived from the polar molecule monoxide: $d_e \leq 8.7 \cdot 10^{-29}\, e \cdot cm$ $(95\%\, C.L)$ [12]
- Neutral ^{199}Hg atoms: $d_{^{199}Hg} \leq 7.4 \cdot 10^{-30}\, e \cdot cm \quad (95\%\ C.L.)$ [13]
- Derived from the atomic ^{199}Hg EDM measurement: $d_p \leq 2 \cdot 10^{-25}\, e \cdot cm$ $(95\%\, C.L.)$ [14]
- Spin precession data from the muon g-2 experiment: $d_\mu \leq 1.8 \cdot 10^{-19}\, e \cdot cm$ $(95\%\, C.L.)$ [15]

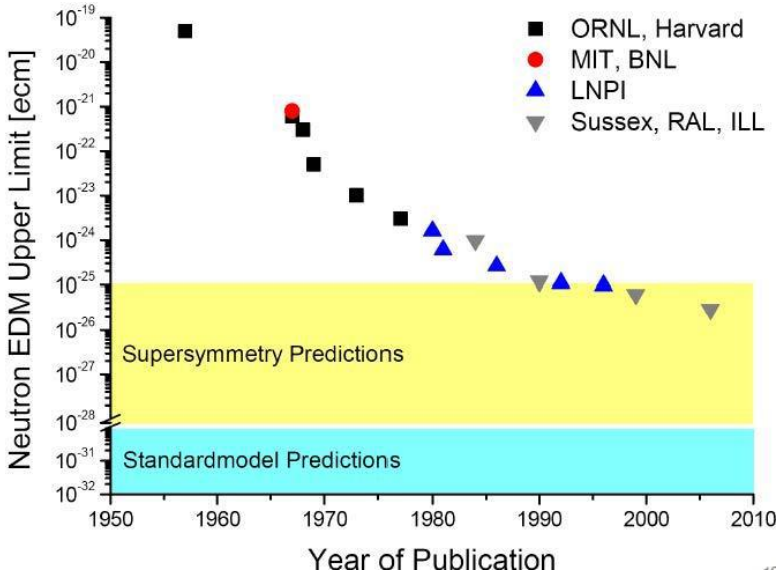

Figure 1.3 - Time evolution of neutron EDM upper limit

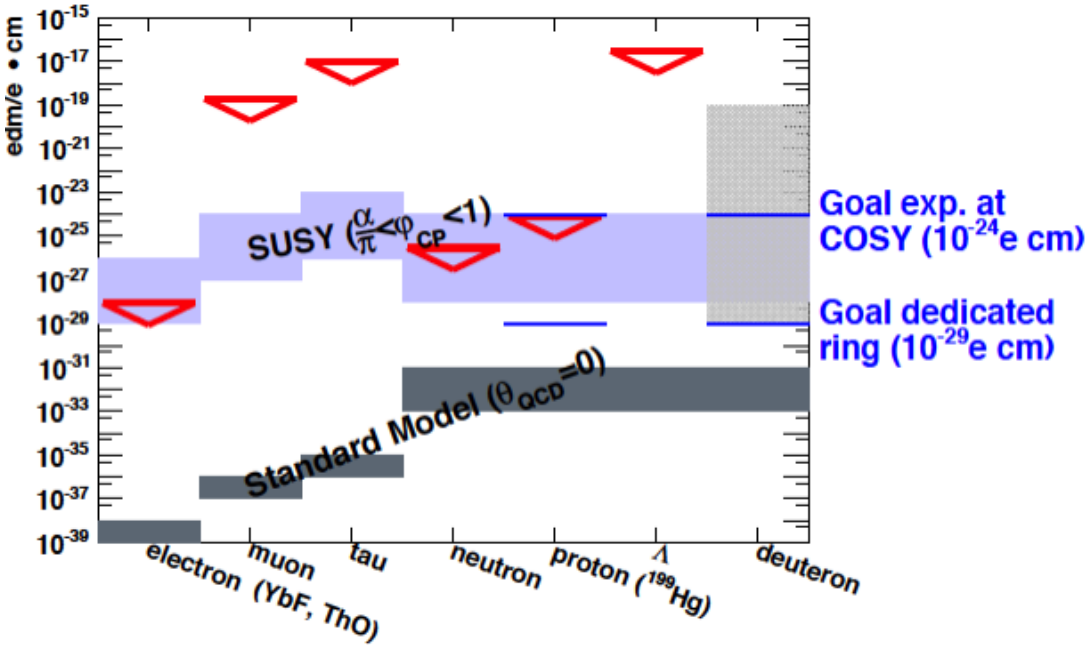

Figure 1.4 - Time evolution of EDM upper limit for various elementary particles and comparison between SM and SUSY models.

The different EDM measurement results are compatible with zero.
To find physics beyond the SM, high-precision experiments are performed like the permanent EDM searches of elementary particles or high-energy physics (e.g. with LHC at CERN).
The EDM limits of the proton and electron are calculated by measurements of neutral atoms, theoretical knowledge is taken into account to derive these EDM limits [14].

As mentioned before, the application of combined $\vec{E}$ and $\vec{B}$ fields on a charged particle would result in an acceleration of that particle, which could not stay inside the trap anymore. Therefore, the concept of using particle storage rings for trapping charged particles for a direct EDM measurement is considered.
In the next chapter a description of the proposed EDM measurement technique using storage rings is given.

CHAPTER 2 - EDM measurements in storage rings

This section is dedicated to the description of EDM measurement techniques by use of a storage ring, a description of the main principle applied to pure magnetic rings as well as to combined electric and magnetic rings is given. The proposed RF Wien filter method for pure magnetic rings is also explained.

2.1 EDM searches in storage rings

2.1.1 Main principle

The idea for a particle EDM measurement in a storage ring is based on the interaction between an electric field $\vec{E}$ and the dipole moment $\vec{d}$ of the particle. Since the spin is the only vector of an elementary particle defining a direction, the EDM vector must lie on the same direction of the spin vector. For a non-vanishing EDM this interaction leads to a polarization build-up. The time evolution of the spin vector is described by the equation (2.1) [16]:

$$\frac{d\vec{S}}{dt} = \vec{d} \times \overrightarrow{E_*} \tag{2.1}$$

Where $\overrightarrow{E_*}$ denotes the electric field in the particle rest frame.
In figure (2.1) a generic EDM measurement procedure is illustrated. The polarization vector lies initially in the horizontal plane, the interaction between the electric field and the EDM then rotates it

upwards or downwards out of the plane, and the vertical component of the oscillation can be measured by use of a polarimeter [16].

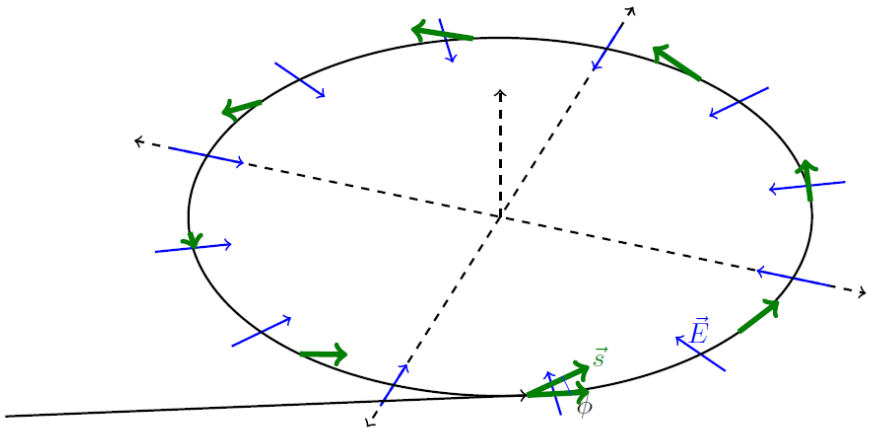

Figure 2.1 - Principle of an EDM measurement in a storage ring. Longitudinally polarized particles enter a storage ring. A radial electric field is used as a guiding field. An EDM will tilt the spin in the vertical direction. The vertical polarization can be measured by use of a polarimeter.

If the effect of a magnetic field interacting with particles' MDM is also taken into account, the spin motion is governed by the Thomas-BMT equation, which in case of electric and magnetic fields perpendicular to the beam direction ($\vec{v}\cdot\vec{E} = \vec{v}\cdot\vec{B} = 0$) has the form [16]:

$$\frac{d\vec{S}}{dt} = \vec{S} \times \vec{\Omega} \tag{2.2}$$

With $\vec{\Omega}$:

$$\vec{\Omega} = \frac{e\hbar}{mc}\left[G\vec{B} + \left(G - \frac{1}{\gamma^2 - 1}\right)\vec{E} \times \vec{v} + \frac{1}{2}\eta_{EDM}\left(\vec{E} + \vec{v} \times \vec{B}\right)\right] \tag{2.3}$$

Where $G = 0.5(g-2)$ is the anomalous g-factor, γ is the usual Lorentz relativistic factor and η_{EDM} is the EDM parameter.

Equation (2.2) is a starting point for different possible approaches, in general it is useful to eliminate the terms containing G since spin motions driven by MDM are usually much larger than the ones driven by the tiny EDM effect.
The following sections analyze the approaches based on the different nature of the storage rings.

2.1.2 Pure electric storage ring

In a pure electric storage ring (i.e. $\vec{B} = 0$) eq. (2.2) changes in such a way that it is possible to eliminate the terms containing G, and thus the contribution of the MDM, if the additional condition:

$$\left(G - \frac{1}{\gamma^2 - 1}\right) = 0 \tag{2.4}$$

is fulfilled. Then eq. (2.2) reduces to:

$$\frac{d\vec{S}}{dt} = \frac{e\hbar}{2mc}\eta\vec{S} \times \vec{\Omega} \tag{2.5}$$

Condition (2.4) can only be fulfilled by particles with $G > 0$ and only with a specific value of their momentum, usually referred to as "magic momentum", p_{magic}. For example, condition (2.4) can be achieved for protons with a momentum of $p_{magic} = 0.7\,GeV/c$, and using electric fields in the order of 10 MV/m results in a ring of about 40m radius. Such a pure electric ring was proposed at Brookhaven National Laboratory (BNL) to perform a measurement of the proton EDM [16].

2.1.3 Combined electric and magnetic ring

In a storage ring that makes use of a proper combination of $\vec{E}$ and $\vec{B}$ fields it is possible to eliminate the terms containing G in eq. (2.2) if the condition:

$$G\vec{B} + \left(G - \frac{1}{\gamma^2 - 1}\right)\vec{E} \times \vec{v} = 0 \tag{2.6}$$

is fulfilled. A combined electric and magnetic ring could achieve that also for particles with negative G, like the deuteron. Such a storage ring is under study by JEDI collaboration at Forschungszentrum Jülich [16].

2.1.4 Pure magnetic storage ring

The feasibility study which is being carried out by the JEDI collaboration at Forschungszentrum Jülich, aiming to perform a proof-of-principle measurement of deuteron EDM, is based on the use of the COSY storage ring, which is a pure magnetic driven ring.

In this case the factor $\vec{\Omega}$ from eq. (2.2) becomes:

$$\vec{\Omega} = \frac{e\hbar}{mc}\left(G\vec{B} + \frac{1}{2}\eta\vec{v} \times \vec{B}\right) \tag{2.7}$$

and the build-up of the EDM effect is less straightforward than in the previous cases.

The term containing G results in a spin precession in the horizontal plane of the storage ring and, because of this precession, the projection of the spin vector onto the plane containing particles'

momentum vector points parallel to momentum vector for 50% of the time, pointing anti-parallel for the remaining 50%.
An electric field is experienced by the particles in their rest frame, caused by the laboratory magnetic field, which interacts with the EDM and drives a 50%up-50%down motion of the spin due to the oscillating behavior of the spin vector projection. No net vertical polarization is then built up.
In order to allow for a sufficient polarization build-up in the ring, JEDI collaboration at Forschungszentrum Jülich is developing a method based on the use of a particular kind of Wien Filter which, operated at a proper resonance frequency, results in a net EDM-induced polarization build-up of the beam. In next section a more detailed description of this method is given.

2.1.5 RF Wien Filter

As illustrated in the previous section, in a pure magnetic storage ring, the oscillating behavior of the spin vector projection onto the beam plane, caused by spin precession, drives a 50%up-50%down spin motion, due to the interaction between motional electric field, $E^* = v \times B$, induced in the particle's rest frame by dipole magnets field and the EDM. So there is not any net vertical polarization build-up. In figures (2.2) and (2.3) this process is illustrated [17].

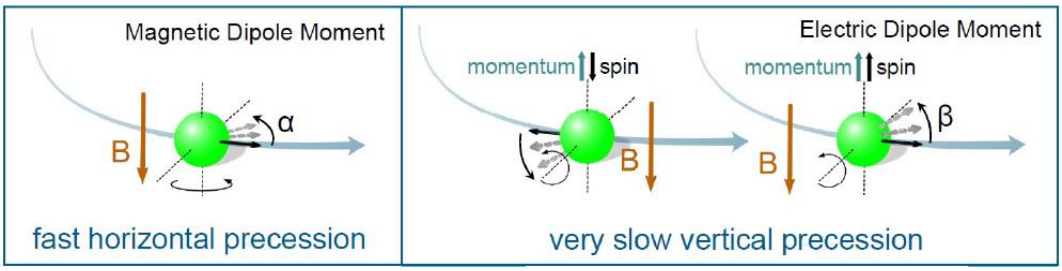

Figure 2.2 - Left: MDM-driven fast precession of the spin vector in the beam plane. Right: EDM-induced very slow vertical precession of the spin vector. Up when spin and momentum vectors are parallel and down when they are antiparallel.

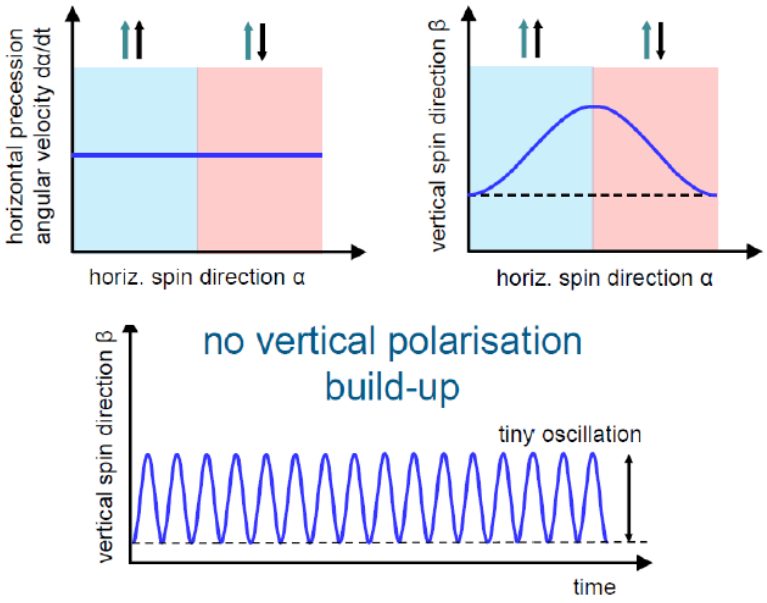

Figure 2.3 - Upper Left: the angular velocity of the spin horizontal precession motion is constant over one whole precession cycle, and thus (Upper right) the contributions to vertical polarization given by EDM cancel out. As a result at the bottom part of the figure the time behavior of the spin vertical component is shown. No net vertical polarization builds up over time.

The aim of the RF Wien Filter design is to obtain a tool capable of braking the symmetry between up and down spin motion without interfering with particles' orbital trajectory, and thus building up vertical polarization.

The use of a proper $\vec{E}$ and $\vec{B}$ fields combination with the constraint:

$$\vec{E} + \vec{v} \times \vec{B} = 0 \tag{2.8}$$

Applied in one point along the magnetic storage ring, will not affect particles' momentum but will perturb spin precession $(\overrightarrow{B_*} \neq 0)$ in such a way that the spin projection symmetry between parallel and anti-parallel to momentum vector no longer holds, then a vertical polarization can build up and be detected as an EDM signal. Figure (2.4) illustrates this method.

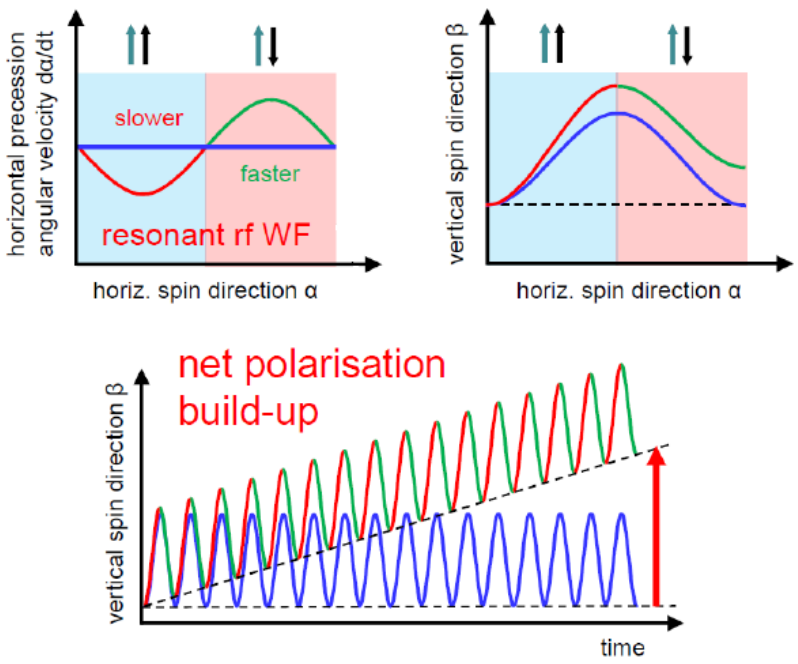

Figure 2.4 - Upper left: the B field introduced by the Wien Filter affect horizontal precession angular velocity in such a way that, over one precession cycle, spin vector points in one direction longer than in the other. Thus (upper right) after one whole spin precession cycle a tiny net vertical polarization remains. As a result in the bottom part of the figure the time behavior of the spin vertical component is shown. Net vertical polarization build-up over time is possible. In order for this method to work, E and B fields of the RF Wien Filter must be always in phase with the horizontal spin precession.

From these considerations it's clear that, in order for this procedure to work properly, the $\vec{E}$ and $\vec{B}$ fields of the RF Wien Filter must be always in phase with the horizontal spin precession.
The correct resonance frequency at which RF Wien Filter must work is given by:

$$f_{Wien} = (k + \gamma G) f_{REV} \tag{2.9}$$

With k being an integer and f_{REV} the revolution frequency of the particles in the ring [17].
This kind of approach is under study at the Forschungszentrum Jülich and could be performed at the existing COSY ring.
In figure (2.5) this RF Wien Filter approach to the EDM measurement is illustrated.

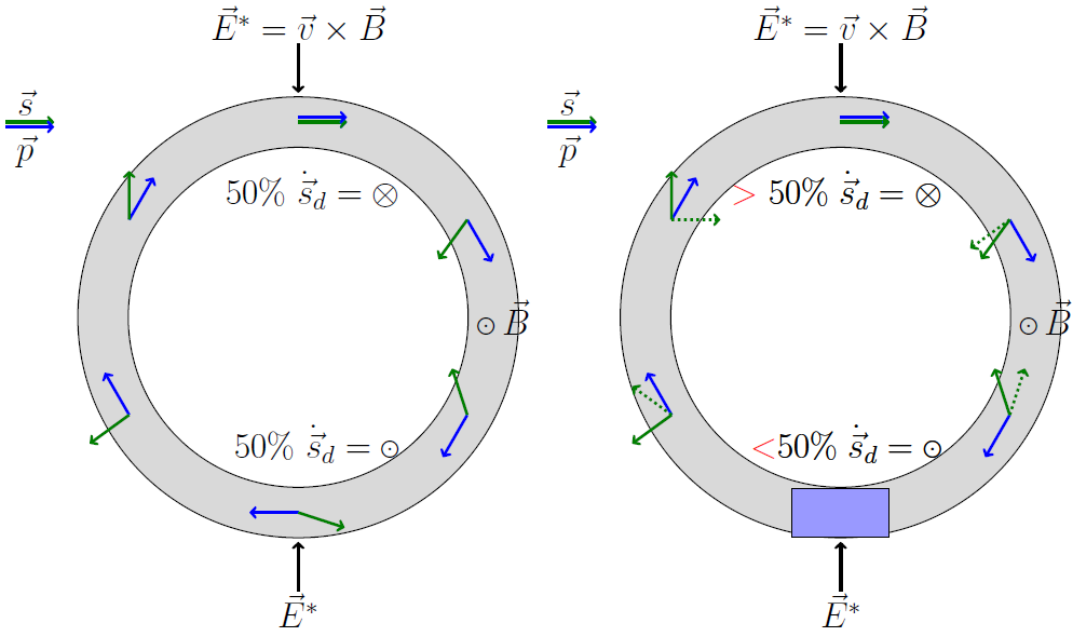

Figure 2.5 - Measurement of EDM in a pure magnetic ring: Left: in a pure magnetic ring particles experience a redial electric field $\vec{v} \times \vec{B}$. That causes an EDM-driven tilt of the spin vector out of the plane, in the upper hemisphere if the spin points parallel to the momentum vector and in lower hemisphere if it points antiparallel. This leads to an up-down motion of the spin vector due to the EDM and no vertical polarization can build up. Right: a Wien Filter (blue box in figure) will not affect particles' momentum ($\vec{E} + \vec{v} \times \vec{B} = 0$) but will influence the spin motion (dotted arrows in figure) in such a way that it will point for more than 50% of the time in one direction. As a result a vertical polarization due to the EDM can build up.

A more detailed description of the COSY ring and of the main polarimetry measurements performed by use of COSY is given in the next chapter.

CHAPTER 3 - The Cooler Synchrotron (COSY) storage ring

In the following sections a description of the COSY storage ring complex is given, along with a quick overview on most important spin-related quantities measured at COSY.

3.1 The COSY storage ring facility

3.1.1 Main storage ring

The storage ring COSY at Forschungszentrum Jülich (FZJ) is a particle accelerator facility designed to provide polarized proton and deuteron beams. Polarized beams are available for internal as well as external experiments. In this accelerator complex many devices for particle beam polarization manipulation are available, making it an ideal starting point as a test facility for a future EDM dedicated ring.

The facility consists of a polarized ion source, the cyclotron JULIC that operates an acceleration on the particles coming from the source and injects the beam into the ring, and the COSY storage ring itself, equipped with a beam extraction line that leads the beam to several external experimental areas [18].

A sketch of the COSY storage ring facility is shown in picture (3.1).

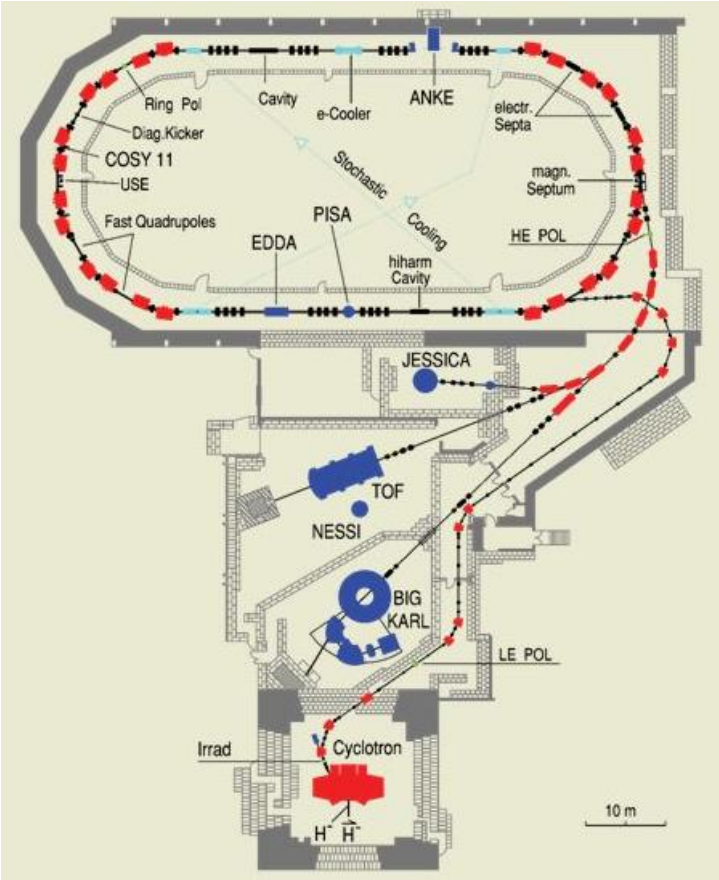

Figure 3.1 - Sketch of the COoler SYnchrotron (COSY) at Forschungszentrum Julich. The accelerator facility comprises polarized ion source, the cyclotron JULIC and the storage ring COSY. Blue elements are internal and external experimental places. Red elements are beam manipulation and preparation elements (like cyclotron and steering magnets). Light blue elements are beam cooing devices.

COSY is a 184m long race-track storage ring that can store a number of particles typically in the order of 10^{10} with a momentum up to 3,7 GeV/c. Its most distinctive feature is the beam cooling, intended as a shrinking of the beam phase-space surface, that improves the quality of the beam.

For beams with a momentum up to 600 MeV/c for protons and up to 1200 MeV/c for deuterons the so called electron cooler is used, which is placed in the straight section of COSY. It works by injecting into the beamline an electron beam at the same velocity and position of the main hadron beam. The phase-space surface of the electron beam is considerably smaller than the hadron beam's and, through Coulomb

interaction, transverse momentum of the main hadron beam can be transferred to the electron beam which is then extracted from the beamline leaving a hadron beam characterized by a reduced phase-space surface, thus by a higher quality [19].
Stochastic cooling is used for higher momenta instead, starting from roughly 1500 GeV/c on.

3.1.2 Polarized source

The COSY polarized particle source is a colliding beam source. The basic principle consists in creating a beam of electrically neutral, polarized hydrogen or deuterium atoms and make it collide with a beam of atomic cesium, causing one electron to be transferred from a cesium atom to a polarized hydrogen or deuterium atom [20]. The nucleus polarization is preserved in the resulting negative ions that can be then extracted and sent to the cyclotron, where they are accelerated and injected into COSY. Figure (3.2) shows a layout of the source.

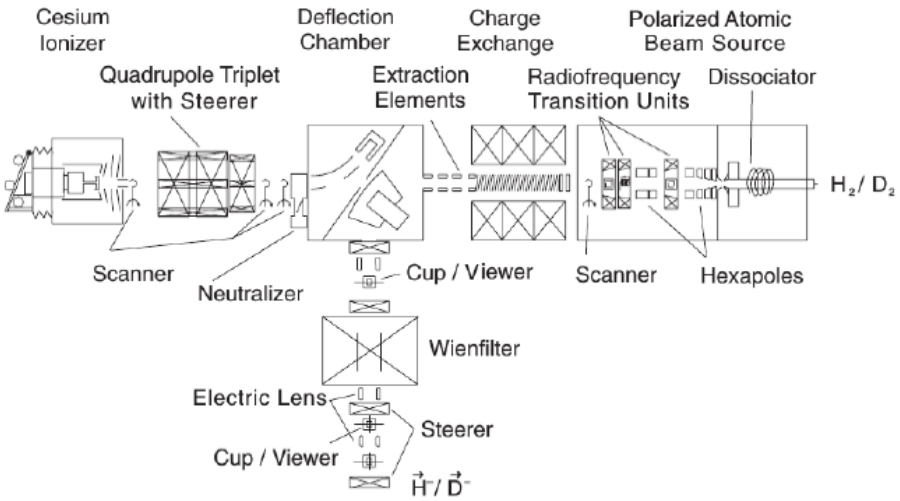

Figure 3.2 - Polarized beam source at COSY [21]. The Cesium beam is produced in the left branch of the T-shaped layout, the hydrogen or deuterium polarized beam is produced in the right branch. Negative ions produced by the collision of the two beams are extracted through the branch at the bottom of the figure.

The atomic beam source first dissociates hydrogen or deuterium molecules into single atoms by use of an electric discharge, atoms pass through a magnetic hexapole which acts as a focusing magnet and outputs a radially polarized beam. Different combinations of vector and tensor polarization are achievable [21].
The Cesium beam is the second part of the polarized source. Cesium atoms are first ionized, brought to neutrality in a cesium vapor chamber and then accelerated to 45 KeV to have an optimized cross section for the charge exchange reaction.
The two beams collide in a central region of the source dedicated to the charge exchange, placed inside a solenoid which determines spin quantization axis. The charge exchange reaction $H + Ce \rightarrow H^- + Ce^+$ prompts negative ions that can be extracted and, after passing a Wien Filter that rotates particles' spin in order to match the direction of the magnetic field in the cyclotron, they are sent to the cyclotron that operates an acceleration up to 300 MeV/c for protons or 600 MeV/c for deuterons. The beam is then injected into COSY through a 100m long injection line.

3.2 Polarimetry measurements at COSY

3.2.1 EDDA

As described in the previous chapter, an EDM signal can be detected by use of a polarimeter, a detector that measures the rate asymmetry in the azimuthal direction of a nuclear scattering process between a polarized particle beam and a target.
From the rates measured is then possible to infer information on beam polarization.
The EDDA (Elastic Dibaryons, Dead or Alive?) detector, placed in a straight section of COSY, can be used as a polarimeter to measure the

vertical and in-plane polarization. The detector is made of a number of plastic scintillators arranged in two layers, in the inner layer 32 plastic scintillator bars are parallel to the beam and in the outer layer ring-shaped plastic scintillators are placed around the beam. Figure (3.3) shows a picture of EDDA.

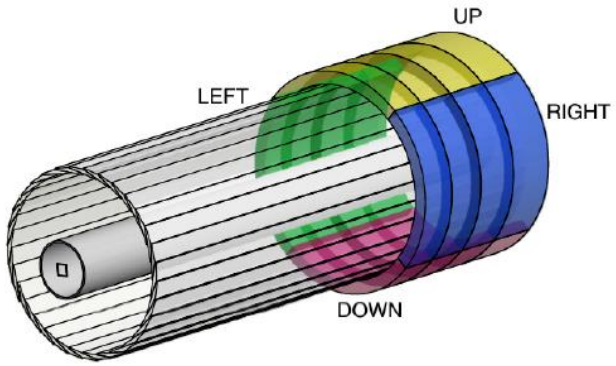

Figure 3.3 - Layout of EDDA detector [22]. Only ring used in polarization measurements are shown.

In polarimetry experiments, scintillator bars in EDDA are divided into four groups, each group for one cardinal direction. Vertical polarization can be obtained directly from the asymmetry between left and right count rates. In-plane polarization could in principle be assessed starting from the up-down count rate asymmetry, but the rapid spin precession motion, with a rate in the order of 120 kHz, makes this task hard to accomplish. The in-plane polarization requires a more complicated procedure, described in section 3.2.5.
In the following sections a definition of the most relevant physical quantities involved in polarimetry measurements is illustrated.

3.2.2 Differential cross sections

Polarized particle beams behave differently from unpolarized ones when involved in nuclear scattering reactions. In a reaction involving an unpolarized beam the only defined direction is the beam

axis, the distribution of scattered particles is then invariant for rotations about the beam axis. A polarized beam introduces an additional defined direction, namely the polarization vector, so that the distribution of scattered particles, and thus differential scattering cross sections, are no longer independent of the azimuth. This azimuthal asymmetry is the basis for all hadron polarimeters.
In the following a definition of differential scattering cross section is given, along with the most relevant polarimetry observables.
The coordinate system outlined is illustrated in fig (3.4):

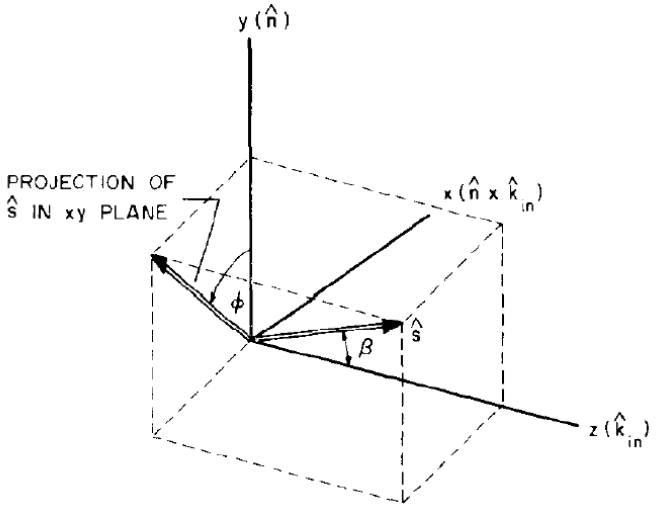

Figure 3.4 - Coordinate definitions for polarized particle scattering

If we let $\hat{k}_{in}$ be the incident particle momentum vector and $\hat{k}_{out}$ the outgoing particle momentum vector, the z-axis is defined as the axis parallel to $\hat{k}_{in}$, the y-axis parallel to $\hat{k}_{in} \times \hat{k}_{out}$, the x-axis forming a right-handed system with the other two. Φ is the angle between y-axis and the projection of the spin vector onto the xy-plane, β is the angle between the spin axis and the z-axis, the left side of a general polarimetry detector is at $\phi = 0°$, right side is at $\phi = 180°$, up is at $\phi = 270°$ and down at $\phi = 90°$.

The so called Analyzing Power **A** defines the dependence of scattering reactions on the beam polarization, for a spin-1/2 particle the differential cross section is given by:

$$\sigma(\theta,\phi) = \sigma_0(\theta)\left(1 + \vec{P}\vec{A}(\theta)\right) \tag{3.1}$$

With θ being the scattering angle and σ_0 the non-polarized cross section. With the additional assumption $\beta = 90°$ it simplifies to:

$$\sigma(\theta,\phi) = \sigma_0(\theta)\left(1 + A_y P\cos(\theta)\right) \tag{3.2}$$

With $P = \left|\vec{P}\right|$.
Differential cross section for spin-1 particles has a similar form but it also takes into account the tensor Analyzing Power:

$$\sigma(\theta,\phi) = \sigma_0(\theta)\left(1 + \frac{3}{2}\vec{P}\vec{A} + \frac{1}{3}\sum\nolimits_{ij} P_{ij}A_{ij}\right) \tag{3.3}$$

Where $\vec{A}$ is vector Analyzing Power and A_{ij} is tensor Analyzing Power, the components A_{yz} and A_{xy} violate parity and go to zero as nuclear scattering is dominated by strong interaction [rif]. As tensor polarization, also tensor Analyzing Power has no trace:

$$A_{xx} + A_{yy} + A_{zz} = 0$$

With this and the additional simplifying assumption $\beta = 90°$ the differential cross section becomes:

$$\sigma(\theta,\phi) = \sigma_0(\theta)\left(1 + \frac{3}{2}P_{vec}A_y\cos\phi + \frac{1}{2}P_{tens}\left(A_{xx}\sin^2\phi + A_{yy}\cos^2\phi\right)\right) \tag{3.4}$$

The vector polarization has a 2π-periodic modulation in ϕ, the effect of tensor polarization is π-periodic.

3.2.3 Relevant polarimetry observables

Equations (3.1) and (3.4) are the basis for all polarization measurements.

The beam polarization can be inferred from rates asymmetries measured via a polarimeter if the Analyzing Power is known, different asymmetries can be constructed by the four rates, as summarized in table 3.1:

Asymmetry	Statistical Uncertainty	Polarization Observables
$\varepsilon_{\text{vec}} = \frac{L-R}{L+R}$	$\sqrt{\frac{1-\varepsilon_{LR}^2}{L+R}}$	$\frac{3}{2}\frac{P_{\text{vec}}A_y}{1+\frac{1}{2}P_{\text{tens}}A_{yy}}$
$\varepsilon_{\text{tens}} = \frac{(L+R)-(U+D)}{(L+R)+(U+D)}$	$\sqrt{\frac{1-\varepsilon_{\text{tens}}^2}{(L+R)+(U+D)}}$	$\frac{P_{\text{tens}}(A_{yy}-A_{xx})}{1+\frac{1}{4}P_{\text{tens}}(A_{yy}+A_{xx})}$

Table 3.1 – Observables in spin-1 polarimetry measurements and their statistical uncertainty [23]. L, R, D and U stand for the rates in each direction

Table 3.1 shows the main asymmetries for a spin-1 particle like the deuteron. Vector polarization is calculated from left-right rate asymmetry, For tensor polarization the difference between rates in the horizontal and vertical plane is used. Statistical errors in table 3.1 are given under the assumption that rate errors are simply counting errors $\sigma_N = \sqrt{N}$.

3.2.4 Errors in polarization measurements

In order to have an information on the relative error on the asymmetries, a Figure of Merit (FoM) can be defined as σA_y^2 for vector polarization (with σ = cross section and A_y = y-component of vector

analyzing power) and for tensor polarization as $\sigma(A_{yy} - A_{xx})^2$, this figures are inversely proportional to the squared relative error for $\varepsilon \approx 0$ [23].

Polarization measurements are also affected by several systematic errors, the most relevant sources of which are usually detector efficiency and beam alignment issues.

The efficiency of the detector is not uniform over detector volume, so the number of event each side misses can be different and build a fake asymmetry.

A misalignment in the beam position means that the two sides of the detector are not at the same exact scattering angle, inducing a systematic error in cross sections and analyzing power measurements, which are function of the azimuthal angle θ [24].

In order to address the problem of systematic errors, different polarization states can be compared. The polarization of an unpolarized beam, which polarization is known to be precisely zero, can be measured so that any asymmetry detected must be a systematic error and can be used to correct measurements with polarized beams.

Another method makes use of the so called Cross Ratio, that mixes positive and negative polarization states:

$$\varepsilon_{CR} = \frac{r-1}{r+1} \tag{3.5}$$

With:

$$r^2 = \frac{L_+ R_-}{L_- R_+} \tag{3.6}$$

Where $L_\pm$ and $R_\pm$ are event rates in the left and right side of the detector for positive and negative polarization states [24].

3.3 measurement of horizontal polarization

As introduced in section 3.2.1, the measurement of in-plane polarization requires a more complicated method with respect to calculation of the vertical polarization. The fast precession motion of the horizontal polarization, with a rate of about 120kHz, makes necessary the use of a dedicated procedure.
The development, at Forschungszentrum Jülich, of a "*time-stamp system*" made possible recording horizontal polarization as a function of time. In the following a description of the experimental cycles within which this method has been used is given.

3.3.1 Experimental cycle with the *time-stamp system*

A vertically polarized beam is injected into COSY and the polarization is then rotated in the horizontal plane by use of an rf-solenoid which operates at the spin resonance frequency given by:

$$f_{res} = f_{cyc}(1 - G\gamma) \tag{3.7}$$

Where f_{cyc} is the cyclotron frequency and $G\gamma$ is the spin-tune.
A Time-to-Digital Converter (TDC), created on purpose at FZJ, marked each polarimeter event with the elapsed time obtained from a continuously running clock.

Particle position in the beam bunch: The clock period of the TDC is set on a value of 92.59 ps, a much smaller value of COSY beam revolution time of 1.332 μs. This allows for a good resolution on longitudinal position within the beam bunch of a detected particle. The rf-cavity and the TDC must be calibrated in such a way that the turn number since the DAQ starts can be calculated, then it is

possible to use the fractional part of the turn number to obtain a map of the particle distribution in the beam bunch. It is then possible to interpret the fractional part of the turn number as the position of particles around the ring relative to the center of the bunch. Figure (3.5) shows a scatterplot of polarimeter events as a function of the fractional part of the turn number (vertical axis) and clock time (horizontal axis).

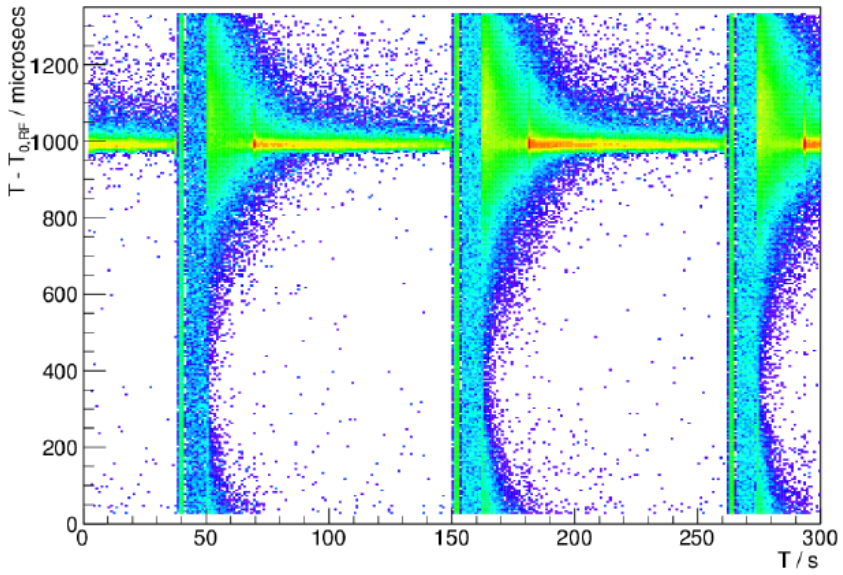

Figure 3.5 - Scatterplot of polarimeter events in function of the fractional part of the turn number (thus of the position in the ring) in the vertical axis, and in function of clock time in the horizontal axis. There is a sufficient amount of time for almost four machine cycles to be shown completely. The intensity scale starts with violet and proceeds to blue, green and yellow to red.

As it is shown in figure, when the cycle starts the beam is spread all over the ring (vertical axis range covered completely). In the first few seconds injection, ramping and bunching occur, along with the cooling system start. The bunching process shifts events from the area near 300 towards the center of the bunch around 1000 along vertical axis, electron cooling makes the bunch more compact (narrow yellow-red band). After about 30 seconds the extraction of the bunch onto polarimeter target starts and the height of the cooling peak

decreases until the beam is almost gone. One machine cycle is made of about 8.8×10^7 turns.

Total spin precession angle: In order to calculate the total spin precession angle only the integer part of the turn number is used.
The calculation process requires the knowledge of the spin-tune frequency $G\gamma f_{cyc}$ (about 120 kHz) that can be obtained from eq. (2.16) as follows:

$$G\gamma f_{cyc} = f_{cyc} - f_{res} \tag{3.8}$$

The rf-solenoid spin resonance frequency f_{res} is obtained using a variable-frequency scan across the resonance value and refined with a series of fixed-frequency scans to pinpoint the center of the resonance with an error of 0.2 Hz [25]. The total horizontal polarization precession angle is then calculated for each event as the product between the spin tune and the integer part of the turn number:

$$\omega_{TOT} = 2\pi G\gamma \cdot Int(N_{turns}) \tag{3.9}$$

Amplitude of U/D asymmetry: The polarization precession circle is divided into 9 bins and events from the up and down detector quadrants are individually sorted into each bin.
The main challenge comes from the high frequency of the polarization precession motion, in fact one full precession corresponds to only 6 turns of the COSY beam (~8.3 μs) while the rate of the elastic scattered particles is approximately one in 700 turns. In order to have significant statistics, an accumulation time of 3 seconds is adopted and the up-down asymmetry is calculated for each bin and its behavior is reproduced by a sine wave of variable amplitude and phase

(with a non-zero offset if there is a systematic difference between acceptance in different sides of the detector):

$$\frac{D-U}{D+U} = f(\omega) = A\sin(\omega+\phi)+B \tag{3.10}$$

The magnitudes of all 3-seconds accumulation times are then put together to create a history of the in-plane polarization during the store. Figure (3.6) illustrates the result of the procedure described above.

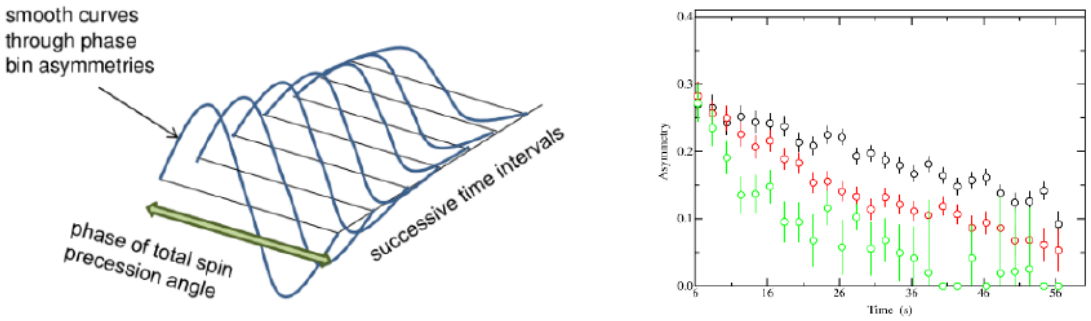

Figure 3.6 - Sketch of the procedure to extract the horizontal polarization as a function of time from the total spin precession angle. On the left panel are sine waves that represent the asymmetries in the circle of the total spin precession angle. The circle is divided in 9 bins and collects the events in a 3 second time window, according to the phase of the total precession angle in the horizontal plane. On the right panel there is one example of the horizontal polarization measurement for three different beam emittances from a large (green) to a small (black) size.

In order to refine the calculation process, the spin tune itself is varied over a small range in each accumulation time-window to find the value that gives the largest polarization amplitude. It is possible to find a peak in each time-window with FWHM of 1.8×10^{-6} of the spin tune value. Typically the spin tune can be known with a precision of 10^{-8} in an accumulation time-window and varies by 10^{-7} during a beam store, this variation seems to be related with the changing spin tune across the profile of the beam as it is extracted onto the carbon polarimeter target [25].

3.4 Achievements at COSY storage ring

The development at FZJ of the *time-stamp system* tool described in the previous section made possible to successfully measure physical quantities that play a fundamental role in spin manipulation, and ultimately in a direct EDM measurement of elementary particles.
The experimental procedure carried out in these measurements is described in this section.

3.4.1 Spin coherence time (SCT) measurement

A fundamental quantity for polarized beam manipulation that is monitored and measured at COSY is the *spin coherence time*, that can be defined as the time taken by the in-plane polarization to drop to $e^{-1/2} = 0.606$ of its original magnitude [26]. Following several tuning and optimization of the machine settings a spin coherence time of about 1000s was achieved at COSY, which is a basic requirement for an EDM measurement with the desired accuracy of 10^{-29} $e \cdot cm$. In this section a description of the technique used in the measurement of the SCT, and of the investigation on the possibility to extend it, is presented.
The SCT studies at COSY aimed to investigate the effects of the decoherence sources represented by a finite transverse beam size (emittance) and the second order momentum spread in the beam $(\Delta p/p)^2$ due to synchrotron oscillations.
In order to study each of these two contributions separately, a polarized deuteron beam with a momentum $p = 0{,}97\ GeV/c$ has been manipulated using the electron cooler (to minimize the beam size) and then bunched so that all first order $\Delta p/p$ contributions average to

zero, obtaining a beam with large $(\Delta p/p)^2$ associated with synchrotron oscillations.

A second setup with a beam characterized by a large horizontal emittance was obtained by cooling and bunching the beam simultaneously for 60s (to minimize the beam size), then switching off the cooling system and on the horizontal heating (white noise applied to horizontal electric field plates). In both cases the polarization was then rotated from vertical direction into the beam plane by use of RF solenoid [27].

The horizontal polarization lifetime of the beam was manipulated using three families of sextupoles in the COSY arc sections, namely the MXG, MXL and MXS sextupoles, chosen because of their suitable position in the ring (see figure 3.7). MXG is located where the dispersion function D is the largest, meaning that particles have large $\Delta p/p$ and travel along different paths with respect to the reference orbit. MXL and MXS are placed in the sections with the largest beta functions β_x and β_y, that is where vertical and horizontal beam sizes are the largest. Figure (3.7) shows where the sextupole magnets are placed inside COSY ring.

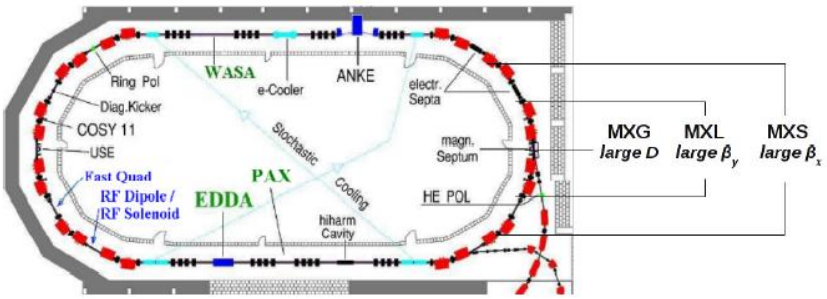

Figure 3.7 - Structure of the COSY ring where the position of the sextupole magnets is indicated on the right arc. The same sextupole arrangement is valid for the left arc.

As a result of several experimental cycles carried out from 2012 to 2014 with different sextupoles fields intensities combinations applied on polarized deuteron beams with large $(\Delta p/p)^2$ and large

horizontal beam size, it was possible to obtain a map of the horizontal polarization lifetime in function of the sextupoles parameters.

In figure 3.8 first results obtained with a fixed value of MXL intensity at -1,45% (with this MXL value zero chromaticity lines are very close to each other), and for several values of MXG and MXL field intensity are shown.

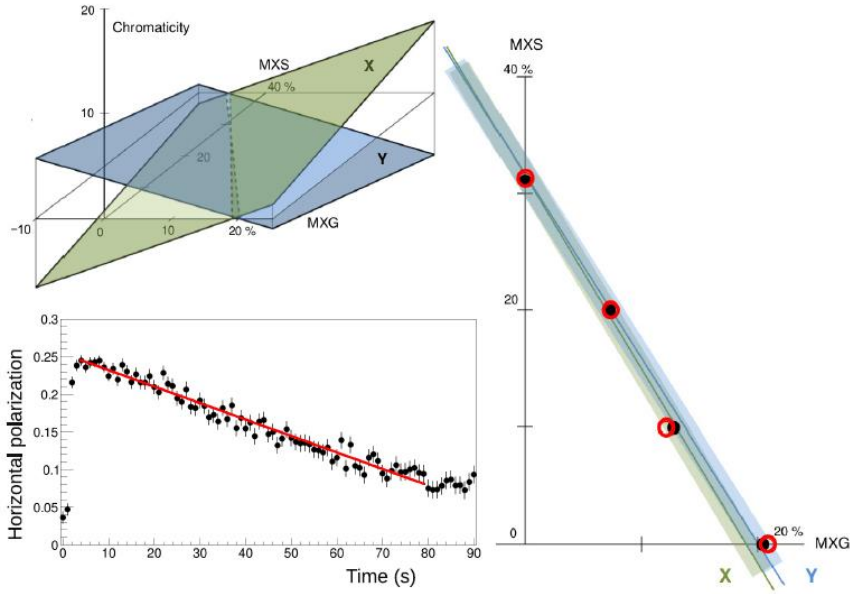

Figure 3.8 - Top-left: X and Y chromaticities measurements as a function of the sextupole fields MXS and MXG with MXL=-1:45%. The scales are in percent of the power supply full range. The dashed lines represent the loci where chromaticities are zero. Bottom-left: an example of horizontal polarization measurement with a linear fit shown with a red line. The slope is proportional to the inverse of SCT in a first approximation. Right side: the preliminary result of SCT measurements for two set of data. The longest horizontal polarization life times (red circles for horizontally wide beam, black dots for large $(\Delta p/p)^2$ lie along the zero chromaticity lines (green is the horizontal and blue is the vertical chromaticity).

The figure shows two chromaticity planes (vertical Y and horizontal X) in the upper left corner with a dashed line representing the zero chromaticity lines.

In the bottom left corner an example of a horizontal polarization measurement is drawn, in the online analysis SCT was defined as the ratio between the zero intercept p_0 and the slope p_1 of the linear fit (red line in figure).

The right side of figure 3.8 shows the location in the sextupole space of the longest SCTs and zero chromaticity lines. On the $\hat{x}$ and $\hat{y}$ axis there are values in percentage of the full power scale for MXS and MXG, and MXL is fixed at −1,45%. The red circles represent the longest SCTs for a horizontally wide beam and the black dots the longest SCTs for large $(\Delta p/p)^2$ contribution.

From these considerations it's clear that the longest polarization lifetimes are found close to the middle-range for zero chromaticity, suggesting that is best to have MXS and MXG field intensities nearly equal, meaning that both horizontal width and longitudinal spread decoherence sources are cancelled where both chromaticities (X and Y) are zero [27].

In the experimental tests performed at COSY from 2014 to present day, it was possible to lengthen the SCT up to nearly 1000s, basic requirement for a direct EDM measurement in a storage ring with the required accuracy, by use of a proper beam preparation and a fine tuning on the combination of sextupole fields intensities.

3.4.2 Spin tune measurement

As explained in the previous sections, the horizontal component of the beam polarization in COSY is characterized by a rapid precession motion about the vertical axis, with frequencies measured typically around 120 kHz.

The beam is made of a big number of particles ($\approx 10^{10}$) with slightly different momenta and thus each individual particle precesses with its own rate, after a sufficient amount of time phase differences between particles' precession rates are piled-up and horizontal polarization decreases as each particle spin points in a different direction.

The so called *spin tune* ν_s can be defined as the ratio between spin precession frequency and beam revolution frequency:

$$\nu_s = \frac{f_{spin}}{f_{beam}} \tag{3.11}$$

In-plane spin rotation and scattering cross section for a polarized beam determine different event rates on the different sides of a polarimetry detector. In an ideal ring, spin tune would be $\nu_s = G\gamma$.
With a spin precession frequency of 120 kHz (see above) and a COSY frequency of about 750 kHz (typical value for the measurements presented in this thesis) a value of around 0,16 of the spin tune is obtained. That corresponds to 6,25 spin precessions in one beam orbit cycle.
Spin tune can be measured with a precision in the order of 10^{-8} over a time interval of 2.6s, a precision of 10^{-10} could be achieved over an interval of ~100s [28].

3.3 COSY, an ideal starting point for...

From what has been presented so far, it's clear that COSY storage ring facility represents an ideal starting point for polarimetry experiments and for the permanent EDM search of charged particles with use of a storage ring. Scientific expertise and experience in the field of spin and beam polarization manipulation make it one of the most suitable facilities in which to design an elementary charged particle EDM search experiment.
In 2011 the international JEDI (Jülich Electric Dipole moment Investigations) collaboration was created at FZJ, involving institutes and universities around the world, aiming to carry out a

long term project for the measurement of the permanent electric dipole moments of charged particles by use of the COSY storage ring.
The ideal scenario for the search of a permanent EDM of an elementary charged particle, like proton, would be a pure electrostatic dedicated storage ring, but with the measurement procedure proposed by JEDI collaboration members it will be possible to perform a proof-of-principle experiment at COSY, a pure magnetic storage ring, by use of a polarized deuteron beam. This experiment could lead to measure the upper boundary of the deuteron permanent EDM.
The main idea is to use a polarized deuteron beam and manipulate its polarization with the help of the RF Wien Filter (see section 2.1.5) in such a way to have an EDM-induced vertical polarization build-up in the beam that can eventually be measured via a polarimeter.
The high performing polarimeter which is going to be used for this measurement is a best performing, new concept of polarimeter based on LYSO scintillator crystal with a read-out system based only on Silicon Photomultipliers (SiPMs) matrices that is being developed at FZJ. The testing and experimental sessions that were carried out in order to develop such a device are the main topic of this thesis and will be illustrated in detail in the next chapter.

CHAPTER 4 - LYSO Polarimeter Development

As briefly described in the end of the previous chapter, a LYSO-based polarimeter is being developed by JEDI collaboration at Forschungszentrum Jülich, to be used for EDM proof-of-principle measurement at COSY storage ring.
In this chapter a detailed description of the experimental activity supporting the LYSO Polarimeter development is given.
The chapter starts with a presentation of LYSO scintillator characteristics that is followed by a description of the polarimeter itself.

4.1 General description and characteristics

LYSO (Lutetium Yttrium Ortosilicate) is a Cerium doped Lutetium based scintillation crystal that offers several benefits compared to many common scintillation materials, e.g. compared to NaI(Tl) it has a high density (7.1 vs. 3.67 g/cm^3), very fast, single exponential decay time (~40 vs. 250 ns), comparable light yield and, very useful, is non-hygroscopic. With a peak wavelength of 420 nm, the output is well matched to the sensitivity curve of photomultiplier tubes (PMTs) as well as silicon photomultipliers (SiPMs).
High density and fast decay time make LYSO a good scintillator for calorimetry and any other kind of application where high stopping power, high throughput and excellent timing are critical.

In table (4.1) general LYSO characteristics are summarized, Figure (4.1) shows LYSO's behavior in terms of response and inner activity, while figure (4.2) shows its emission in a.u.

PROPERTY	VALUE
Density [g/cm^3]	7.1
Attenuation length for 511 KeV (cm)	1.2
Decay time (ns)	36
Energy resolution @ 662 KeV	8.0
Light output, photons per KeV	33
Average temperature coefficient 25 to 50 °C (%/°C)	-0.28

Table 4.1 - Main LYSO properties as given by manufacturer (courtesy of Saint-Gobain Inc.)

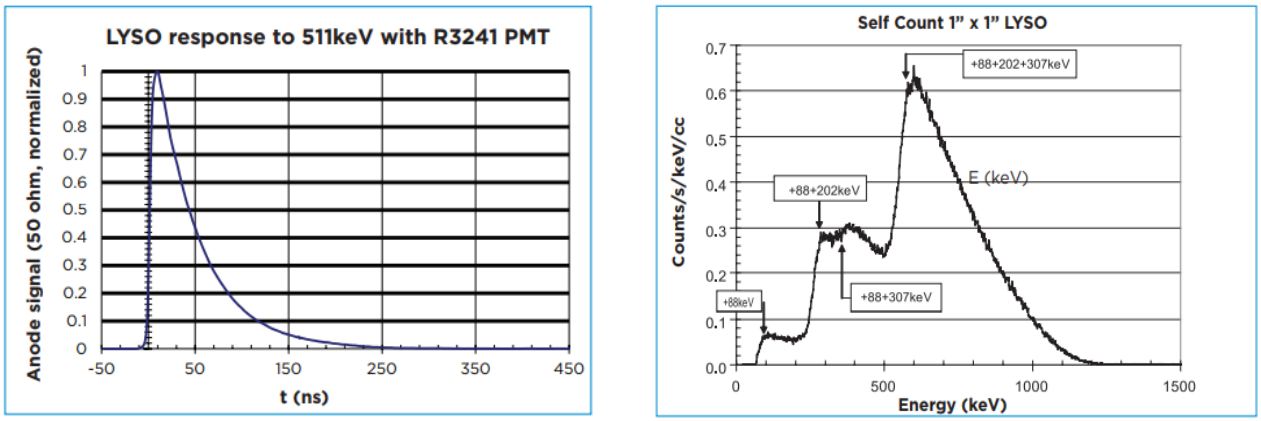

Figure 4.1 – LEFT: LYSO response to 511 KeV – RIGHT: LYSO contains a naturally occurred radioactive isotope, ^{176}Lu, a beta emitter. The decay results in a 3 gamma ray cascade of 307,202 and 88 KeV. Total rate for this activity is 39 cps/g.

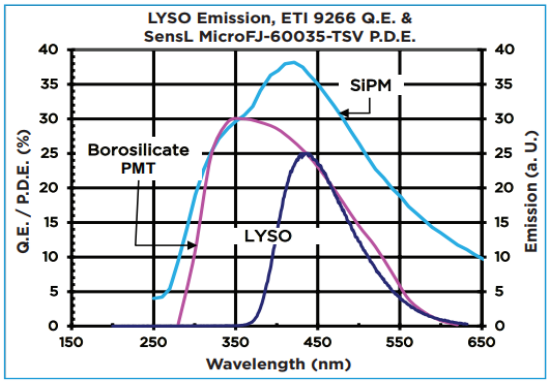

Figure 4.2 - LYSO Emission, ETI 9266 Q.E. & SensL MicroFJ-60035-TSV P.D.E. (Q.E. data courtesy of Electron Tubes, Inc.)

Thanks to its particularly suitable characteristics, LYSO scintillator crystal has been chosen to constitute the sensitive volume of the JEDI polarimetry detector.

The aim of such a device is to measure the polarization of the stored deuteron beam by detection of the asymmetry in elastically scattered deuterons off different targets.

A sketch model of the detector is shown in picture (4.3).

On the left side of figure (4.3) the ingoing direction of the beam is shown. The beam enters the detector from the Target Chamber, the particles scattered off the target continue their flight along the Flight Chamber, onto which *degraders* are hinged, and hit any of the 52 LYSO modules constituting the sensitive volume of the detector, depending on the beam scattering direction. The module then registers particle's energy and scattering position with respect to the incoming direction.

The LYSO modules pack is also covered with two layers of plastic scintillators, allowing for particles identification by means of DeltaE/E method.

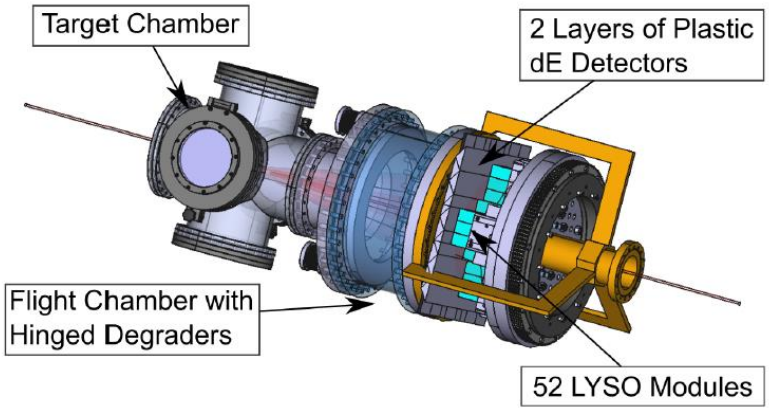

Figure 4.3 – Full LYSO Polarimeter view

4.2 Description of a single LYSO module

The sensitive volume of the detector is made up by a number of LYSO based modules, covering a certain solid angle. Building a modular detector is particularly convenient for more than one reason, first of all it allows for a quick and easy rearrangement of the modules themselves, thus, of the very detector sensitive volume, in case of a change of geometrical characteristics of the experiment; it is also quite easy to assemble and disassemble, therefore making it simple to substitute a single module if it is damaged or malfunctioning.
A concept view of a single LYSO module equipped with SiPMs readout system is shown in picture (4.4).

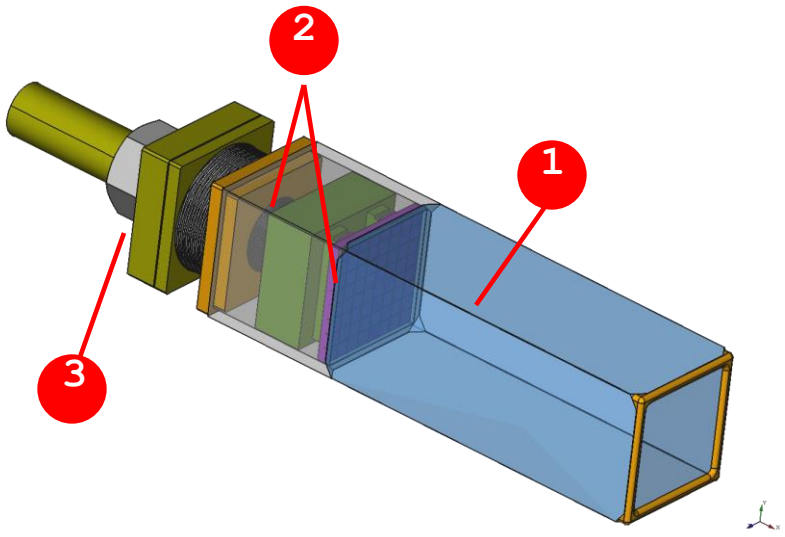

Figure 4.4 - Concept view of a single LYSO-based module. It is possible to observe: 1) LYSO scintillation crystal – 2) SiPM matrix and readout electronics – 3) Mechanics.

With reference to figure (4.4):

1) – LYSO Scintillation crystal

2) – SiPM matrix and readout electronics

3) - Mechanics

4.3 First step: Comparing PMTs and SiPMs in LYSO readout

The first step towards the development of the LYSO polarimetry detector took place at BIG KARL experimental area (see figure 3.1) of the COSY facility at Forschungszentrum Jülich during several COSY test beam times between December 2015 and March 2016.
It was primarily aimed to investigate the possibility to use SiPMs instead of usual PMTs to detect photons out of LYSO scintillation crystal, this opportunity is particularly convenient since SiPMs do not require a supply voltage as high as PMTs to work (~30V vs. ~1200 V), unlike PMTs they are also almost completely insensible to magnetic fields, and much less expensive. They also allow for a more compact layout of the individual LYSO modules.

4.3.1 Setup description

In order to carry out this task, an ensamble of 4 LYSO modules was built, three of which read by usual PMTs and one read by four 2x2 pixels SiPM matrices, and an extracted deuteron beam consisting of a number of particles in the order of 10^9 at various energies (from 100 to 270 MeV) was shot directly into the modules.
On each side of the LYSO modules pack a 100x60 mm rectangular plastic scintillator, half a centimeter thick and coupled with 4 single SiPM pixels (one on each rounded corner), was fixed in order to act as a

veto module and detect all the particles leaking from the body of the modules, therefore depositing only part of their kinetic energy in the crystals.

The entire setup was fixed on a movable positioning table, allowing for position adjustment.

Figure (4.5) shows a schematic of the experimental setup used during this testing session, figure (4.6) shows the setup itself.

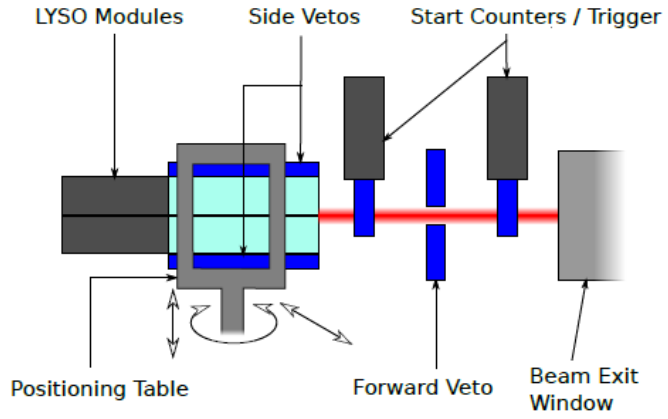

Figure 4.5 - Schematic of the experimental setup

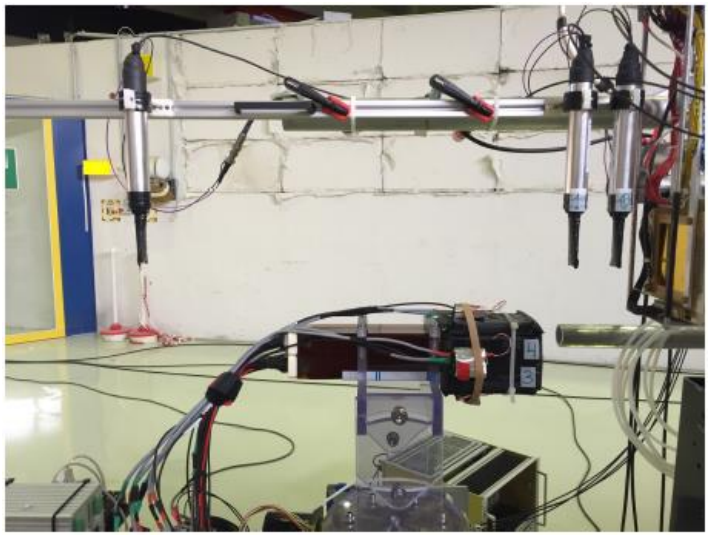

Figure 4.6 - Picture of LYSO I experimental setup during working conditions

LYSO MODULES: In the first experimental test, 30x30 mm surface section and 100mm long *Saint-Gobain* LYSO crystals were used for three

of the four modules built, two 30x30 mm section and 50mm long *Epic Crystals* LYSOs was used for the other one. This allowed to compare between crystals of different manufacturers; all modules were numbered from 1 to 4:

Module 1) *Saint-Gobain* 30x30mm surface, 100mm long LYSO crystal
Coupled with *Hamamatsu* PMT via light guide.

Module 2) *Saint-Gobain* 30x30mm surface, 100mm long LYSO crystal
Coupled with *Hamamatsu* PMT via light guide.

Module 3) *Saint-Gobain* 30x30mm surface, 100mm long LYSO crystal
Coupled with four *SensL ArrayC-60035-4P-BGA* 2x2 pixels SiPM matrices, for a total of 16 pixels, each with a 6x6 mm surface section.

Module 4) 2x *Epic Crystals* 30x30mm surface, 50mm long LYSOs
Coupled with *Hamamatsu* PMT via light guide.

A detailed view of a single module, both with a PMT and with SiPMs, is shown in picture (4.7) and (4.8).

Figure 4.7 - Detailed view of a single LYSO module, coupled with an Hamamatsu PMT, as used in LYSO I experiment

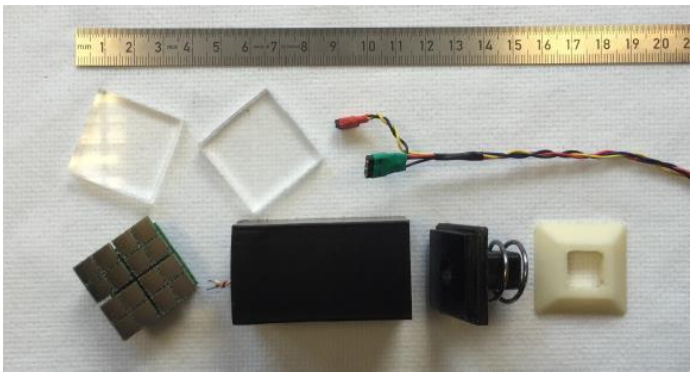

Figure 4.8 - Detailed view of a SiPM-coupled LYSO module (LYSO crystal not shown in the picture)

SIDE VETO MODULES: Each side veto module consists of a single plastic scintillator with a 100x60 mm rectangular face and 5 mm thickness and with chamfered corners. The scintillator is first wrapped in white Teflon tape in order to increase photon reflection index towards the inside of the crystal, and further coated with a Tedlar black tape in order to keep the whole module as light-tight as possible, the four corners are left uncovered in order to attach one *SensL microFC-60035-SMT* SiPM pixel on each corner.

A 3D printed plastic housing was built for each of the four modules. Picture (4.9) shows a single side veto module already assembled, and a close view of one single SiPM pixel is shown in picture (4.10).

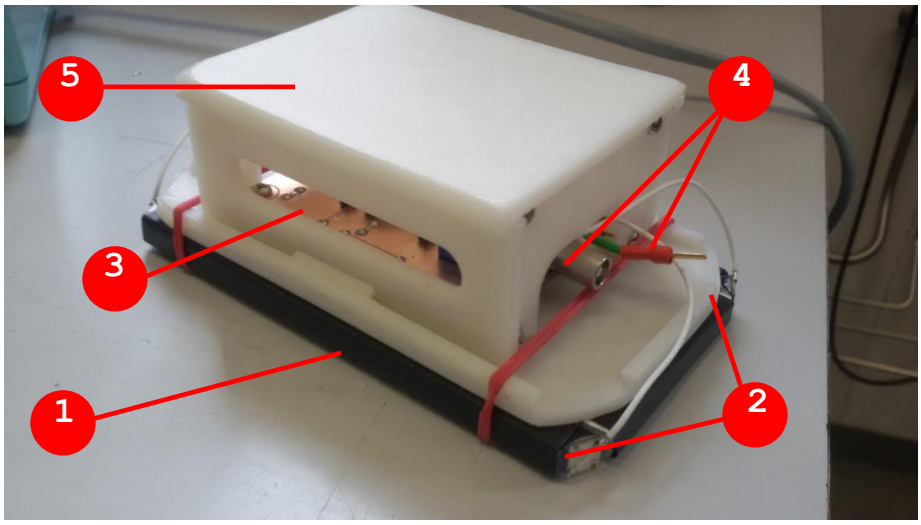

Figure 4.9 - View of a single side veto module already assembled.

With reference to picture (4.9) it is shown:

1) **Plastic scintillator** wrapped in Teflon tape and Tedlar film.

2) **SiPM pixels** mounted on the corners of the scintillator.

3) **Read-out circuit** board.

4) LEMO signal cable and read-out circuit power supply cable **connectors.**

5) 3D printed **plastic housing.**

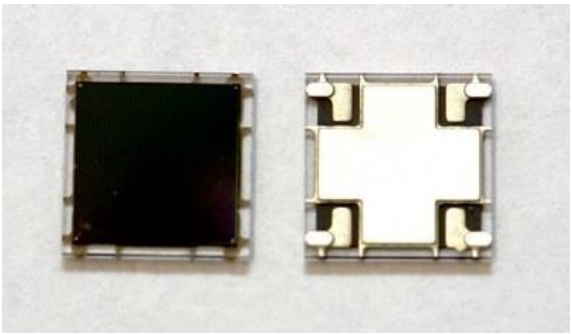

Figure 4.10 - View of a single *SensL microFC-60035-SMT* SiPM pixel used to pick up photons out of side veto plastic scintillator

4.3.2 Read-out electronics design and development

LYSO MODULES: In order to read out the signal from the PMT modules, a custom high voltage board was built by *SmartLab* group at Forschungszentrum Jülich. The module coupled with SiPM matrices was read by a standard *SensL* SiPM read-out board.

SIDE VETO MODULES: The read-out circuit board for side veto modules was designed and developed by *SpinLab* group at University of Ferrara, starting from technical specifics of a *SensL microFC-60035-SMT* single pixel summarized in table (4.2) as given by the manufacturer.
Pictures (4.11) shows the schematics.

PARAMETER	Min.	Typical	Max.	Units
Breakdown Voltage (V_{br})	24.2		24.7	**V**
Recommended Overvoltage (V - V_{br})	1		5	**V**
Spectral Range	300		800	**nm**
Peak Wavelength		420		**nm**
Photon Detection Efficiency		47		**%**
Gain (anode to cathode readout)		$6x10^6$		
Dark Count Rate		30	96	**kHz/mm^2**
Temperature Dependance of V_{br}		21.5		**mV/°C**

Table 4.2 - Technical specifics of *SensL microFC-60035-SMT* SiPM pixel coupled to side vetos plastic scintillator.

The aim was to design a circuit capable of amplifying the output signal of a silicon photomultiplier, in the order of a few millivolts, to generate an output signal of ~1000 mV.
The task was accomplished by making use of a feedback amplification circuit based on *Analog Devices AD8000* OpAmp, as in the schematics shown in picture (4.11).

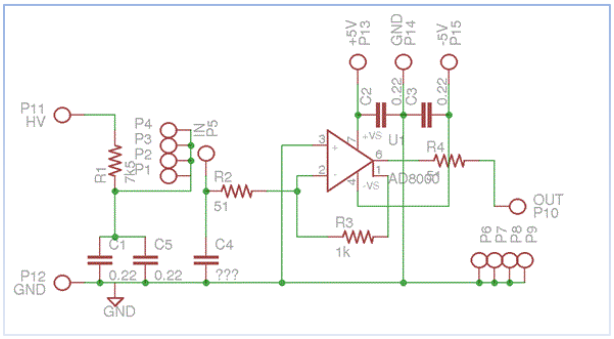

Figure 4.11 - Schematics of readout circuit for one SiPM pixel.

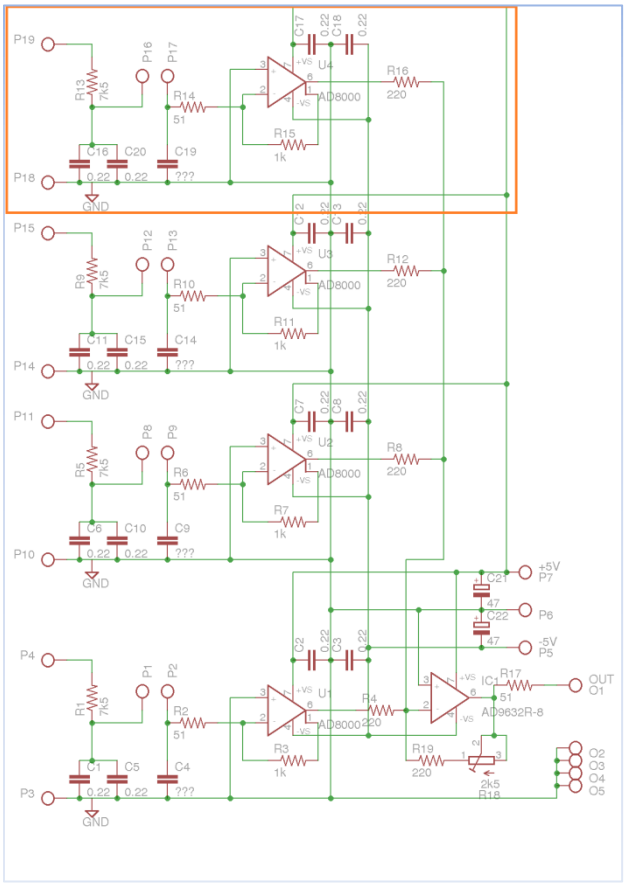

Figure 4.12 - Schematics of the complete SiPM readout circuit for side veto modules. Into the orange box a single SiPM amplification circuit (same as in pic 4.12).

Taking into consideration that the readout board was supposed to read four pixels in each module, in order to obtain only one balanced signal per module, the output signal of each amplification circuit is

led into a fifth feedback amplification loop (built on *Analog Devices AD9632* OpAmp) with an adjustable gain acting as a summing buffer providing a signal averaged over the four SiPMs signals.
Schematics of the complete board are shown in picture (4.12) (in the same picture a single SiPM amplification circuit is highlighted into the orange box).
The board was designed via CAD drawing tool and CAD design was used to print the PCB by use of a PCB printing machine (CNC) at the electronic workshop of University of Ferrara (see picture 4.13 and 4.14).
The ultimate version of the PCBs is shown in picture (4.14).

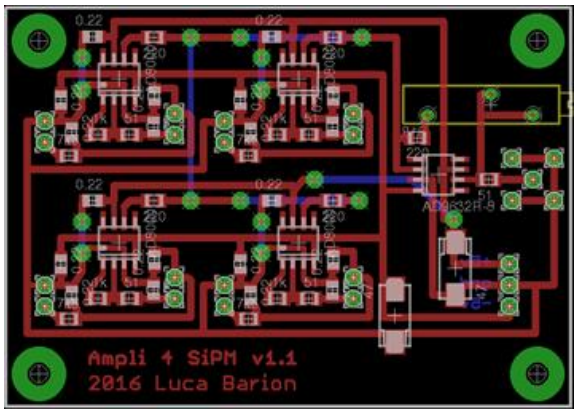

Figure 4.13 - CAD design of SiPMs readout PCB for side veto modules.

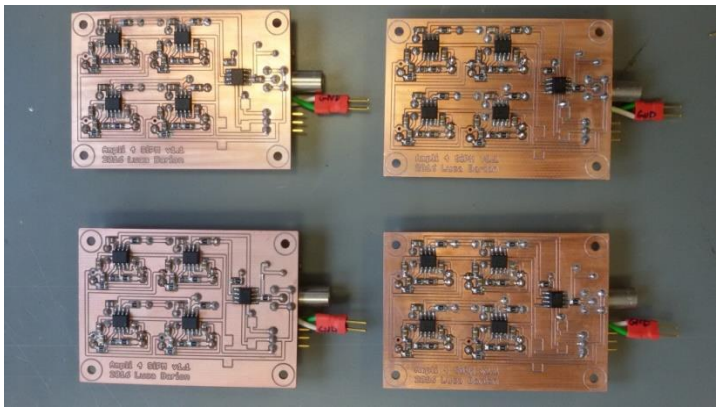

Figure 4.14 - Ultimate version of the readout circuits for side veto modules.

Each circuit was first tested with cosmics and with a 1 kHz frequency, 100 ns width pulsed LED source. Results for one circuit shown in figure (4.15).

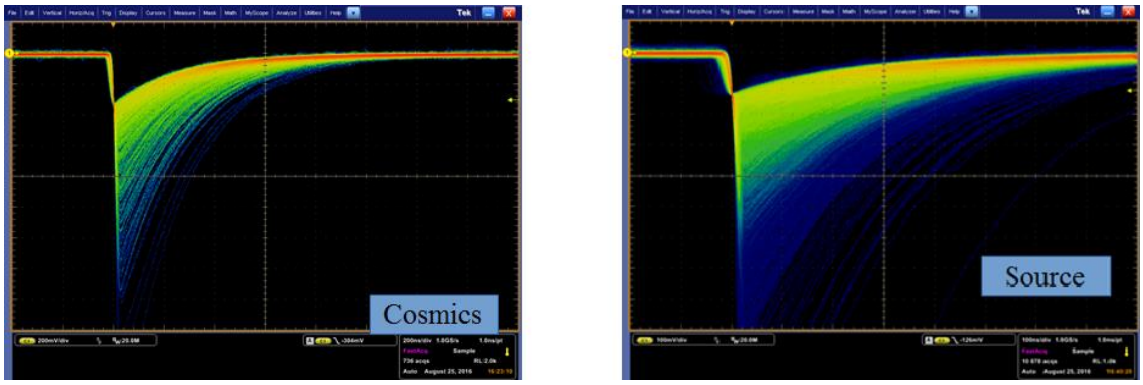

Figure 4.15 - Side veto modules readout circuit test results with cosmics (Left) and with a white LED source pulsed at 1 kHz, 100 ns pulse width (Right).

After a laboratory testing session the whole setup was assembled in the BIG KARL experimental area at FZJ during which an extracted deuteron beam was shot directly into LYSO modules pack at four different energies: 100 MeV, 200 MeV, 230 MeV and 270 MeV.

4.3.3 Experimental results

The experimental session led to important results that allowed for an evaluation of parameters crucial for further development.

DEUTERON RECONSTRUCTION EFFICIENCY: From the acquired spectra, the deuteron reconstruction efficiency (DRE) was estimated via the formula (4.1).

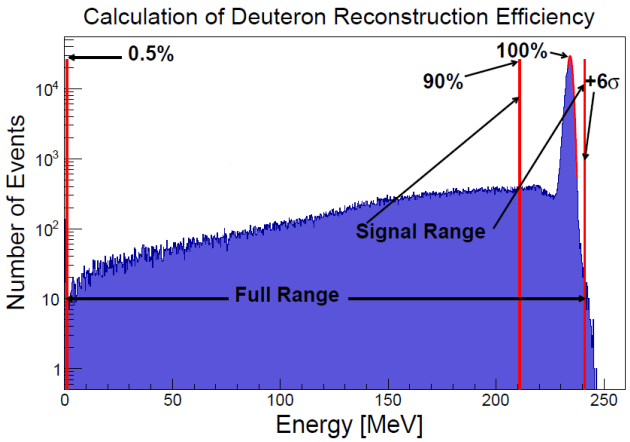

Figure 4.16 - Single LYSO module spectrum at 230 MeV, with y-axis in log scale. All the properties used in deuteron reconstruction efficiency calculation are shown.

$$\epsilon = \frac{\int Signal\ Range}{\int Full\ Range} \tag{4.1}$$

The same calculation was then repeated for all modules and for all of the four energies investigated so that a general behavior of DRE in function of energy could be assessed for each module by interpolating single values with the exponential function reported in formula (4.2). Results are shown in picture (4.17).

$$\epsilon = A_\epsilon e^{\lambda_\epsilon E} \tag{4.2}$$

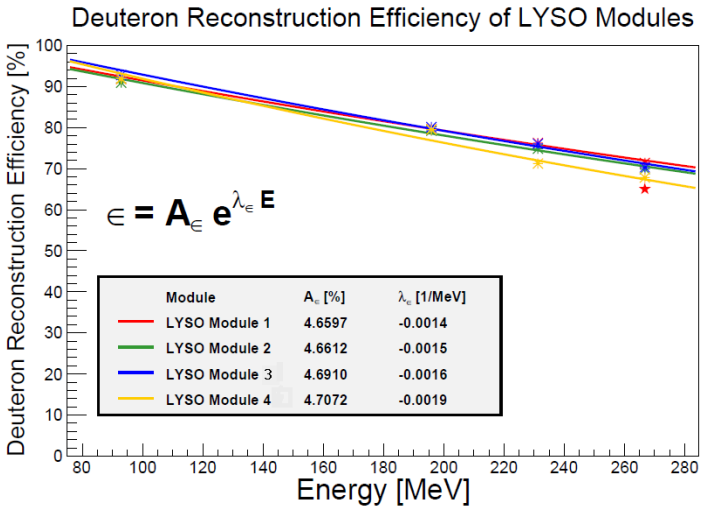

Figure 4.17 - Deuteron reconstruction efficiency in function of energy for all four LYSO modules.

As shown in the plot in figure (4.17), DRE varies between 90% at 100 MeV and 70% at 270 MeV, which is well under way.

ENERGY RESOLUTION OF LYSO MODULES: The energy resolution for each module was evaluated starting from the spectrum of the single module via the ratio:

$$R = \frac{FWHM}{\langle E \rangle}$$

The single spectrum along with resolution properties is shown in picture (4.18).

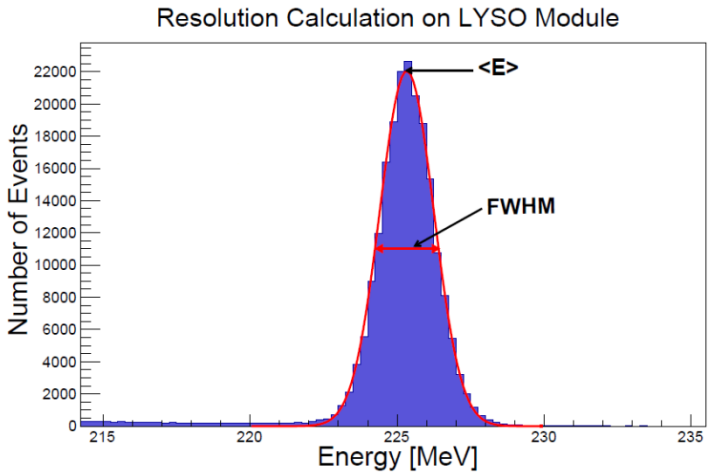

Figure 4.18 - Spectrum of a single LYSO module at 230 MeV with parameters used in resolution calculation.

As for DRE, the same calculation was repeated for all the modules and all energies to provide an evaluation of the resolution behavior in function of energy by interpolating the values via the classic calorimetry convolution formula:

$$R = \frac{a}{E} \oplus \frac{b}{\sqrt{E}} \oplus C \tag{4.3}$$

Where E is the energy and a, b and C are constants.
The resolution plot is shown in picture (4.19).

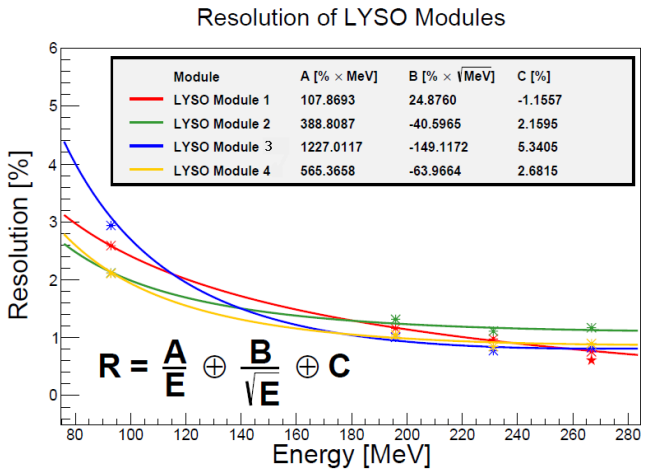

Figure 4.19 - Energy resolution in function of energy for all four LYSO modules.

The results show that a resolution around 1% at 270 MeV was achieved, with the possibility to further improve this result.

COMPARISON BETWEEN PMTs AND SiPMs: Picture (4.20) shows a direct comparison between a single normalized spectrum obtained with a usual PMT-coupled LYSO crystal (module 1) and the one obtained with the SiPM-coupled crystal (module 3) is shown.

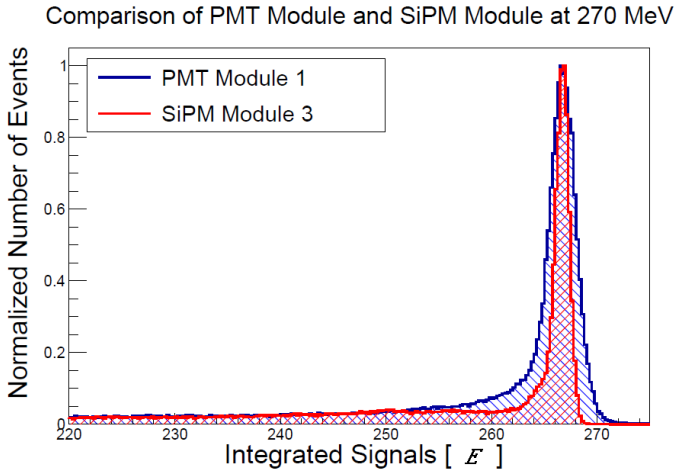

Figure 4.20 - Comparison of PMT module and SiPM module at 270 MeV.

It's easy to understand from the picture above, that in the SiPM module the resolution is better than the PMT module, This evidence lead to the choice of SiPMs over PMTs to read from LYSO and develop a total SiPM-based LYSO polarimeter.

DEUTERON STOPPING POWER OF LYSO: From the measurement of the deuteron stopping power of LYSO, plotted in picture (4.21), another important conclusion was drawn: that the length of each LYSO crystal does not need to be 10 cm: since the peak in the stopping power was observed at ~6 cm with a tail that rapidly falls below ~1% after 7.5 cm it's been chosen a new length for the crystals of 8 cm.

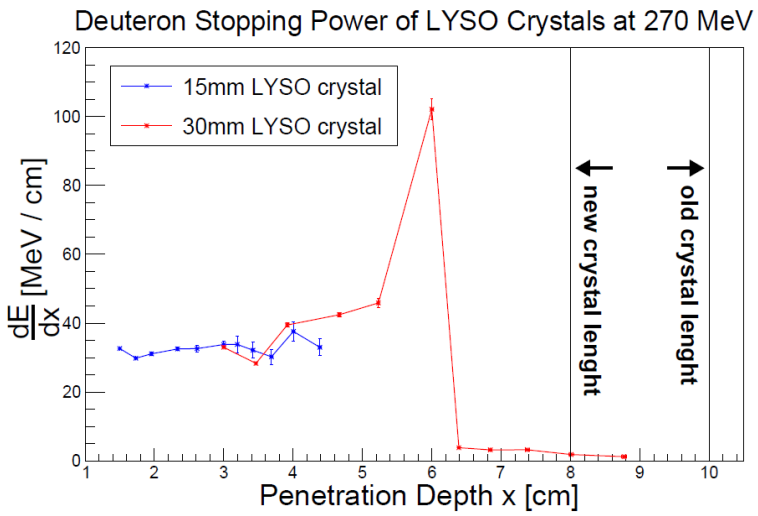

Figure 4.21 - Deuteron Stopping power of LYSO at 270 MeV.

4.4 Step 2: detection of a scattering asymmetry

The second experimental test was performed at FZJ between December 2016, March and November 2017, its main goal was investigating the possibility to measure the beam polarization via scattering asymmetry off a target with a given analyzing power, by use of SiPM-read LYSO-based modules.

Carbon is the main target material chosen, because of its well-known AP, but also targets of different materials have been used to search for other elements with suitable analyzing power.

4.4.1 Setup description

A new experimental setup was built for this purpose, as it is shown in picture (4.22).

The setup is made of a main portal-shaped frame onto which an online controlled stepper motor-driven plastic wheel is fixed after an iron

collimator, the aperture of which can be controlled by an online controlled stepper motor.
The plastic wheel has several slots to host up to six different targets and is positioned in such a way to hold only one chosen target in line with the direction of the outgoing extracted beam, This solution allows to change remotely the target without interrupting the beam extraction.

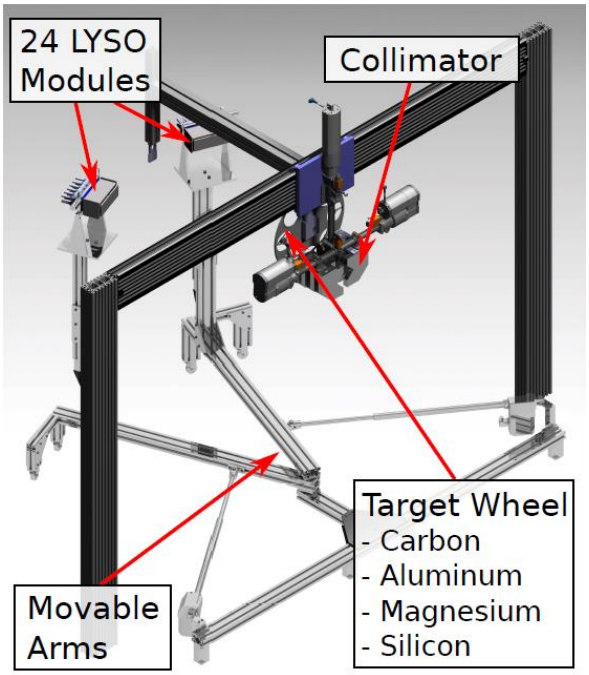

Figure 4.22 - Concept view of experimental setup used in LYSO II experiment.

Two movable mechanical arms, remotely driven via a stepper motor, are mounted on the main frame, on each arm a 3x4 modules pack, for a total of 12 LYSO modules per pack, is held in plane with the beam.
On each array a 90x120 mm plastic scintillator of 5 mm thickness is fixed. The scintillator is read by four *SensL microFC-60035-SMT* SiPM pixels, allowing for a *dE vs. E* plot of each side LYSO pack.
By moving the two arms, the LYSO packs can cover an azimuthal ϑ angle between ~4 degrees and ~85 degrees.
The distance between the target and LYSO's trajectory is approximately 1 meter.

A simple scheme of the experimental setup is shown in picture (4.23).

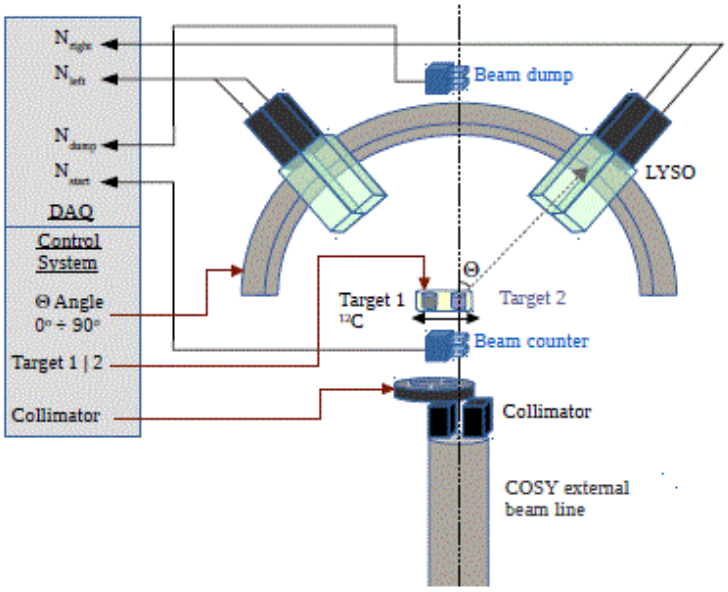

Figure 4.23 - Simple schematic of the experimental setup used in LYSO II experiment.

In order to register the total number of particles impinging the target, a *Beam Counter* made of a thin plastic scintillator read by a PMT was placed between the collimator and the target wheel, and use such an information to calculate Luminosity, fundamental in Cross Sections calculation.

LYSO MODULES: For this experimental session a new concept of LYSO module was developed, characterized by a new size for LYSO crystal, 8 cm, and a new SiPM-based readout system.
Picture (4.24) shows a detailed view of a new LYSO module.

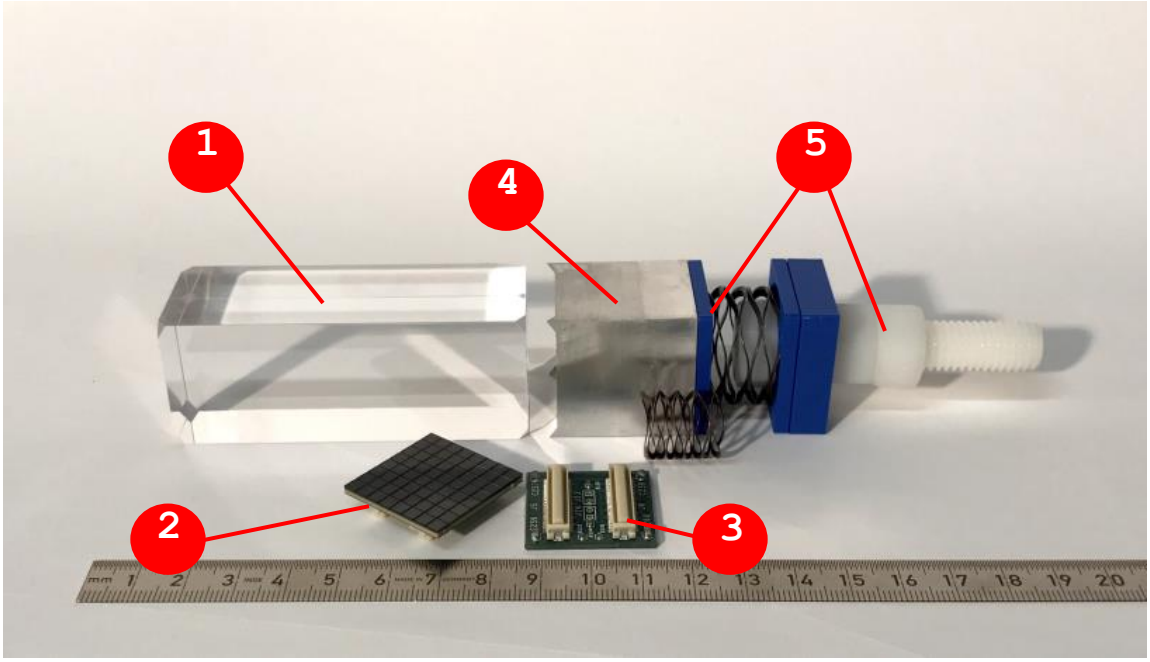

Figure 4.24 - A detailed exploded view of a single LYSO module

With reference to picture above it is possible to describe:

1) **LYSO crystal** – an 8 cm long LYSO scintillation crystal, with a surface section of 30x30 mm and chamfered edges.

2) **Silicon Photomultiplier (SiPMs) matrix** – an 8x8 SensL SiPMs matrix, 28x28 mm surface, for a total of 64 photomultiplier pixels per module, coupled to scintillation crystal through an optical coupling silica film.

3) **Readout circuit** – SiPMs matrix passive readout circuit PCB, designed and built at University of Ferrara (for a detailed description of the designing and building processes of the PCB, please check the section below).

4) **Aluminum casing** – A 3 cm long aluminum casing, 3x3 cm surface section, with shaped edges is used to hold the crystal, the

SiPMs matrix and the readout circuit in the centered position; a strip of Kapton tape is placed on the internal edge of the casing in order to prevent the metal case from electrically interacting both with the PCB and with the matrix.

5) **Spring holder and mechanics** – a tin spring is fixed on the back face of the aluminum casing via a 3D printed plastic holder (blue-colored in the picture), and a mechanical system of 3D printed plastic screw and nut ensure the SiPMs signal LEMO cable and the power supply cable to the body of the module.

Both the crystal and the aluminum casing, with SiPMs matrix and PCB inside, are then covered with a white Teflon tape in order to increase photon reflection index towards the inside of the crystal, and further coated with a Tedlar black tape in order to keep the whole module as light-tight as possible.

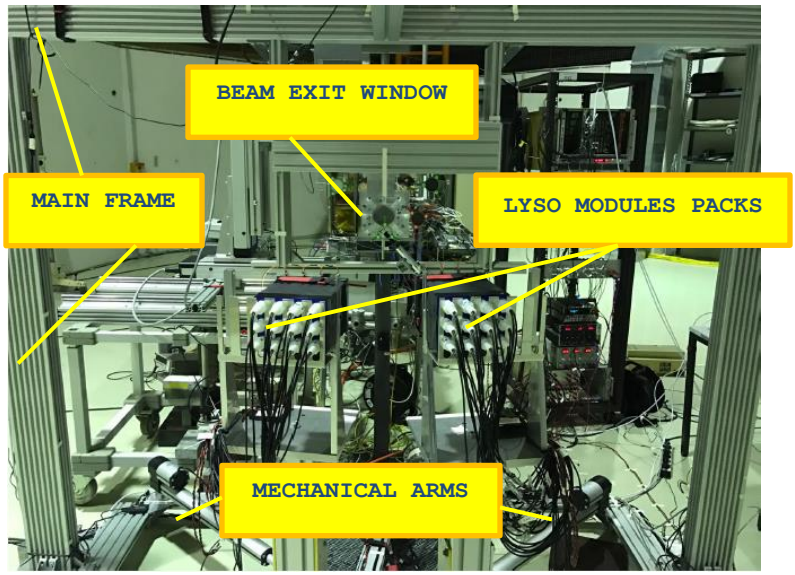

Figure 4.25 - Experimental setup assembled in BIG KARL area (target wheel and collimator NOT mounted).

dEvs.E MODULES: Both LYSO packs have a *dEvs.E* module mounted on the front face, each of these modules is made of a 90x120 mm plastic

scintillator of 5 mm thickness. The scintillator is read by four *SensL microFC-60035-SMT* SiPM pixels, allowing for a *dE vs. E* plot.

4.4.2 Read-out electronics design and development

LYSO MODULES: In order to detect the photons generated by the LYSO crystals an 8x8 SiPM pixels *SensL ArrayJ-30035-64P-PCB* has been chosen, on the base of its technical specifics a custom read-out circuit has been developed by *SpinLab* group at University of Ferrara. Two different passive-parallel solutions (no pre-amplification stage) have been chosen amongst the *ArrayJ* datasheet suggestions: as shown in picture (4.26).

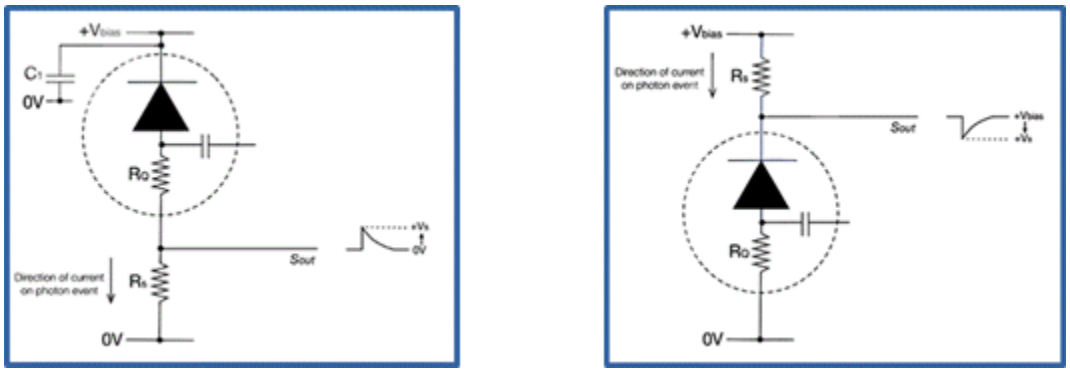

Figure 4.26 - LEFT: positive output schematics - RIGHT: negative output schematics. Both as suggested in the *SensL Array-J* datasheet, both read from the standard output.

The main difference consists in the signal polarity (plus or minus voltage).

The PCB was then designed (picture 4.27) and built for both schematics in order to test them and compare the results, the ultimate version of the PCBs, for both scheme A and B is shown in picture (4.28).

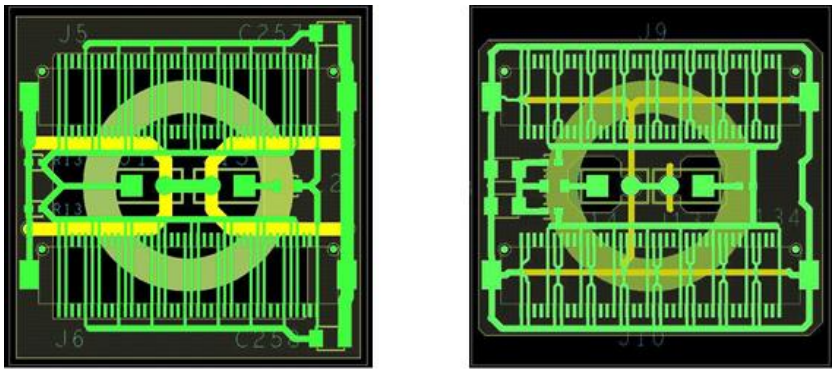

Figure 4.27 - LEFT: PCB design for Scheme A - RIGHT: PCB design for Scheme B

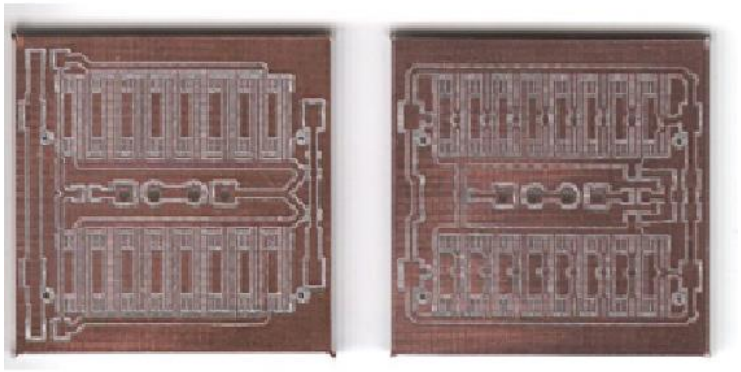

Figure 4.28 - LEFT: PCB positive output - RIGHT: PCB negative output

Eventually the final choice was to use scheme A, with a positive output, since its polarity matched that of the data acquisition hardware.

A total of 24 new modules has been built, tested and then assembled in the experimental setup placed in the BIG KARL experimental area at FZJ, and a 200, 270 and 300 MeV extracted deuteron beam has been shot into the targets.

4.4.3 Experimental Results and data analysis

DATA ACQUISITION SYSTEM* and *SINGLE MODULE SPECTRA: An online data analysis tool was developed by *SmartLab* group at FZJ, allowing for a real time visualization of each LYSO module spectrum, an example is given in figure (4.29)

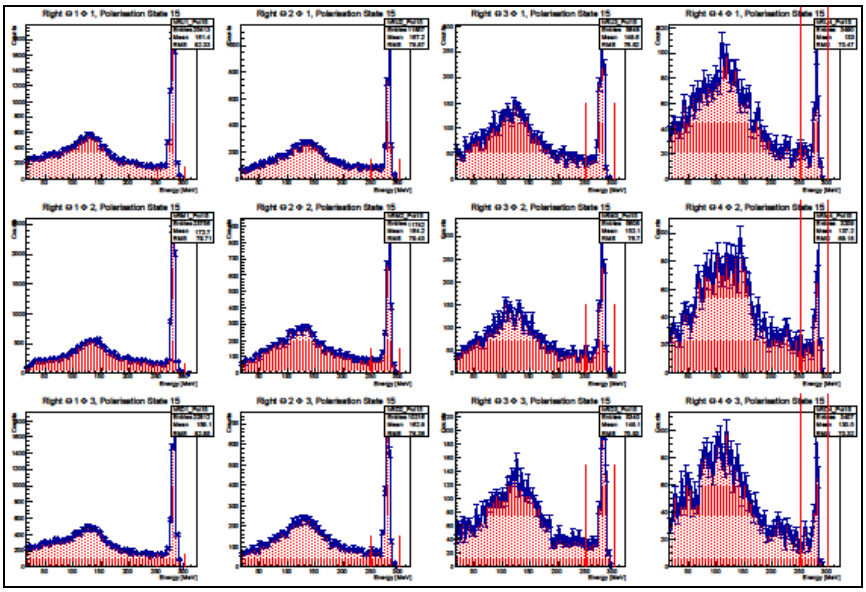

Figure 4.29 - Example of elastic scattering single spectra (for RIGHT detector arm) visualized via custom-made online analysis tool. From the comparison between the height of the peaks and the background, assumed constant over all modules, it is easy to note how for small angles (left side of the picture) the event rate, and thus the total amount of events, is much higher, as expected.

Unpolarized Cross Sections: In the following section results for Carbon target will be shown and described along with a description of the data analysis procedure, followed by results for the other targets obtained with the same procedure. Starting from the spectra acquired for each module in both arms, it was possible to calculate elastic scattering differential cross section for Carbon and other elements in the Theta range between ~4.5 degrees and ~10.5 degrees.By applying proper cuts and a Gaussian fit to each single spectrum in order to characterize the elastic peak, the total number of events registered by each module was obtained (see figure 4.30).

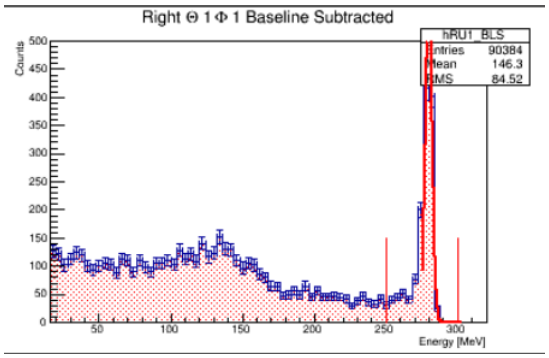

Figure 4.30 - Single elastic scattering spectrum with cuts and Gaussian fit applied.

Since the upper and lower rows of modules lay on a different plane with respect to beam plane, they register a lower count rate for a given theta value.

Hence a small correction is to be applied to the horizontal position of these modules in order to compensate for the lower count rate due to their different polar angle.

From calculations it has been stated that, for upper and lower rows of modules, a 'virtual' shift of ~0.4 degrees towards higher values of theta would result in a count rate that equals that of the *in-plane* modules in the same theta position (see figure 4.31).

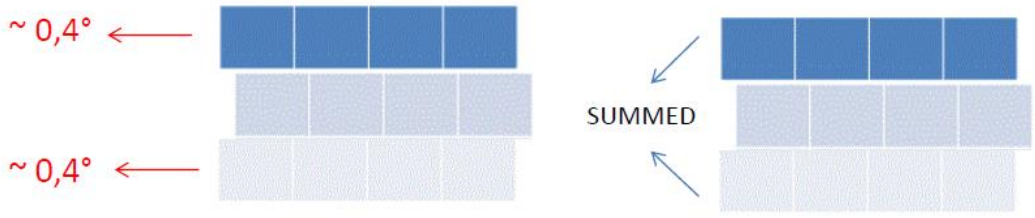

Figure 4.31 - By virtually shifting upper and lower rows by 0.4 degrees it's possible to compare event rates of different planes (left arm in the example figure)

By applying this procedure it is now possible to directly compare the total number of events of modules laying on different planes with respect to beam plane. Summing the events of corresponding modules from upper and lower rows (same theta) and dividing by two a total of eight event rate values *for each arm* in the theta range between 4,5 and 10,5 degrees is obtained.

Assuming a perfect symmetry of the two detector arms and a roughly equal number of right/left scattering events (unpolarized beam) it is possible to sum and divide by two left/right values with same theta in order to improve statistics.
The last information required to evaluate Cross Section is Luminosity. Since the experimental setup has a start counter plastic scintillator placed right before the target, a value of Luminosity for each target is obtained by multiplying the total number of events registered by the start counter (that is the total number of particles impinging the target) by the areal atomic density of the target, that is simply the usual atomic volume density times its thickness.
The differential Cross Section is calculated with the formula (4.4):

$$\frac{d\sigma}{d\Omega} = \frac{N_{peak}}{L \cdot d\Omega} \cdot \eta_{LYSO} \tag{4.4}$$

Where:

- N_{peak} = total number of events in each scattering peak
- L = Luminosity
- $d\Omega$ = Solid angle seen by LYSO crystal face (for small angles the actual size of the whole face is assumed, 0.03x0.03 m^2)
- η_{LYSO} = LYSO detection efficiency factor, evaluated via MonteCarlo-based numerical simulations (value assumed = 1.4).

EVALUATION OF DEUTERON-CARBON UNPOLARIZED DIFFERENTIAL ELASTIC CROSS SECTIONS AT 200 MeV

Figure (4.32) shows single spectra for each crystal in left and right arm:

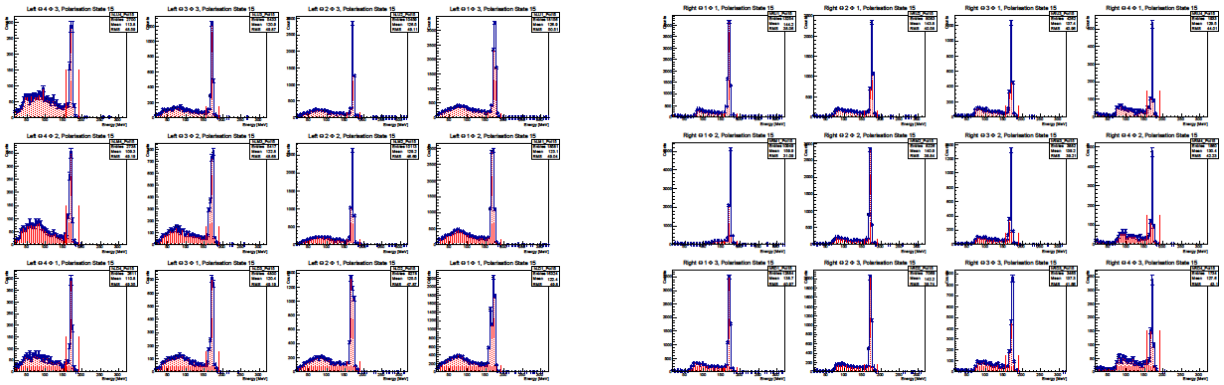

Figure 4.32 - dC Elastic scattering single spectra @ 200 MeV for left arm (LEFT) and right arm (RIGHT)

Figure (4.33) and (4.34) show Cross Section values for each module in both arms, in comparison with Satou's [rif.]:

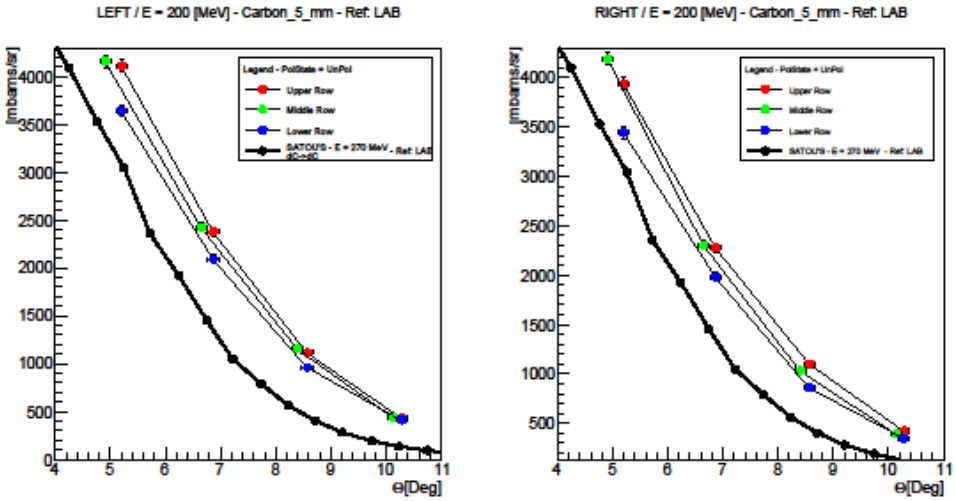

Figure 4.33 - dC elastic scattering differential Cross section @ 200 MeV for each crytal separately. GREEN = in-plane row, RED = Upper row, BLUE = Lower row. Reference frame: Laboratory.

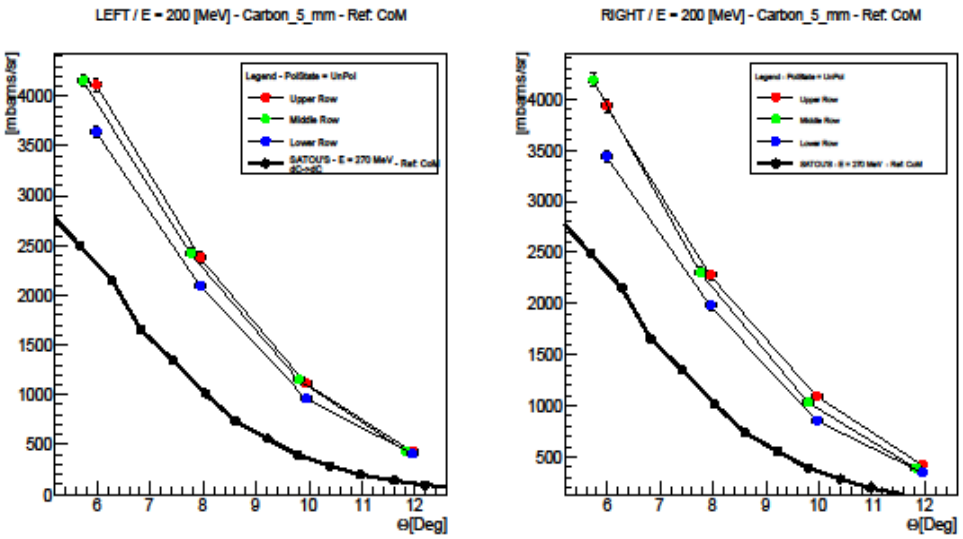

Figure 4.34 - dC elastic scattering differential cross section @ 200 MeV. Reference frame: Center of mass.

Figures (4.35) and (4.36) show the total Cross Section in the theta range between 4.5 and 10.5 degrees (in the Laboratory reference frame), both arms averaged with the procedure described above.
In Laboratory reference frame and in Center of Mass reference frame respectively:

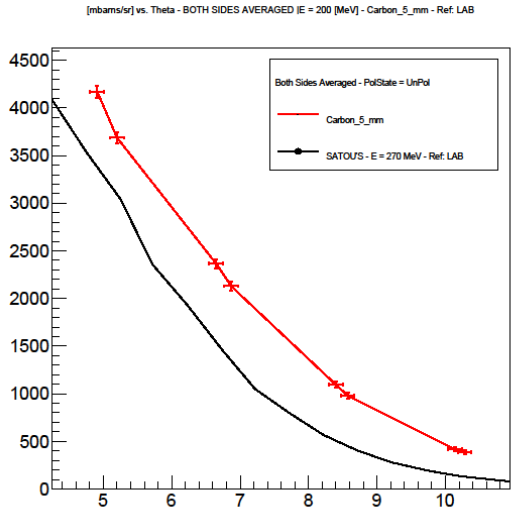

Figure 4.35 – dC differential Cross section @ 200 MeV. Both sides averaged. Reference frame: Laboratory.

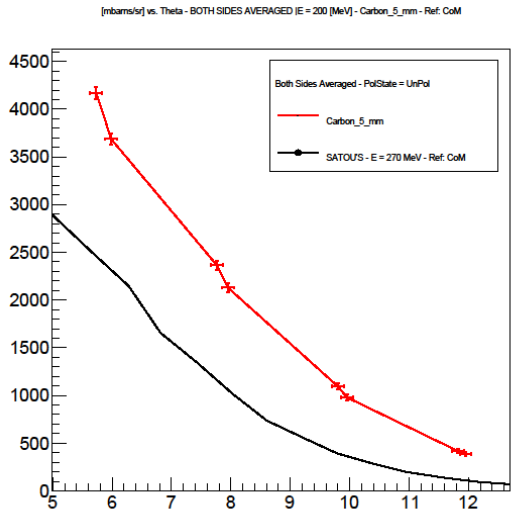

Figure 4.36 - dC differential cross section @ 200 MeV. Both sides averaged. Reference: Center of mass.

EVALUATION OF DEUTERON-CARBON UNPOLARIZED DIFFERENTIAL ELASTIC CROSS SECTION AT 270 MeV

Figures (4.37) and (4.38) show the total Cross Section in the theta range between 4.5 and 10.5 degrees (in the Laboratory reference frame), both arms averaged.

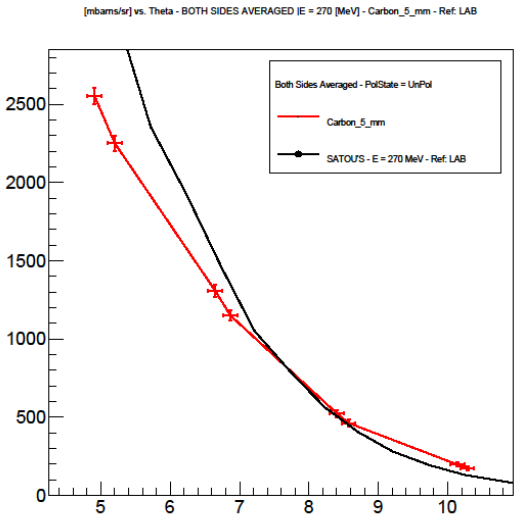

Figure 4.37 - dC differential Cross section @ 270 MeV. Both sides averaged. Reference frame: Laboratory.

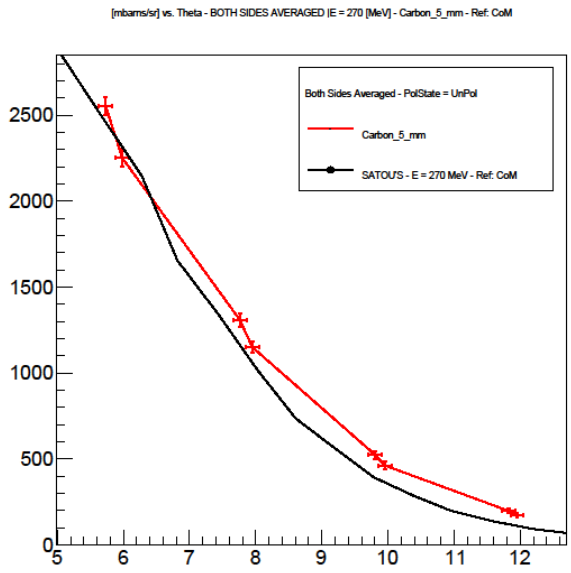

Figure 4.38 - dC differential Cross section @ 270 MeV. Both sides averaged. Reference frame: Center of Mass.

EVALUATION OF DEUTERON-CARBON UNPOLARIZED DIFFERENTIAL ELASTIC CROSS SECTION @ 300 MeV

Figures (4.39) and (4.40) show the total Cross Section, both arms averaged.

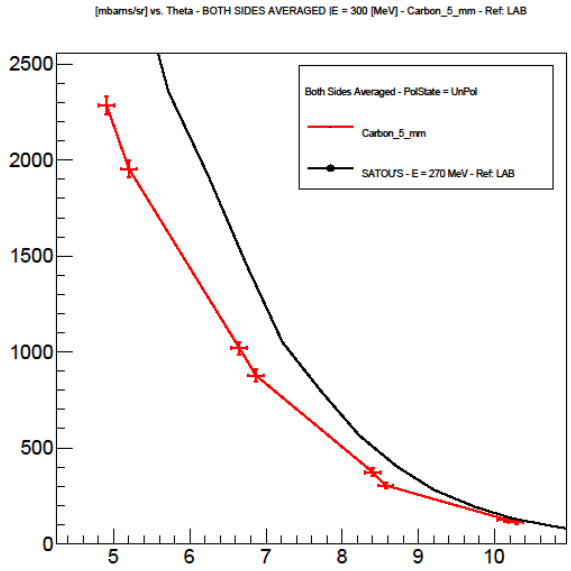

Figure 4.39 - dC differential Cross section @ 300 MeV. Both sides averaged. Reference frame: Laboratory.

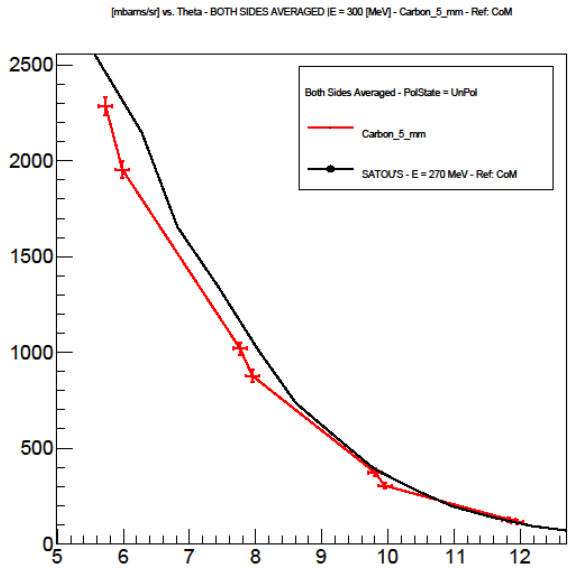

Figure 4.40 - dC differential Cross section @ 300 MeV. Both sides averaged. Reference frame: Center of Mass.

The following figures, (4.41) and (4.42), compare unpolarized differential cross sections of all target elements @ 270 and 300 MeV in the Lab reference frame:

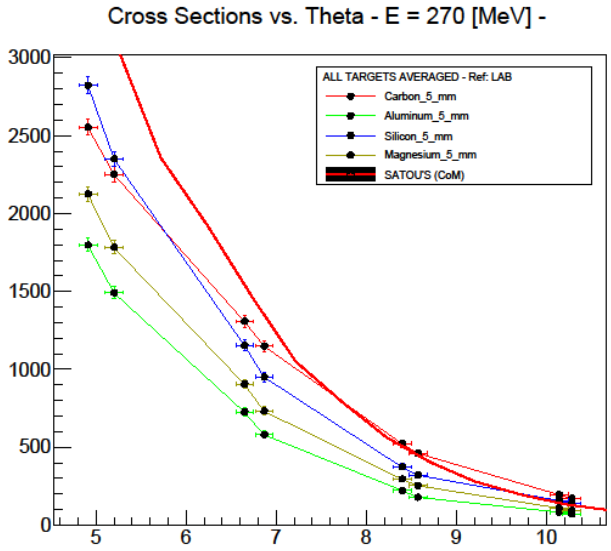

Figure 4.41 – Total unpolarized differential Cross section [mbarns/sr] @ 270 MeV for various elements. Both sides averaged. Reference frame: Laboratory.

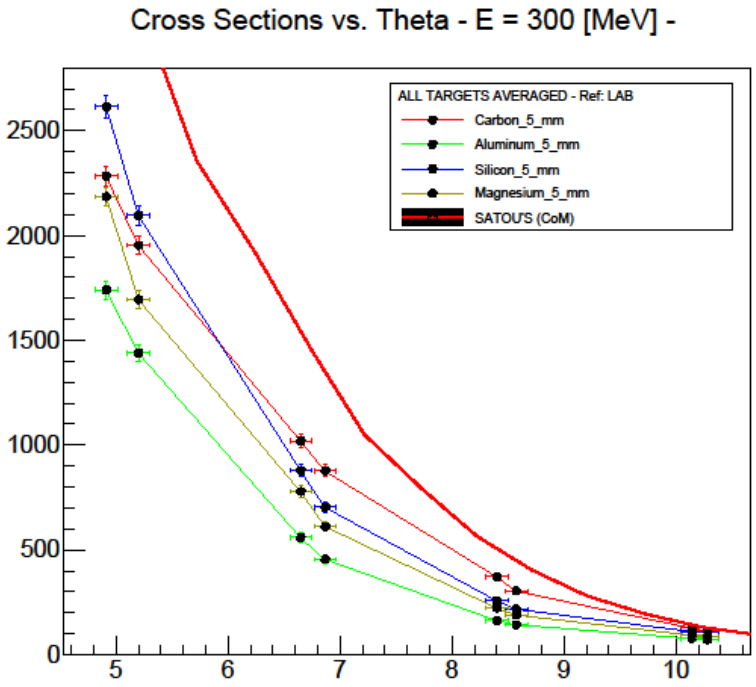

Figure 4.42 - Total unpolarized differential Cross section [mbarns/sr] @ 300 MeV for various elements. Both sides averaged. Reference frame: Laboratory.

Polarized Cross Sections: In the case of a polarized beam with a given degree a similar procedure can be used to calculate polarized cross sections, but since the detector measures a polarization-induced asymmetry in the beam-target scattering direction, the results measured in the two arms of the detector at a given theta value are not comparable and thus cannot be averaged like in the unpolarized case. The results of the two arms must then be visualized separately, allowing for a direct visualization of the asymmetry induced by the polarization in the beam. It is still possible to average upper and lower planes results in both arms to compare them to in-beamplane results, by use of the procedure described for unpolarized data. The polarized cross section is also linked to the unpolarized cross section of the same process by the formula (2.11) recalled here:

$$\sigma_{POL}(\vartheta) = \sigma_{UNPOL}(\vartheta) \cdot \left[1 + P_y A_y(\vartheta) \cos(\phi)\right]$$

Where ϑ is the polar angle, ϕ is the azimuthal angle, P_y is the beam polarization and A_y is the target vector analyzing power.
Once both the polarized and unpolarized cross sections are measured, they can be used, to evaluate the product $P_y A_y$, with the knowledge of P_y, the analyzing power A_y can be evaluated.
Results for polarized cross sections will now be presented and discussed for Carbon and other target elements.

CARBON POLARIZED CROSS SECTION @ 200 MeV –Polarization State: UP

Figure (4.43) shows single spectra for each crystal in left and right arm @ 200 MeV, beam polarization state: UP

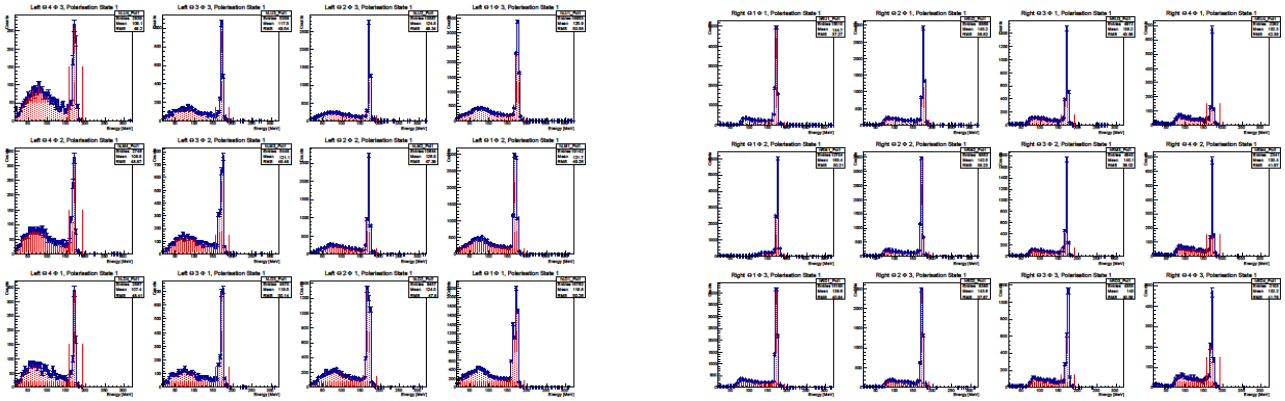

Figure 4.43 - dC Elastic scattering single spectra @ 200 MeV for left arm (LEFT) and right arm (RIGHT), Polarization state: UP. It is possible to see how beam polarization prompted an asymmetry in the scattering direction: counts on the right arm are in much higher number than on the left arm.

From the spectra in figure (4.43) it is already clear that the polarization state produced an asymmetry in the scattering direction and that the detector measures it correctly, in fact the number of counts on the right arm is much higher than the number of counts on the left arm.

Figures (4.44) and (4.45) show Cross Section values for each module in both arms, (in comparison with Satou's dC Cross Section). Polarization state: UP

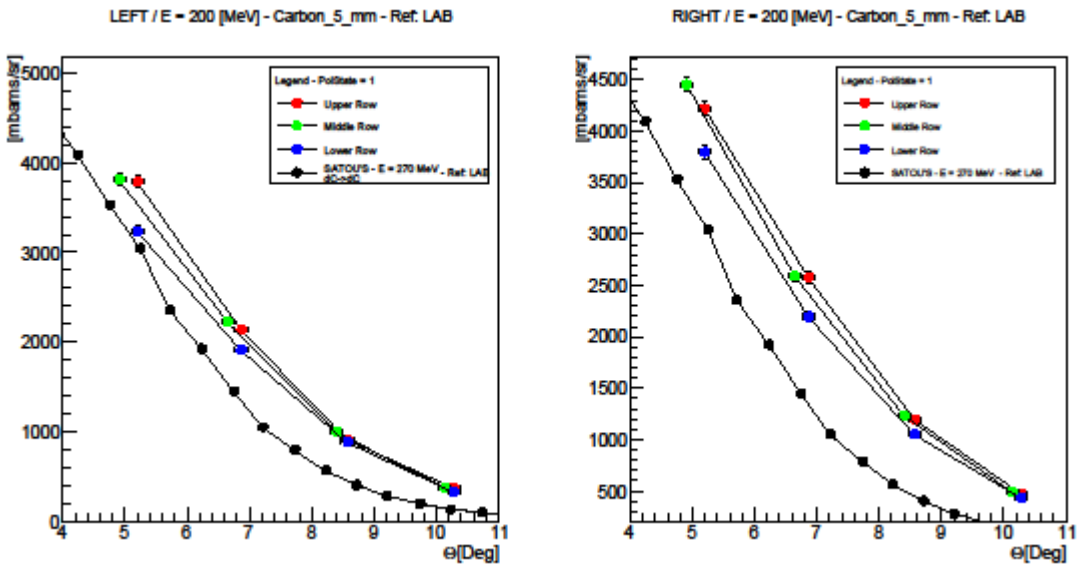

Figure 4.44 - dC elastic scattering polarized differential Cross section @ 200 MeV for each crystal separately. Polarization state: UP. GREEN = in-beamplane row, RED = Upper row, BLUE = Lower row. Reference frame: Laboratory.

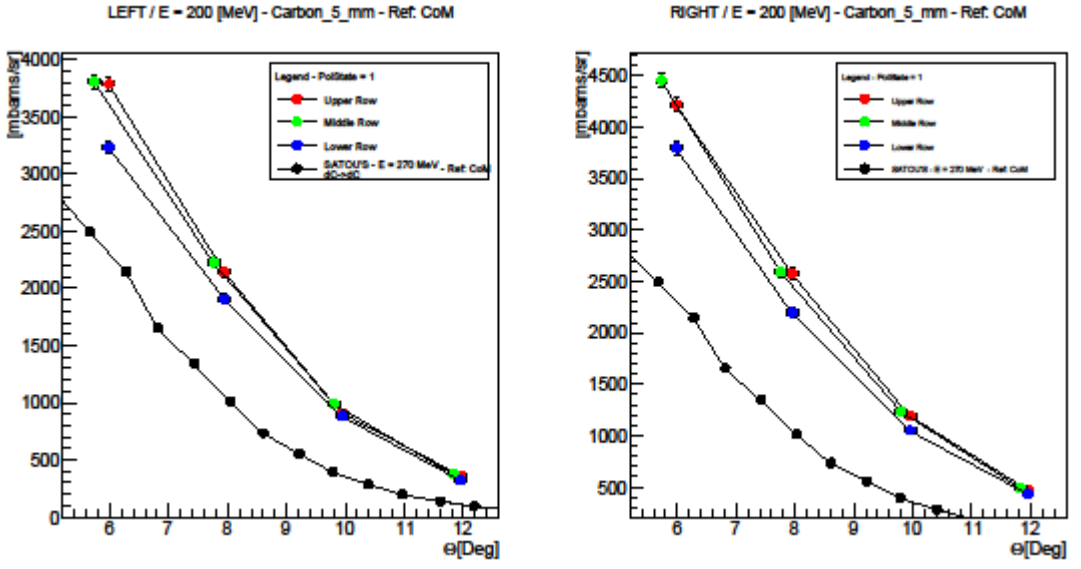

Figure 4.45 - dC elastic scattering polarized differential cross section @ 200 MeV. Polarization state: UP. Reference frame: Center of mass.

Figures (4.46) and (4.47) show the total Cross Section, left and right arms visualized separately. Polarization state: DOWN

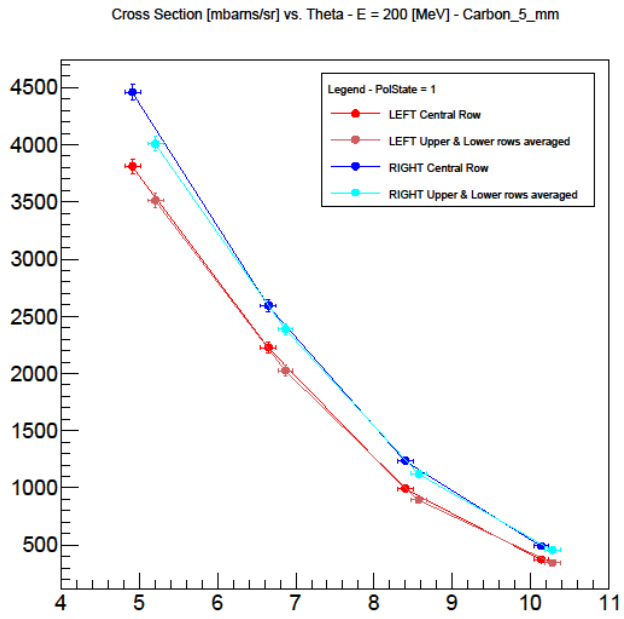

Figure 4.46 - Total dC polarized differential Cross section @ 200 MeV. Both sides visualized separately. Polarization state: UP. DARK RED = LEFT Upper and Lower rows averaged. RED = LEFT in-beamplane row. DARK BLUE = RIGHT Upper and Lower rows averaged. BLUE = RIGHT in-beamplane row. Reference frame: Laboratory.

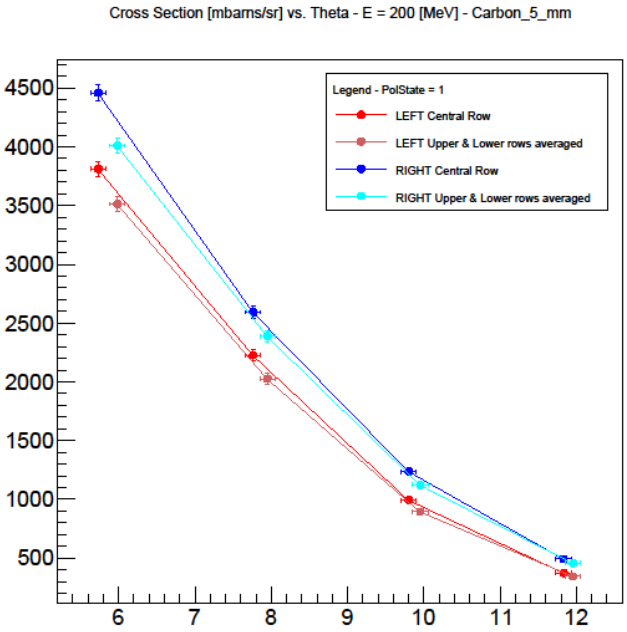

Figure 4.47 - Total dC polarized differential Cross section @ 200 MeV. Polarization state: UP. Both sides visualized separately. Reference frame: Center of Mass.

CARBON POLARIZED CROSS SECTION @ 200 MeV –Polarization State: DOWN

Figure (4.48) shows single spectra for each crystal in left and right arm @ 200 MeV, beam polarization state: DOWN

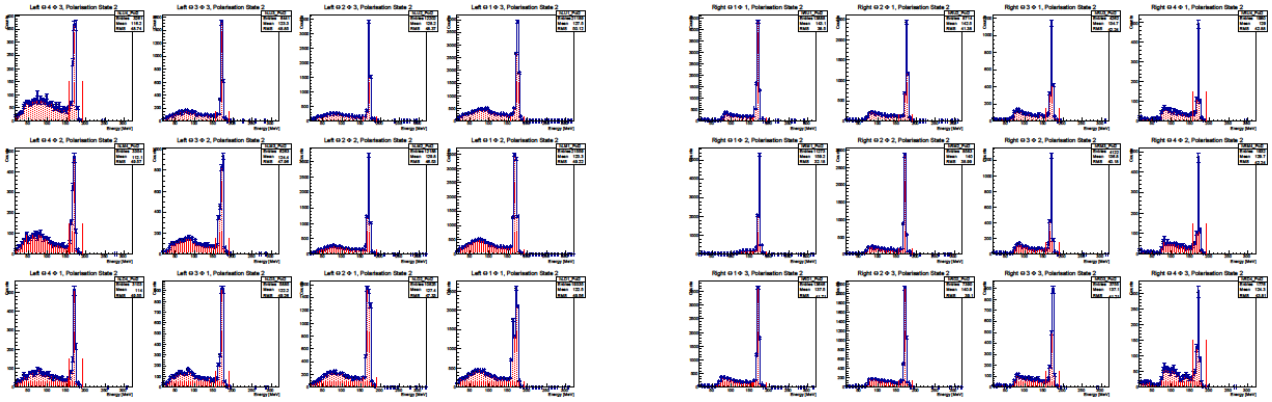

Figure 4.48 - dC Elastic scattering single spectra @ 200 MeV for left arm (LEFT) and right arm (RIGHT), Polarization state: DOWN. Counts on the left arm are higher than on the right arm.

Figures (4.49) and (4.50) show Cross Section values for each module in both arms, (in comparison with Satou's dC Cross Section). Polarization state: DOWN

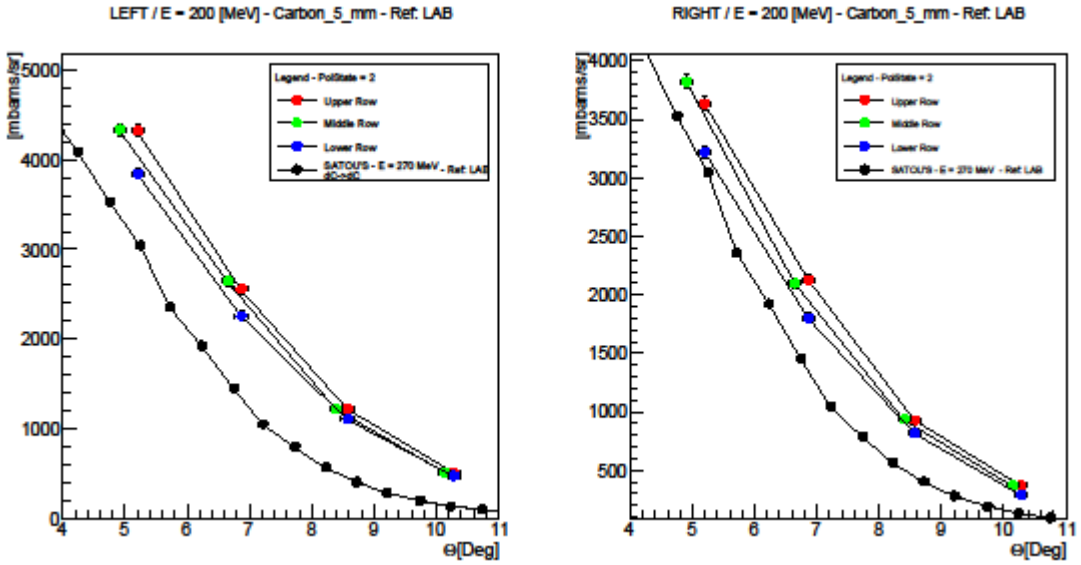

Figure 4.49 - dC elastic scattering polarized differential Cross section @ 200 MeV for each crystal separately. Polarization state: DOWN. GREEN = in-beamplane row, RED = Upper row, BLUE = Lower row. Reference frame: Laboratory.

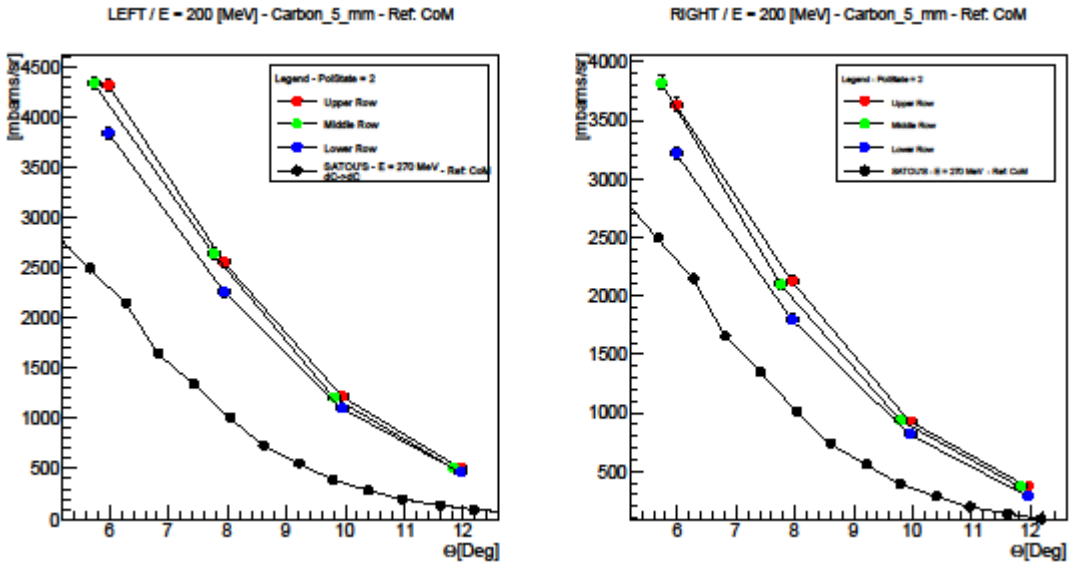

Figure 4.50 - dC elastic scattering polarized differential cross section @ 200 MeV. Polarization state: DOWN. Reference frame: Center of mass.

Figures (4.51) and (4.52) show the total Cross Section, left and right arms visualized separately. Polarization state: DOWN

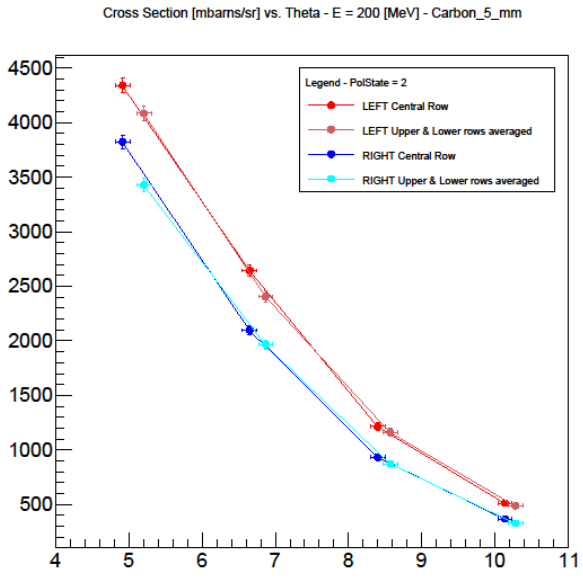

Figure 4.51 - Total dC polarized differential Cross section @ 200 MeV. Both sides visualized separately. Polarization state: UP. DARK RED = LEFT Upper and Lower rows averaged. RED = LEFT in-beamplane row. DARK BLUE = RIGHT Upper and Lower rows averaged. BLUE = RIGH T Upper and Lower rows averaged. BLUE = RIGHT in-beamplane row. Reference frame: Laboratory.

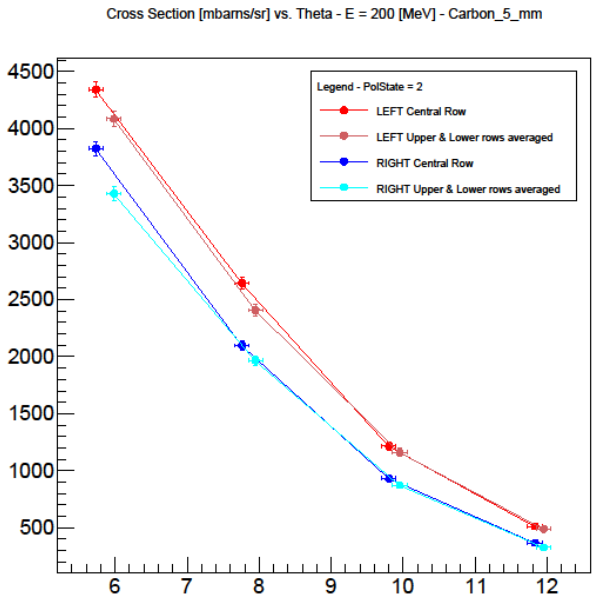

Figure 4.52 - Total dC polarized differential Cross section @ 200 MeV. Polarization state: UP. Both sides visualized separately. Reference frame: Center of Mass.

CARBON POLARIZED CROSS SECTION @ 270 MeV –Polarization State: UP

Figure (4.53) shows single spectra for each crystal in left and right arm @ 270 MeV, beam polarization state: UP

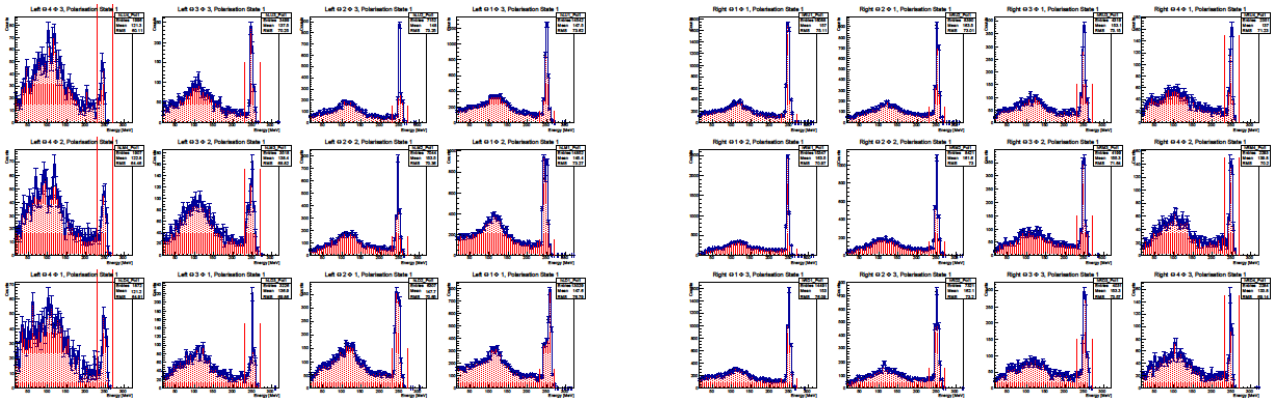

Figure 4.53 - dC Elastic scattering single spectra @ 270 MeV for left arm (LEFT) and right arm (RIGHT), Polarization state: UP. Counts on the right arm are higher than on the left arm.

Figures (4.54) and (4.55) show Cross Section values for each module in both arms, (in comparison with Satou's dC Cross Section). Polarization state: UP

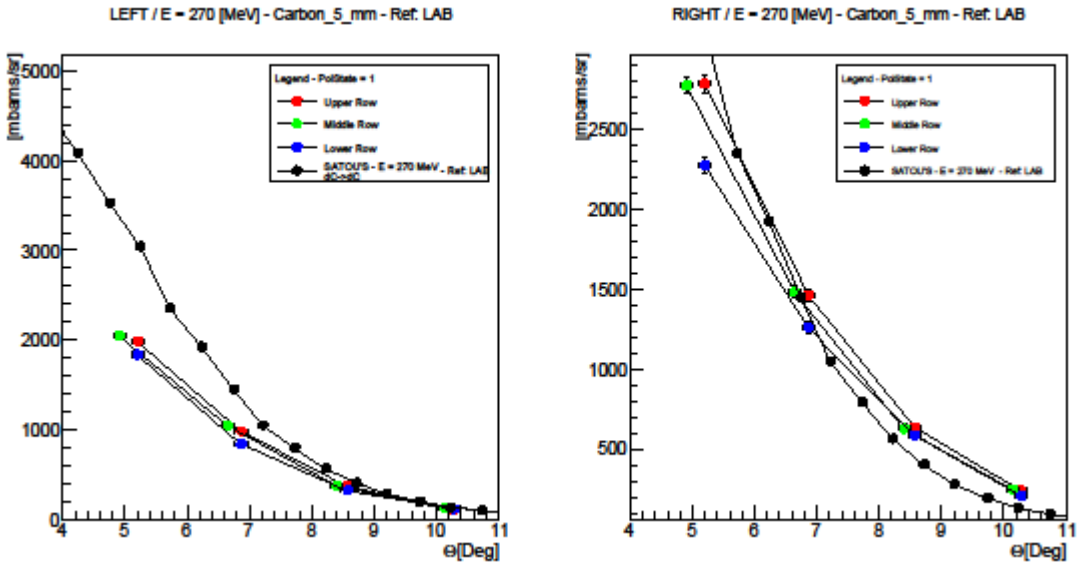

Figure 4.54 - dC elastic scattering polarized differential Cross section @ 270 MeV for each crystal separately. Polarization state: UP. GREEN = in-beamplane row, RED = Upper row, BLUE = Lower row. Reference frame: Laboratory.

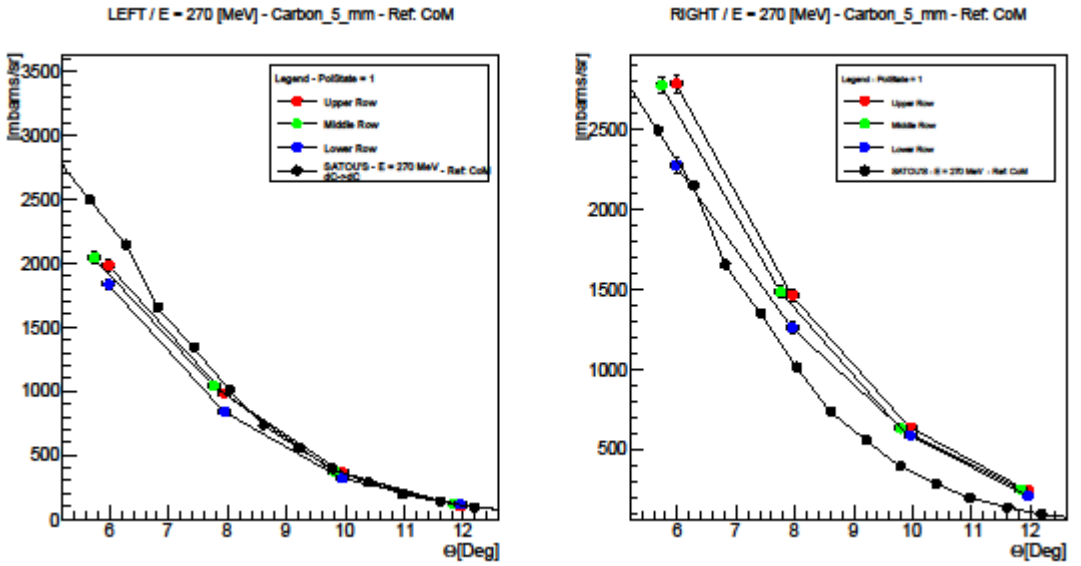

Figure 4.55 - dC elastic scattering polarized differential cross section @ 270 MeV. Polarization state: UP. Reference frame: Center of mass.

Figures (4.56) and (4.57) show the total Cross Section, left and right arms visualized separately. Polarization state: UP

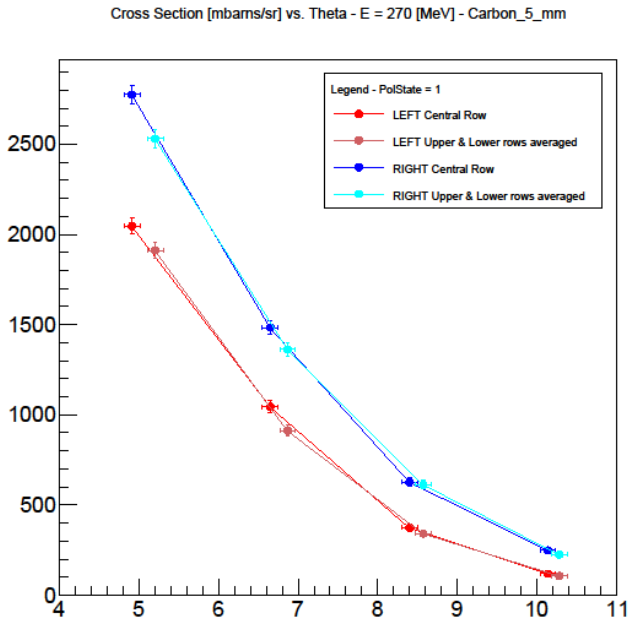

Figure 4.56 - Total dC polarized differential Cross section @ 270 MeV. Both sides visualized separately. Polarization state: UP. DARK RED = LEFT Upper and Lower rows averaged. RED = LEFT in-beamplane row. DARK BLUE = RIGHT Upper and Lower rows averaged. BLUE = RIGHT in-beamplane row. Reference frame: Laboratory.

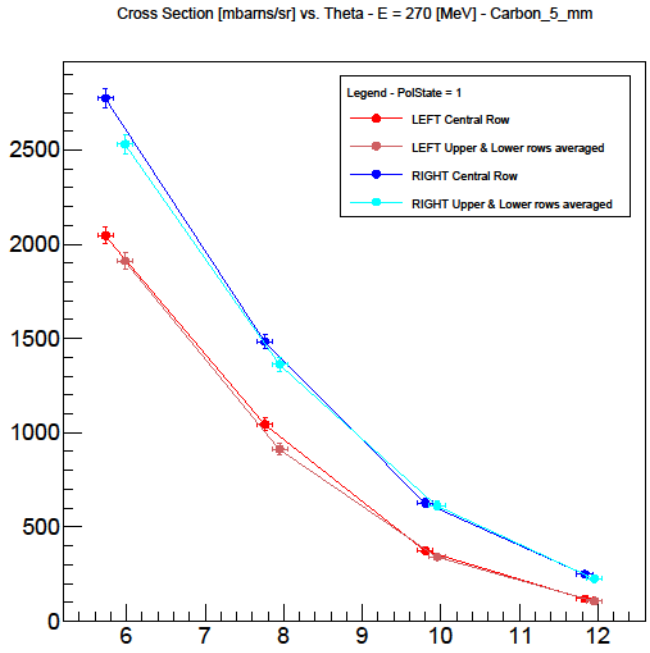

Figure 4.57 - Total dC polarized differential Cross section @ 270 MeV. Polarization state: UP. Both sides visualized separately. Reference frame: Center of Mass.

CARBON POLARIZED CROSS SECTION @ 270 MeV –Polarization State: DOWN

Figure (4.58) shows single spectra for each crystal in left and right arm @ 270 MeV, beam polarization state: DOWN

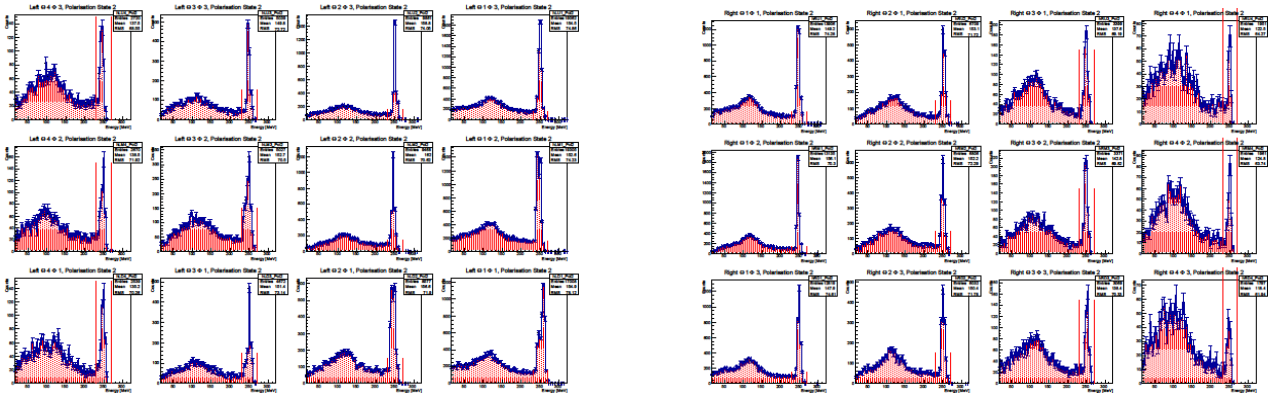

Figure 4.58 - dC Elastic scattering single spectra @ 270 MeV for left arm (LEFT) and right arm (RIGHT), Polarization state: DOWN. Counts on the left arm are higher than on the right arm.

Figures (4.59) and (4.60) show Cross Section values for each module in both arms, (in comparison with Satou's dC Cross Section). Polarization state: DOWN

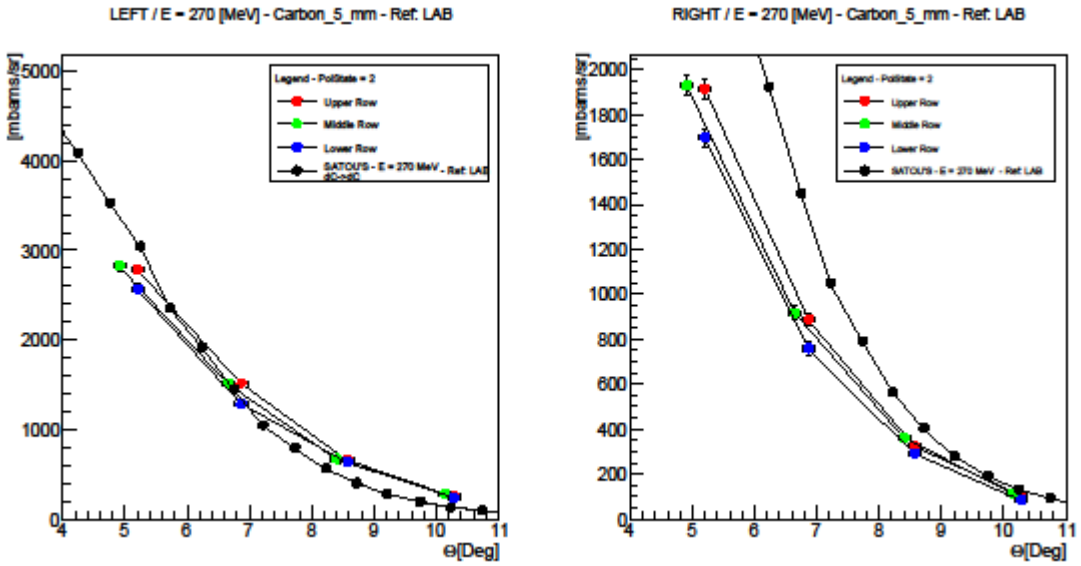

Figure 4.59 - dC elastic scattering polarized differential Cross section @ 270 MeV for each crystal separately. Polarization state: DOWN. GREEN = in-beamplane row, RED = Upper row, BLUE = Lower row. Reference frame: Laboratory.

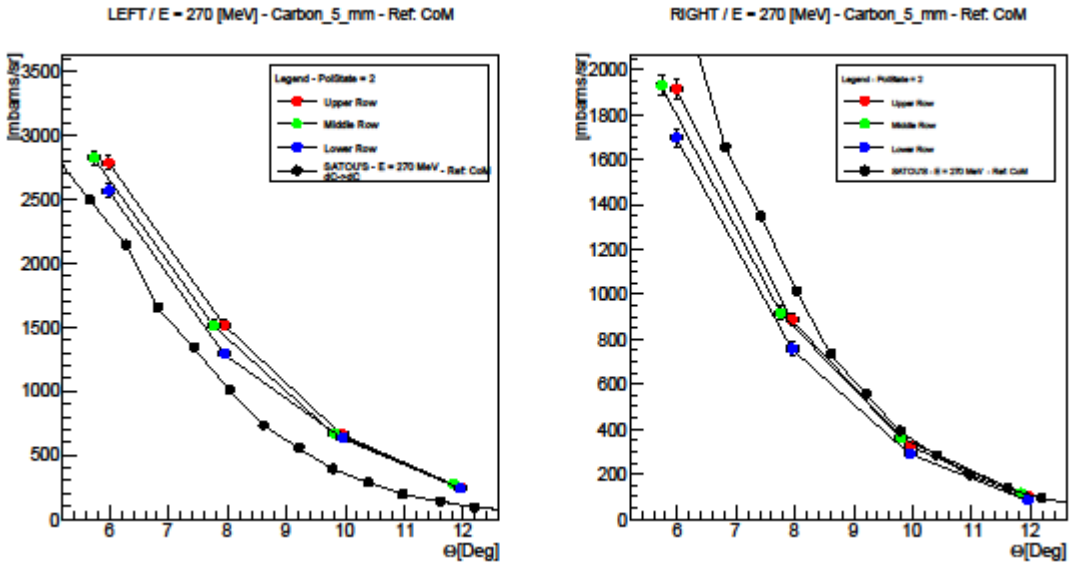

Figure 4.60 - dC elastic scattering polarized differential cross section @ 270 MeV. Polarization state: DOWN. Reference frame: Center of mass.

Figures (4.61) and (4.62) show the total Cross Section, left and right arms visualized separately. Polarization state: DOWN

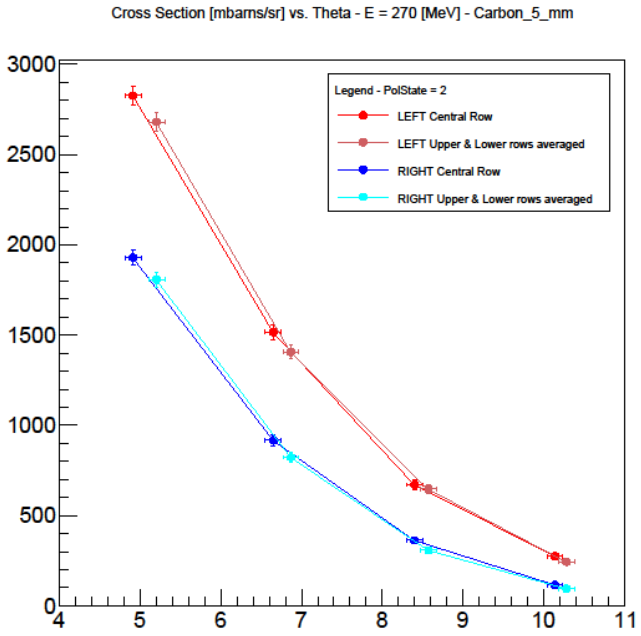

Figure 4.61 - Total dC polarized differential Cross section @ 270 MeV. Both sides visualized separately. Polarization state: DOWN. DARK RED = LEFT Upper and Lower rows averaged. RED = LEFT in-beamplane row. DARK BLUE = RIGHT Upper and Lower rows averaged. BLUE = RIGHT in-beamplane row. Reference frame: Laboratory.

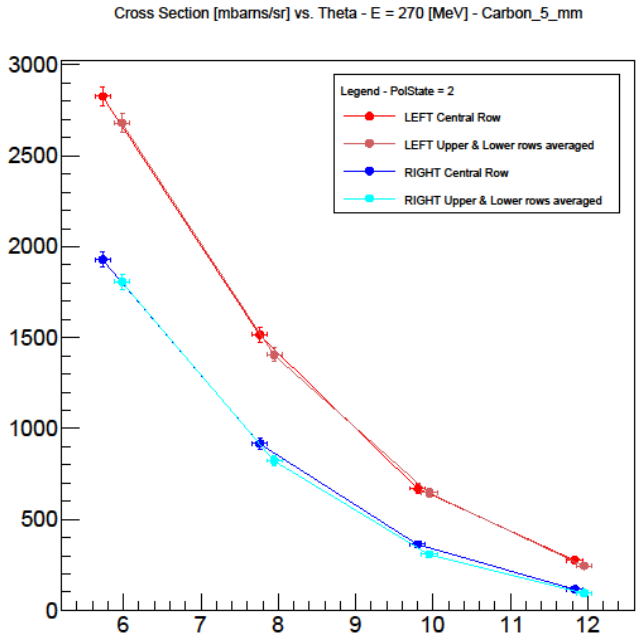

Figure 4.62 - Total dC polarized differential Cross section @ 270 MeV. Polarization state: UP. Both sides visualized separately. Reference frame: Center of Mass.

CARBON POLARIZED CROSS SECTION @ 300 MeV –Polarization State: UP

Figure (4.63) shows single spectra for each crystal in left and right arm @ 300 MeV, beam polarization state: UP

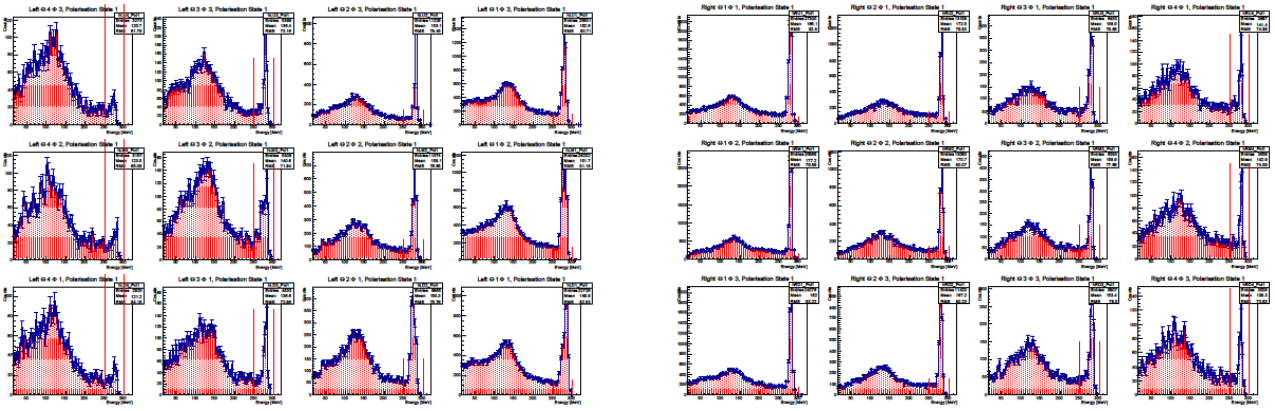

Figure 4.63 - dC Elastic scattering single spectra @ 300 MeV for left arm (LEFT) and right arm (RIGHT), Polarization state: UP. Counts on the right arm are higher than on the left arm.

Figures (4.64) and (4.65) show Cross Section values for each module in both arms, (in comparison with Satou's dC Cross Section). Polarization state: UP

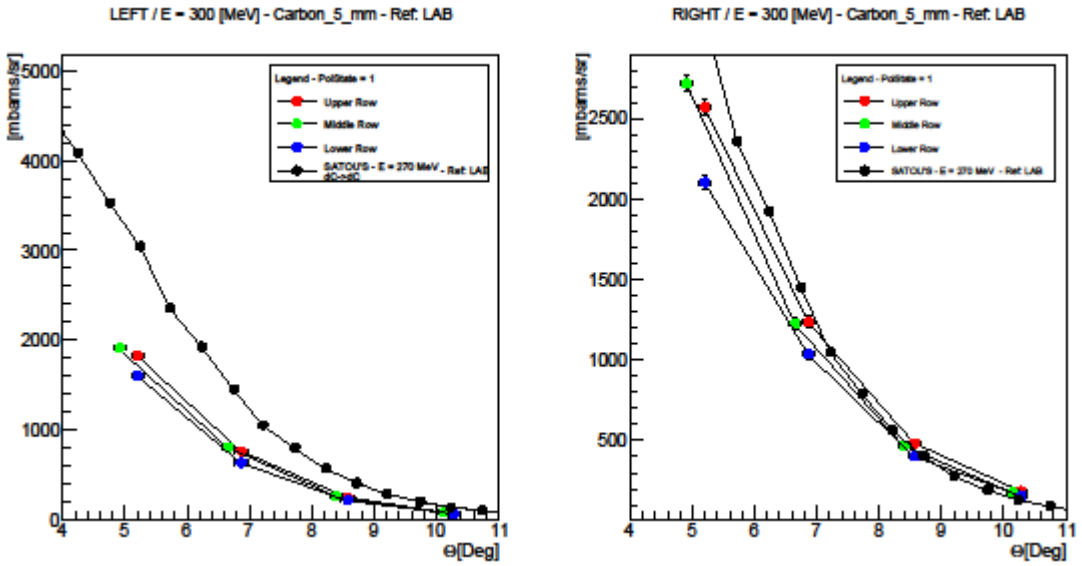

Figure 4.64 - dC elastic scattering polarized differential Cross section @ 300 MeV for each crystal separately. Polarization state: UP. GREEN = in-beamplane row, RED = Upper row, BLUE = Lower row. Reference frame: Laboratory.

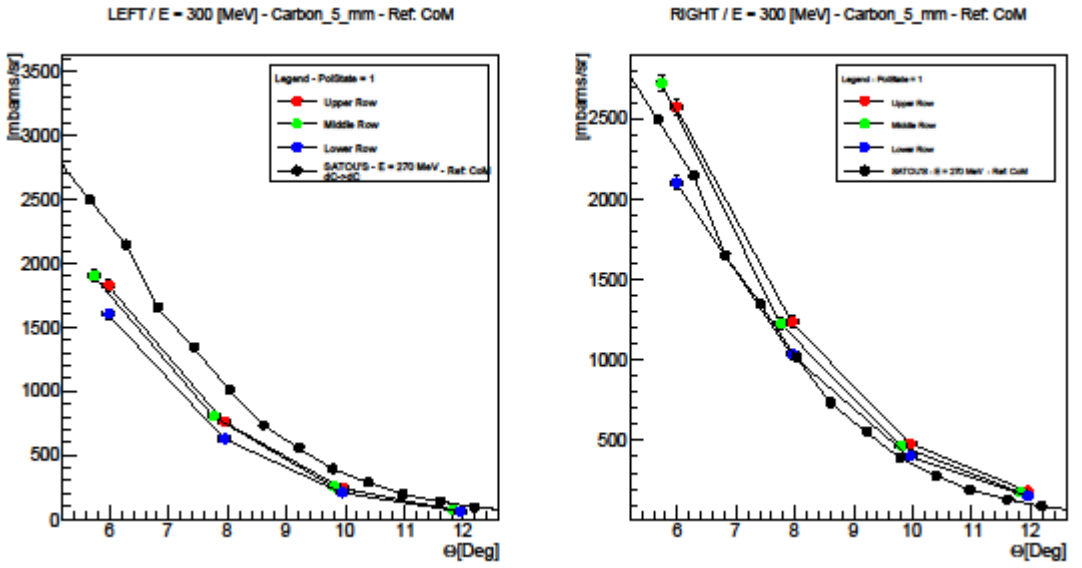

Figure 4.65 - dC elastic scattering polarized differential cross section @ 300 MeV. Polarization state: UP. Reference frame: Center of mass.

Figures (4.66) and (4.67) show the total Cross Section, left and right arms visualized separately. Polarization state: UP

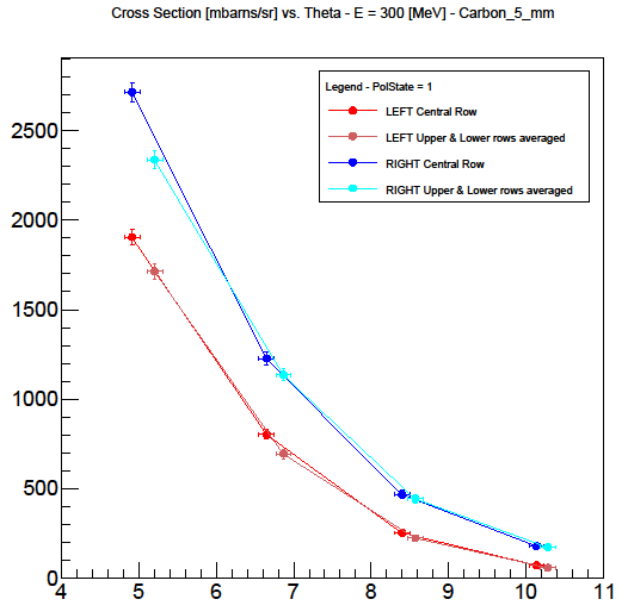

Figure 4.66 - Total dC polarized differential Cross section @ 300 MeV. Both sides visualized separately. Polarization state: UP. DARK RED = LEFT Upper and Lower rows averaged. RED = LEFT in-beamplane row. DARK BLUE = RIGHT Upper and Lower rows averaged. BLUE = RIGH T Upper and Lower rows averaged. BLUE = RIGHT in-beamplane row. Reference frame: Laboratory.

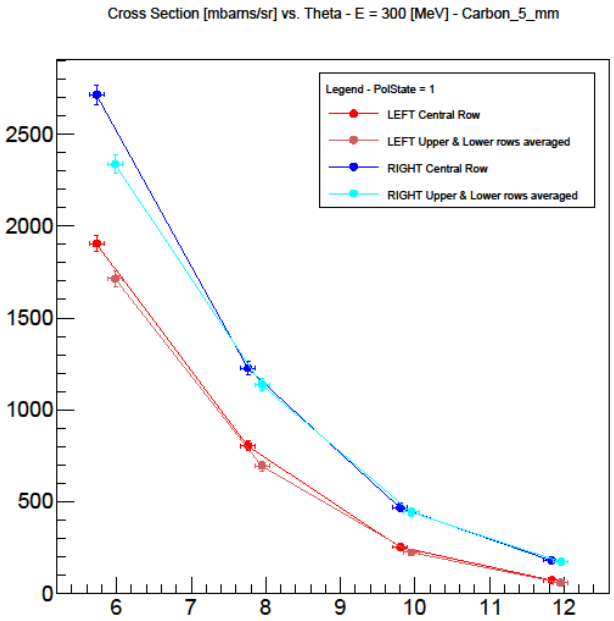

Figure 4.67 - Total dC polarized differential Cross section @ 300 MeV. Polarization state: UP. Both sides visualized separately. Reference frame: Center of Mass.

CARBON POLARIZED CROSS SECTION @ 270 MeV –Polarization State: DOWN

Figure (4.68) shows single spectra for each crystal in left and right arm @ 300 MeV, beam polarization state: DOWN

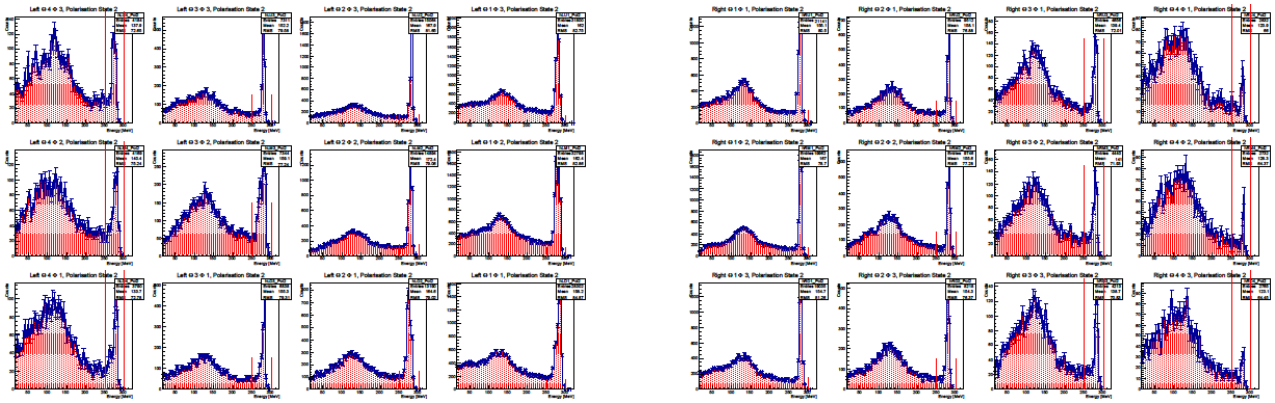

Figure 4.68 - dC Elastic scattering single spectra @ 300 MeV for left arm (LEFT) and right arm (RIGHT), Polarization state: DOWN. Counts on the left arm are higher than on the right arm.

Figures (4.69) and (4.70) show Cross Section values for each module in both arms, (in comparison with Satou's dC Cross Section). Polarization state: DOWN

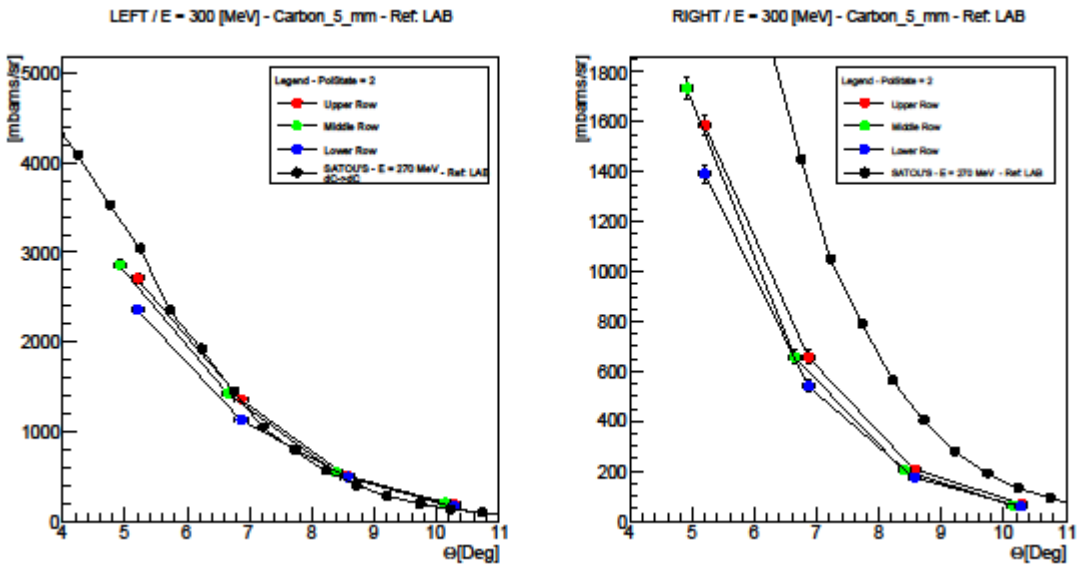

Figure 4.69 - dC elastic scattering polarized differential Cross section @ 300 MeV for each crystal separately. Polarization state: DOWN. GREEN = in-beamplane row, RED = Upper row, BLUE = Lower row. Reference frame: Laboratory.

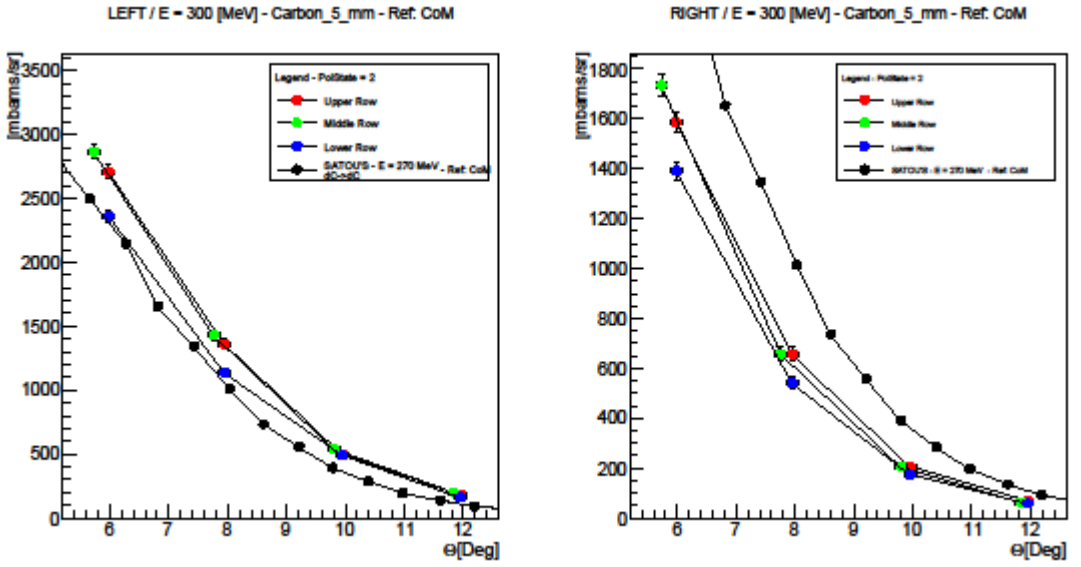

Figure 4.70 - dC elastic scattering polarized differential cross section @ 300 MeV. Polarization state: DOWN. Reference frame: Center of mass.

Figures (4.71) and (4.72) show the total Cross Section, left and right arms visualized separately. Polarization state: DOWN

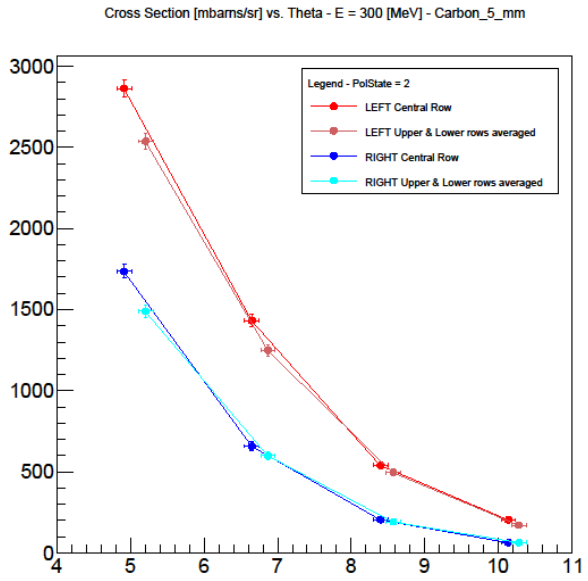

Figure 4.71 - Total dC polarized differential Cross section @ 300 MeV. Both sides visualized separately. Polarization state: DOWN. DARK RED = LEFT Upper and Lower rows averaged. RED = LEFT in-beamplane row. DARK BLUE = RIGHT Upper and Lower rows averaged. BLUE = RIGH T in-beamplane row. Reference frame: Laboratory.

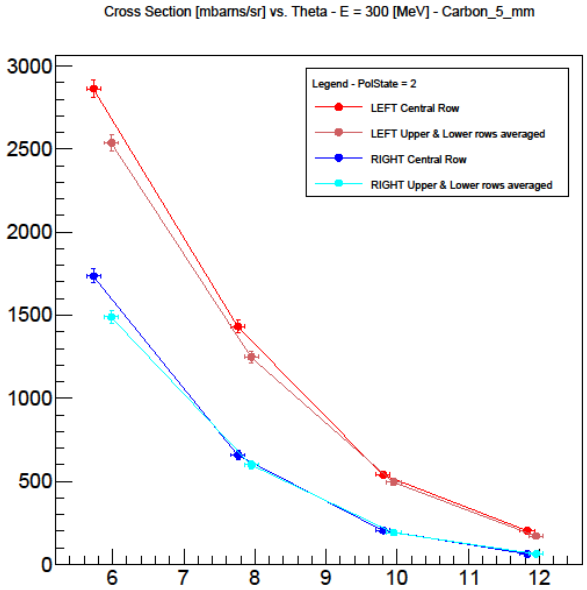

Figure 4.72 - Total dC polarized differential Cross section @ 300 MeV. Polarization state: UP. Both sides visualized separately. Reference frame: Center of Mass.

CONCLUSIONS

The result plots shown here, along with results of other different target materials, prove that the LYSO-based SiPM-read polarimeter works quite well in measuring scattering asymmetry and thus a net beam polarization if present. However there are several issues, mainly regarding LYSO modules energy resolution, to be addressed yet. Figure (4.73) shows a comparison between LYSO energy resolutions as a function of incoming deuteron beam energy. The blue line is the first measurement obtained with PMT readout, and the red line is an average of all modules with SiPM readout from November 2017 beam time.

The figure shows a clear sub-percent resolution for SiPM-based LYSO modules but with quite big error bars. These errors come partially from a significant deviation between modules caused by light sensor sensitivity, optical coupling, and readout channels. Also, during scattering experiments, a double peak was observed in some of the crystals, with each peak being very narrow with about a third of the present resolution.

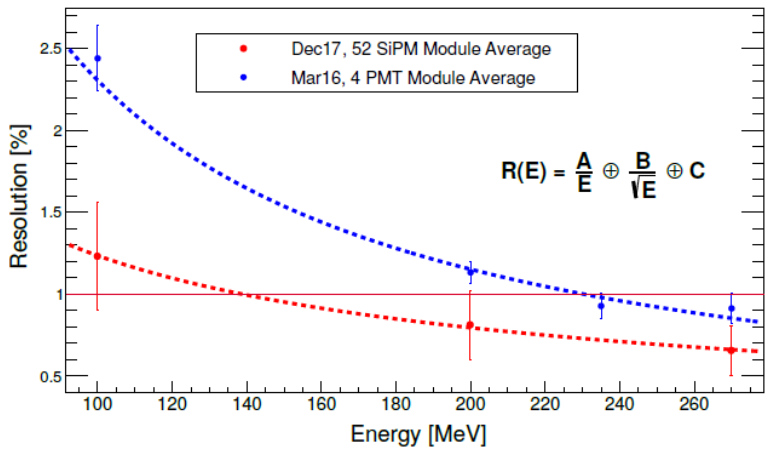

Figure 4.73 - The comparison of energy resolutions as a function of incoming deuteron beam energy. Blue data points are the first measurement of the LYSO crystals with PMT readout. The red data points are averages of all modules with SiPM readout from December 2017 beam time. Note: here the resolution is defined as a FWHM divided by amplitude.

The integrals of the peaks were very dependent on beam spot location when aiming at crystals.
These observations lead to the decision of carrying out more careful and detailed crystal scans that were performed in the March 2018 beam time and are descripted in the next section.

4.5 Step 3: LYSO crystals homogeneity scans

A further step in the development of the LYSO-based polarimeter took place in the BIG KARL experimental area at FZJ in March 2018. It was primarily aimed to perform a series of scans on LYSO crystals in order to obtain a map that shows the behavior of each module in terms of light emission homogeneity, so to be able to apply a tailored correction to the spectra acquired by each crystal. A 300 MeV focused deuteron beam was then injected directly into front and side face of each LYSO crystal.
In this beam time also a comparison between different types of SiPM arrays from different manufacturers was carried out.

4.5.1 Setup description

For this experimental test 28 new LYSO modules for a total of 52 modules have been built and arranged in the same cross-shaped pattern as they will be in the ultimate detector device. All modules were mounted on a stainless steel circular plate that can rotate about beam direction axis thanks to an online controlled stepper motor. The circular plate with the 52 LYSO modules was then mounted on a mainframe that allows for position adjustment via remotely controlled electric motors. Figure (4.74) shows a sketch of the experimental setup.

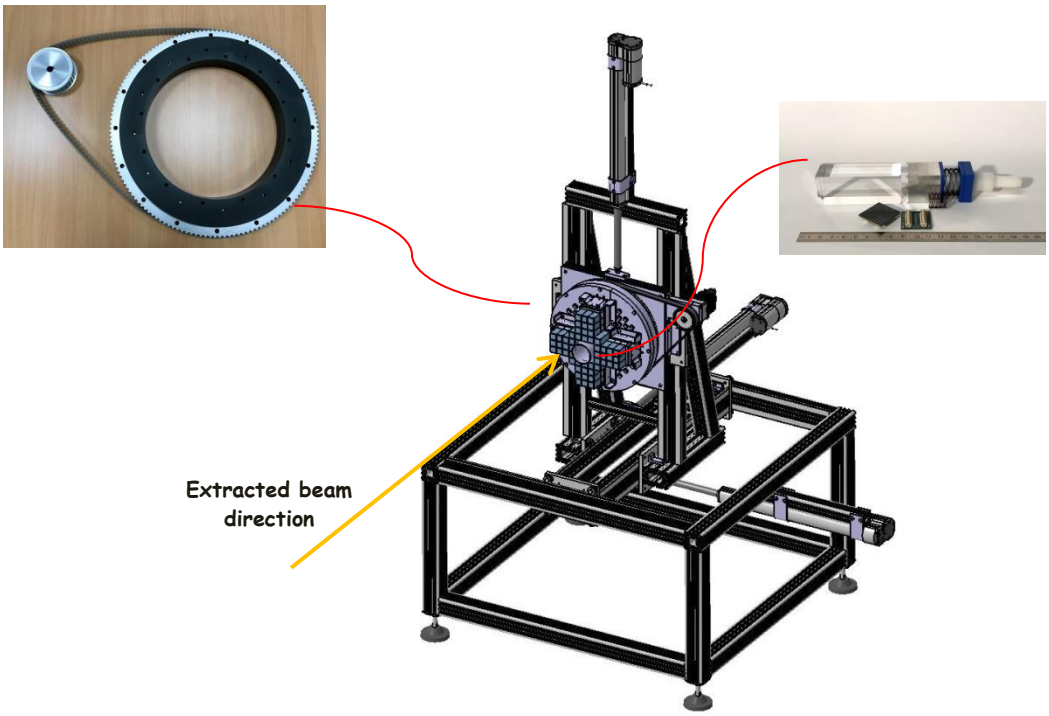

Figure 4.74 - Sketch of the experimental setup built and used in the March 2018 beam time. The upper left particular shows the mechanical system used to rotate the detector sensitive volume about beam direction axis. Upper right picture shows one of the LYSO modules disassembled. Yellow line shows the direction of the extracted deuteron beam.

Figures (4.75) shows the naked mainframe and a particular of assembling operations respectively. In figure (4.76) a front picture of the assembled setup is shown.

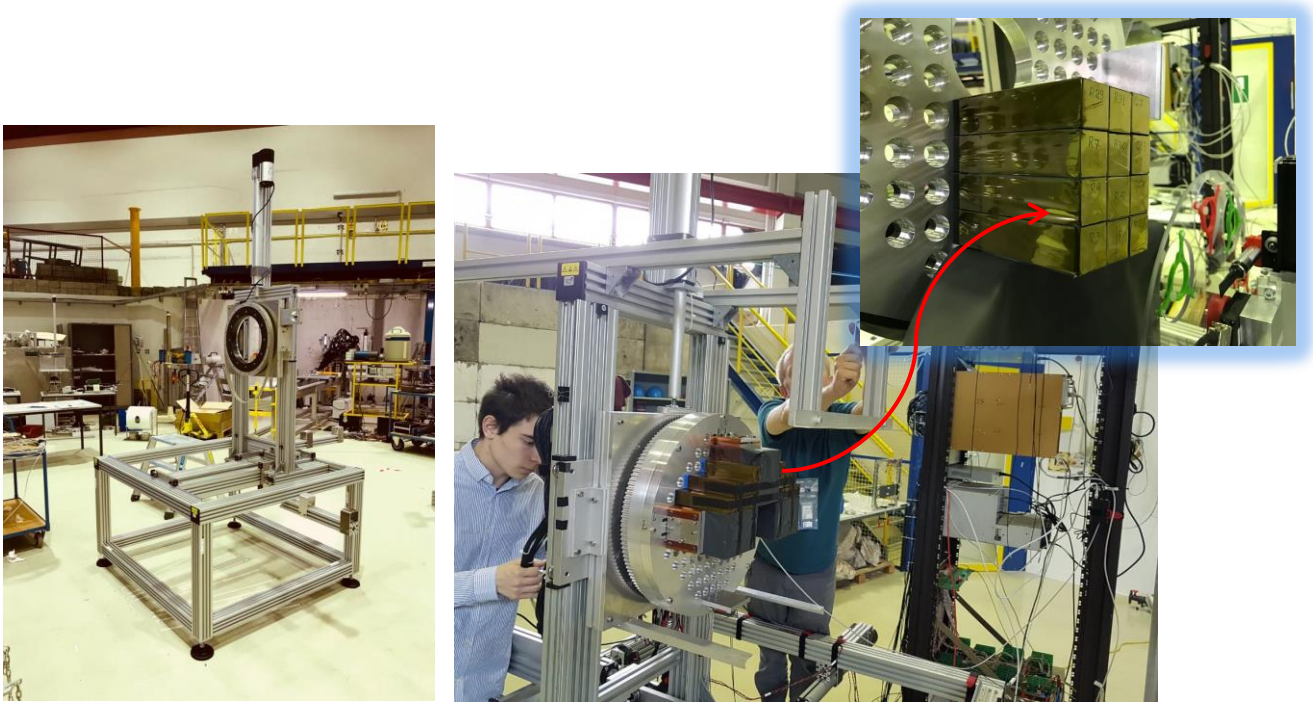

Figure 4.75 - LEFT: naked mainframe of the experimental setup. RIGHT: particular of assembling operations. UPPER RIGHT: particular of one of the four detector "wings".

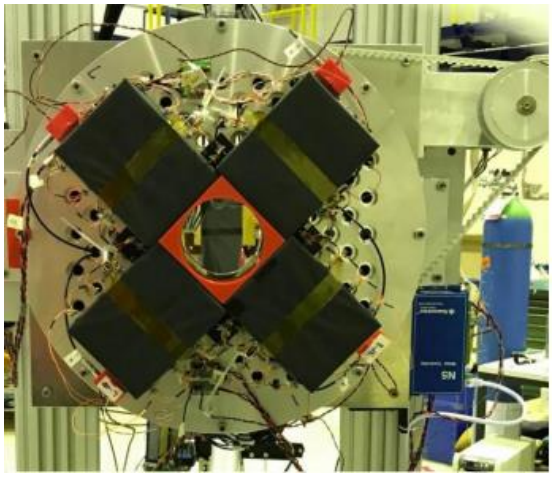

Figure 4.76 - Particular of the final experimental setup: 48 LYSO modules arranged in a cross-shaped pattern around the beam direction. 4 modules not yet mounted in picture.

The setup was assembled in the BIG KARL experimental area at COSY facility at FZJ and a 300 MeV extracted deuteron beam was shot into the front and side face of each crystal.

4.5.2 Results of LYSO crystals front and side scans

The scans performed on each crystal resulted in a map showing the homogeneity of the energy reconstruction. Figure (4.77) shows the

results for one crystal front face, Figure (4.78) shows the results for the same crystal side face.

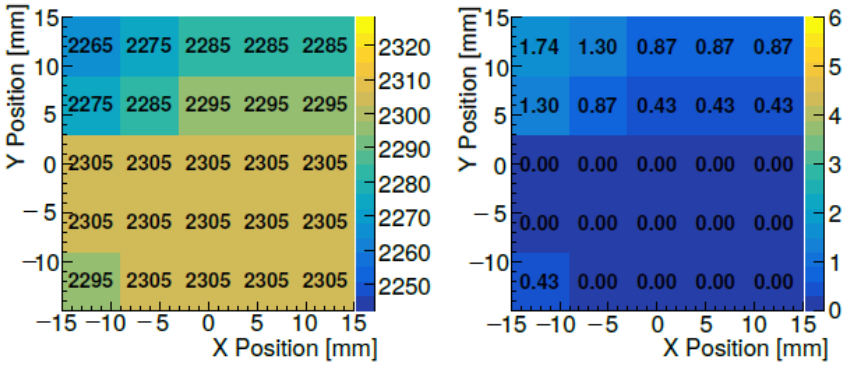

Figure 4.77 - A typical 5x5 front face map of a LYSO crystal with a 300MeV deuteron beam. Left: the absolute values of peak position of the beam energy. Right: the relative deviation from the maximum value showing the homogeneity of the energy reconstruction to be within two percent.

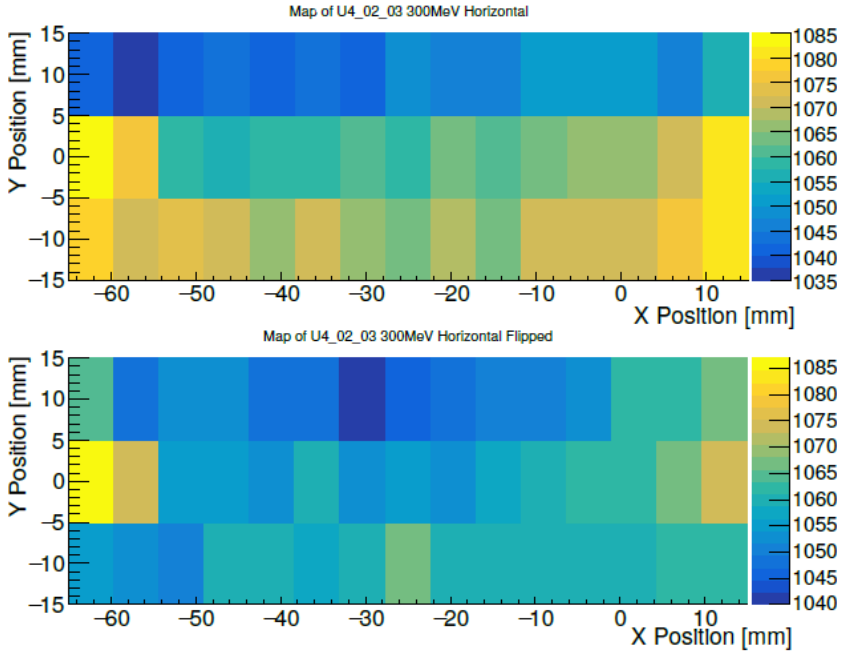

Figure 4.78 - A 15x3 side face map of a LYSO crystal at 300MeV deuteron beam. In both measurements, the sensor is located on the right side. Upper: The same orientation as for the Fig. 4.77. Clear lowering of the light output can be identified in the upper part of the crystal. Lower: The 90° rotated map of the same crystal showing a different light output distribution from the upper face. Note: the crystals are only 3 cm thick, so deuterons are punching through.

As can be seen from the figures above, significant deviations in the light output homogeneity were found and identified for the crystal shown in figure as well as for all other crystals at one energy value (300 MeV). Some of the crystals were scanned also with different energies but no energy dependence was found.
Front and side face maps of all 52 LYSO modules at one energy are now obtained, and will be used in next experimental sessions to apply a correction to acquired data for all those errors coming from crystal inhomogeneity.

4.5.3 Comparison between different types of SiPMs

The second task accomplished in this beam time was the comparison of SiPMs with different pixel size and from different manufacturer. Namely three types of SiPM arrays have been compared: SensL 20μm, Ketek 25 μm and Ketek 15 μm pixel size array. Figure (4.79) shows the results of this comparison.

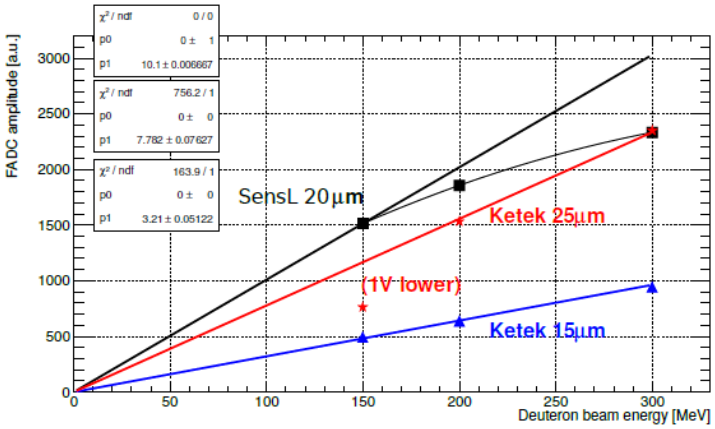

Figure 4.79 - Typical measured amplitudes for SensL 20 µm (black), Ketek 25 µm (red) and Ketek 15 µm (blue) pixel size array vs. deuteron beam energy. All points are pedestal subtracted. That's why all linear fits are zero normalized (y = g·x). Black line: only 150MeV measurement is fitted and extrapolated to 300MeV . Red line: only the measurements at 200 and 300MeV are in fit. Blue line: only the measurements at 150 and 200MeV are fitted and extrapolated.

As expected, the smallest pixel ($15\,\mu m$) leads to a higher number of pixels per unit area and thus to a higher dynamic range.
Even though the pixel size is slightly bigger for the Ketek $25\,\mu m$ than for the SensL $20\,\mu m$, the amplitude vs. energy behavior of the Ketek is more linear in the operating range, this can be explained by the pixel architecture and PCB layout of the Ketek array, designed to drastically reduce optical crosstalk and dark current.
In general, all three types of SiPM arrays can be used successfully, but when building new LYSO modules in the future the choice will most probably be $15\,\mu m$ Ketek arrays because of their better dynamic range. Also, Ketek arrays have separated SiPM connectors, this will allow for more flexibility in design and test different readout PCB schemes for a signal including data reduction.

CONCLUSIONS

Argument of the present work is the development of a precision beam polarimeter to support the EDM feasibility studies performed at COSY storage ring of the FZ-Jülich in Germany in the period between February 2016 and January 2019, the polarimeter consists of single modules of LYSO crystal with an integrated SiPM readout system. The development started from the conceptual design and ended with the construction of a prototype with the use of which a series of tests on an extracted beam station have been performed. The tests concerned elastic deuteron scattering of six different target materials (C, Mg, Al, Si, Ni, Sn). Also, several different beam energies (100, 150, 200, 270, 300 MeV) with very different intensities (from several Hz to several MHz) have been used. The detector hardware is very reliable and the online analysis software is robust and operational. After its successful commissioning and exploitation on the test bench, the collaboration plans to install and test the full detector on COSY ring in spring 2019.

BIBLIOGRAPHY

[1] M. S. Sozzi, Discrete symmetries and CP violation: from experiment to theory., vol. XVI, Oxford: Oxford graduate texts. englisch. Univ. Press, 2008.

[2] R. A. Alpher e. al., "The Origin of Chemical Elements" *Phys. Rev. 73,* p. 803 804, 7 1948.

[3] B. D. Fields e. al, "Big Bang Nucleosynthesis," *Chin. Phys. C38,* p. 339 344, 2014.

[4] P. A. R. Ade e. al, "Planck 2013 results. XVI. Cosmological parameters," *Astron. Astrophys. 571,* 2014.

[5] W. Bernreuther, "CP violation and baryogenesis" *Lect. Notes Phys. 591,* p. 237 293, 2002.

[6] M. Aguilar e. al., "Precision Measurement of the Helium Flux in Primary Cosmic Rays of Rigidities 1.9 GV to 3 TV with the Alpha Magnetic Spectrometer on the International Space Station," *Phys. Rev. Lett. 115,* p. 211101, 2015.

[7] M. Aguilar e. al., "Precision Measurement of the Proton Flux in Primary Cosmic Rays from Rigidity 1 GV to 1.8 TV with the Alpha Magnetic Spectrometer on the International Space Station," *Phys. Rev. Lett. 114,* p. 171103, 2015.

[8] J. H. Christenson e. al., "Evidence for the 2π Decay of the K_L^0" *Phys. Rev. Lett. 13,* p. 138 140, 1964.

[9] I. B. Khriplovich, "CP violation without strangeness: electric dipole moments of particles, atoms, and molecules", XII, 230 S., Berlin: Springer, 1997.

[10] J. H. Smith e. al., "Experimental Limit to the Electric Dipole Moment of the Neutron," *Phys. Rev. 108,* p. 120 122, 1957.

[11] C. A. Baker e. al., "Improved Experimental Limit on the Electric Dipole Moment of the Neutron," *Phys. Rev. Lett. 97,* p. 131801, 2006.

[12] J. Baron e. al., "Order of Magnitude Smaller Limit on the Electric Dipole Moment of the Electron," *343.6168,* p. 269 272, 2014.

[13] B. Graner e. al., "Reduced Limit on the Permanent Electric Dipole Moment of 199Hg," *Phys. Rev. Lett. 116,* p. 161601, 16 2016.

[14] V. F. Dimitriev and R. A. Sen'kov, "Schiff Moment of the Mercury Nucleus and the Proton Dipole Moment," *Phys. Rev. Lett. 91,* p. 212303, 21 2003.

[15] G. W. Bennet e. al., "Improved limit on the muon electric dipole moment," *Phys. Rev. D 80,* p. 052008, 5 2009.

[16] J. Pretz e. al., "Measurement of Permanent Electric Dipole Moments of Charged Hadrons in Storage Rings," 2013.

[17] M. Zurek, "Searches for Electric Dipole Moments (EDM) at aStorage Ring with JEDI," in *NuFact2018*, Blacksburg, Virginia,

2018.

[18] R. Maier, "Cooler synchrotron COSY - Performance and perspectives," *Nuclear Instruments and Methods in Physics Research Section A: Accelerators, Spectrometers, Detectors and Associated Equipment 390.1-2,* pp. 1 - 8, 1997.

[19] D. Prasuhn e. al., "Electron and stochastic cooling at COSY," *Nuclear Instruments and Methods in Physics Research Section A: Accelerators, Spectrometers, Detectors and Associated Equipment 441.1,* p. 167 174, 2000.

[20] W. Haeberli, "Sources of Polarized Ions," *Annual Review of Nuclear and Particle Science 17,* p. 373 426, 1967.

[21] D. Chiladze e. al., "Determination of deuteron beam polarizations at COSY," *Physical Review Special Topics – Accelerators and Beams 9,* p. 050101, 2006.

[22] Z. Bagdasarian e. al., "Measuring the polarization of a rapidly precessing deuteron beam," *Phys. Rev. ST Accel. Beams 17,* p. 052803, 5 2014.

[23] Gerald G. Ohlsen. and P. W. Keaton, "Techniques for measurement of spin-12 and spin-1 polarization analyzing tensors," *spin-1 polarization analyzing tensors,* p. 41 59, 1973.

[24] N. P. M. Brantjes e. al., "Correcting systematic errors in high-sensitivity deuteron," *Nucl. Instrum. Meth. A664,* p. 49 64, 2012.

[25] G. Guidoboni, Spin Coherence Time Studies fot the Storage Ring EDM Search, Ferrara: Tesi di Dottorato di Ricerca in Fisica, 2012, p. 30 34.

[26] G. Guidoboni e. al., "How to Reach a Thousand-Second in-Plane Polarization Lifetime with 0.97 GeV/c Deuterons in a Storage Ring," *Phys. Rev. Lett. 117,* p. 054801, 5 2016.

[27] G. Guidoboni e. al., "Spin coherence time studies of a horizontally polarized deuteron beam at COSY, pp. 2-5.

[28] D. Eversmann e. al., "New method for a continuous determination of the spin tune in storage rings and implications for precision experiments," *Phys. Rev. Lett. 115.9,* p. 094801, 2015.